NANOPARTICLE DEPOSITION FROM AIR AS AN INADVERTENT SOURCE OF FOOD CONTAMINATION AND EDIBLE PLANT SURFACE RESPONSES

Eva Kranjc

Doctoral Dissertation
Jožef Stefan International Postgraduate School
Ljubljana, Slovenia

Supervisor: Prof. Maja Remškar, Jožef Stefan Institute, Ljubljana, Slovenia

Evaluation Board:
Prof. Radmila Milačič, Chair, IPS and Jožef Stefan Institute, Ljubljana, Slovenia
Prof. Damjana Drobne, Member, Biotechnical Faculty, University of Ljubljana, Ljubljana, Slovenia
Prof. Branka Salopek Sondi, Member, Department for Molecular Biology, Ruđer Bošković Institute, Zagreb, Croatia

MEDNARODNA PODIPLOMSKA ŠOLA JOŽEFA STEFANA
JOŽEF STEFAN INTERNATIONAL POSTGRADUATE SCHOOL

Eva Kranjc

NANOPARTICLE DEPOSITION FROM AIR AS AN INADVERTENT SOURCE OF FOOD CONTAMINATION AND EDIBLE PLANT SURFACE RESPONSES

Doctoral Dissertation

NALAGANJE NANODELCEV IZ ZRAKA KOT NENAMERNO ONESNAŽENJE HRANE IN ODZIV POVRŠIN UŽITNIH RASTLIN

Doktorska disertacija

Supervisor: Prof. Maja Remškar

Ljubljana, Slovenia, February 2019

To my husband, Sebastijan Magdič

Acknowledgments

The multi-disciplinary nature of this doctoral work necessitated a large amount of collaboration and assistance from many people spread out over multiple departments and institutions. I would first like to thank and acknowledge my supervisor, Prof. Dr. Maja Remškar, for providing me with the opportunity and support to grow as a scientist. I would also like to thank the members of the evaluation commission for my doctoral dissertation for their valuable critiques, which in some cases extend beyond the preparation of this work: Prof. Dr. Radmila Milačič, Prof. Dr. Damjana Drobne, and Asst. Prof. Branka Salopek Sondi. Additional thanks and acknowledgment go to Prof. Dr. Milena Horvat, Prof. Dr. Marjana Regvar, Dr. Darja Mazej, and Dr. David Heath for generously providing their knowledge, resources, and time in support of my work. Special thanks and acknowledgment go to my father, Prof. Dr. Marko Kranjc for assistance with the surface free energy calculations presented in this work. I would also like to thank my fellow colleagues: Marta Jagodic, Dr. Monika Kos, Luka Pirker, Dr. Bojana Višić, Dr. Tome Eftimov, Maja Koblar, Dr. Martina Lorenzetti, Dr. Ana Varlec, Alenka Malovrh, and everyone else who contributed to my work in and out of the laboratory, whether it was showing me how to use a piece of equipment or properly prepare a sample, watering my test plants, and/or providing useful ideas and advice to improve the quality of my work. Finally, I would like to thank my husband and family for their ceaseless encouragement. Financial support for my work was provided by the ERA Chair for isotope techniques in food quality, safety and traceability (ISOFOOD project; grant No. 621329).

Abstract

The purpose of this dissertation was to examine inadvertent food and edible plant exposures to nanoparticles (NPs) in the context of NP emission and deposition from air. This was investigated in terms of: 1) the emitted NP dynamics and characteristics of two types of incense sticks (Strawberry and African Violet) burned in an unventilated room setting and 2) the impact of foliar surface free energy (SFE), a quantitative measure of polar and dispersive forces which determine hydrophobicity/hydrophilicity, on the adhesion and translocation behaviors of arugula (`Eruca sativa Mill.`; low SFE) and escarole (`Cichorium endivia L.`; high SFE) plants after exposure to Pt NPs.

In the first part of this work, scanning mobility particle sizer results showed that the maximum total NP concentration at the end of the burning period was up to 30-fold higher than that of the initial background levels and that it remained up to six-fold higher 100 minutes after the conclusion of the burning period. Emitted incense particles decayed in a biexponential manner, with particles up to 100 nm in size decaying with lifetimes of several tens of minutes on account of fast agglomeration, while the particles with diameters of 100-1,000 nm had lifetimes of >100 minutes, as their removal mechanisms are slower. Slight distance-dependent effects were also observed, with the total NP concentration being higher at decreasing distances to the measurement inlet due to greater proportions of short-lived nucleation mode particles with size up to 100 nm.

In the second part of this work, soil-cultivated arugula and escarole plants were exposed to Pt NPs through either the leaves (5-500 mg/L for 5 days) or roots (one exposure to 20 mL of a 50 mg/L dispersion). Among foliar-exposed plants, inductively coupled plasma-mass spectrometry data showed that relative to escarole, arugula contained higher Pt concentrations in leaves (33, 31, and 14 times higher for 5, 50, and 500 mg/L exposures, respectively). For both plants, the proportion of Pt translocated from roots to leaves (99% and 28% for arugula and escarole, respectively) was higher than that from leaves to roots (<1% for both plants). Scanning electron micrographs of foliar-exposed leaves (500 mg Pt NPs/L) showed a much higher degree of Pt NP aggregation/agglomeration on arugula relative to escarole, in addition to stomata closure from likely shading effects on arugula. Analysis of foliar SFE results based on acid-base theory did not indicate any relationship between Pt NP exposure and changes to SFE.

The results of the incense experiments provide a model of NP air pollution in a typical indoor room setting, indicating that the inadvertent contamination of food with NPs is likely to be significant when placed alongside burning incense and other significant NP emitters (e.g., burning cigarettes). In outdoor settings, the results indicate that plants with low SFE are more susceptible to NP foliar exposures than plants with more hydrophilic surfaces.

Povzetek

Namen pričujoče disertacije je bil preučiti nenamensko izpostavljenost hrane in užitnih rastlin nanodelcem iz zraka, tako s stališča njihovega sproščanja v ozračje kot nalaganja na površine rastlin. To smo preučevali na dva načina: 1)z meritvami dinamike in karakteristik sproščenih nanodelcev med tlenjem dveh vrst kadilnih palčk (Jagoda in Afriška vijolica) v neprezračenem prostoru in 2) z meritvijo učinka površinske energije listov (PE) – kvantitativno merilo polarnih in disperzivnih sil, ki določa hidrofobnost/hidrofilnost – na adhezijo nanodelcev in njihov prenos (translokacijo) v rukoli (Eruca sativa Mill.; nizka PE) in endiviji (Cichorium endivia L.; visoka PE) po izpostavljenosti nanodelcem platine (Pt).

V prvem delu disertacije so rezultati merilnika SMPS ('scanning mobility particle sizer') pokazali, da je bila največja številska koncentracija nanodelcev ob koncu tlenja kadilne palčke do 30-krat višja kot je bila koncentracija pred tlenjem in da je ostala do 6-krat višja še 100 min po končanem tlenju. Število sproščenih nanodelcev iz kadila se je zmanjševalo na biekspонentni način: število delcev z velikostjo do 100 nm se je zmanjševalo z življenjsko dobo nekaj deset minut na račun hitre aglomeracije, medtem ko so imeli delci s premeri 100-1,000 nm življenjsko dobo >100 minut, saj so njihovi mehanizmi ozločanja iz ozračja počasnejši. Opazili smo tudi rahle, od razdalje odvisne učinke, kjer je bila skupna koncentracija nanodelcev višja na manjših razdaljah do vhoda merilne naprave zaradi večjega deleža kratkoživih nanodelcev z velikostjo do 100 nm.

V drugem delu pričujočega dela so prikazani rezultati raziskav v zemlji gojenih solat, rukole in endivije, ki sta bili izpostavljeni nanodelcem Pt bodisi preko listov (5-500 mg/L, 5 dni) ali korenin (ena izpostavljenost do 20 mL disperzije s koncentracijo 50 mg/L). Med listno izpostavljenimi rastlinami so podatki masne spektometrije z induktivno sklopljeno plazmo pokazali, da je rukola glede na endivijo vsebovala višje koncentracije Pt v listih (33-, 31-, in 14-krat višje za izpostavljenosti 5, 50, in 500 mg/L). Za obe rastlini je bil delež prenesene Pt od korenin do listov (99% za rukolo in 28% za endivijo) višji kot od listov do korenin (<1% za obe rastlini). Slike vrstične elektronske mikroskopije izpostavljenih listov (500 mg nanodelcev Pt/L) so poleg zaprtja listne reže stomate zaradi verjetnih senčnih učinkov na rukolo pokazali tudi mnogo višje stopnje agregacije/aglomeracije nanodelcev Pt na rukoli kot na endiviji. Analiza rezultatov meritve površinske energije, ki temelji na teoriji kisline-baze, ni pokazala nobene povezave med izpostavljenostjo nanodelcem Pt in spremembami PE.

Rezultati eksperimentov s kadilom predstavljajo model onesnaženja zraka z nanodelci v tipičnih stanovanjskih prostorih, kar kaže na to, da lahko pride do nenamerne onesnaženosti živil z nanodelci, če so izpostavljena tlečim kadilom in drugim večjim virom nanodelcev (npr. tleče cigarete). V zunanjem zraku pa rezultati kažejo, da so rastline z nizko površinsko energijo bolj dovzetne za onesnaženost listov z nanodelci kot rastline z bolj hidrofilnimi površinami.

Contents

List of Figures **xv**

List of Tables **xvii**

Abbreviations **xix**

Symbols **xxi**

Introduction **1**
1.1 Nanoparticles 1
1.1.1 Characteristics 1
1.1.2 Sources and Sinks 1
1.2 Nanoparticles in Air 2
1.2.1 Nanoparticle Measurement and Collection from Air 4
1.2.2 Incense Burning as a Health Hazard and Source of Nanoparticles in Air 10
1.3 Nanoparticles in Aquatic Environments 11
1.4 Nanoparticles in Soil 13
1.5 Nanoparticles in Food 16
1.6 Nanoparticle Measurements and Collection from Food and Other Biological Matrices 18
1.6.1 Fractionation Techniques 18
1.6.2 Electron Microscopy 19
1.6.3 Spectroscopy 19
1.6.4 Mass Spectrometry 20
1.6.5 Brunauer Emmett Teller Method 22
1.7 Risk Assessment and Application to Nanoparticles 22
1.7.1 Nanoparticle-gut Interactions 23
1.7.2 Potential Mechanisms of Nanoparticle Toxicity 27
1.8 Plant Exposure to Nanoparticles 28
1.8.1 Plant Exposure to Atmospheric Deposits and Foliar Adhesion 28
1.9 Nanoparticle Uptake Mechanisms and Translocation in Plants 29
1.9.1 Roots 29
1.9.2 Leaves 32
1.9.3 Cellular Uptake 35

Aim of the Work **37**

Materials and Methods **39**
3.1 Incense 39
3.1.1 Incense Burning Protocol 39
3.1.2 Chemical Analysis of Unburned and Burned Incense 40

3.1.3 Nanoparticle Distributions and Concentrations 41
3.2 Pt Nanoparticles 41
3.3 Arugula and Escarole Plants 42
3.3.1 Cultivation and Exposure to Pt Nanoparticles Through Leaves and Roots 42
3.3.2 Foliar Surface Morphology 44
3.3.3 Foliar Surface Free Energy 44
3.3.4 Pt Nanoparticle Adsorption Patterns on Foliar Surfaces 46
3.3.5 Pt Measurement in Leaves and Roots 46
3.3.6 Statistical Analysis 47

Results and Discussion **49**
4.1 Incense Powder and Emission Characteristics 49
4.1.1 Incense Chemical Analysis 49
4.1.2 Size Distributions and Concentrations of Emitted Incense Particles 53
4.1.3 Size-Specific Mass Distribution of Emitted Incense Particles 61
4.1.4 Discussion 62
4.2 Arugula and Escarole Responses to Pt Nanoparticle Exposure 64
4.2.1 Pt Nanoparticle Characterization 64
4.2.2 Leaf Surface Characteristics and Pt Nanoparticle Adsorption Patterns . 68
4.2.3 Surface Free Energy Response to Pt Nanoparticle Exposure 71
4.2.4 Pt Concentrations in Leaves and Roots to Assess Translocation 75
4.2.5 Discussion 81

Conclusions **85**

Numerical and Surface Free Energy Solubility Parameter Values **89**

References **109**

Bibliography **125**

List of Figures

Figure 1.1: Diagram of NP sources and pathways in the environment 2
Figure 1.2: Factors affecting atmospheric aerosol formation and particle deposition..... 3
Figure 1.3: Engine exhaust particle characteristics. 4
Figure 1.4: An example of equivalent diameters of an irregular particle 5
Figure 1.5: Schematic diagram of two cascade impactors in series 7
Figure 1.6: Schematic diagram of a DMA..... 8
Figure 1.7: Schematic diagram of a WCPC 9
Figure 1.8: The time-dependent evolution of a particle size distribution..... 10
Figure 1.9: Important aggregation factors 12
Figure 1.10:Electrophoretic mobility of magnetite NPs..... 13
Figure 1.11:Diagram of DLVO theory 15
Figure 1.12:Possible sources of dietary NP exposures..... 17
Figure 1.13:Electron beam interactions with samples in (a) TEM and (b) SEM. 19
Figure 1.14:Schematic diagram depicting the main components of an ICP-MS 21
Figure 1.15:Examples of adsorption isotherms. 22
Figure 1.16:Transection of gut epithelium with possible routes for NP transcytosis..... 24
Figure 1.17:Diagram depicting `in vivo` NP biodistribution 26
Figure 1.18:Optical micrographs of `P. guineense` leaf cross sections 29
Figure 1.19:Possible NP pathways into roots 30
Figure 1.20:TEM micrographs of Ag NPs in `Arabidopsis thaliana` root tissue 32
Figure 1.21:Leaf structure and NP uptake and leaf to root translocation pathways..... 33
Figure 1.22:SEM micrographs showing NPs in and around stomata..... 34
Figure 1.23:Possible internalization and translocation pathways in plants. 35
Figure 1.24:Diagram of NP uptake pathways into cells 36
Figure 3.1: Schematic diagram of the incense burning testing room..... 39
Figure 3.2: Preparation of foliar exposed arugula and escarole leaf samples..... 42
Figure 3.3: Representative plant photographs of the cultivation and exposure setup..... 43
Figure 3.4: Schematic diagram representing the four variables in Young's equation..... 45
Figure 4.1: Incense XRD spectra 50
Figure 4.2: Detailed incense XRD spectra 51
Figure 4.3: SEM micrographs of both incense types. 52
Figure 4.4: Incense NP distribution plots and TPC evolution..... 54
Figure 4.5: Incense NP distribution plots 55
Figure 4.6: Incense total concentration dynamics for different particle sizes 57
Figure 4.7: Incense TPC as a function of combusted mass..... 58
Figure 4.8: Incense TPC with normalized data fitted to a biexponential function 59
Figure 4.9: Incense particle size distribution spectra for selected timepoints..... 60
Figure 4.10:SEM micrographs of African Violet incense..... 62
Figure 4.11:Results of Pt NP characterization 65
Figure 4.12:SEM micrographs of arugula and escarole abaxial foliar surfaces..... 68
Figure 4.13:Photographs of arugula (a, b) and escarole (c, d) plants at harvest..... 70

Figure 4.14:Foliar SFE values accompanied by trend lines..... 71
Figure 4.15:Characteristic images of water droplets 72
Figure 4.16:Photographs of arugula plants 75
Figure 4.17:Pt concentrations of arugula and escarole leavces (a) and roots (b)..... 77

List of Tables

Table 3.1: Humidity and temperature at the beginning of each measurement. S and AV stand for Strawberry and African Violet incense, respectively. The number next to the incense abbreviation indicates the distance of the incense from the measurement inlet while the number following the hyphen indicates the repetition (from 1 to 3). Therefore, e.g., S15-1 denotes the first measurement of the Strawberry incense placed 15 cm from the inlet. 40
Table 4.1: Elemental composition of the two incenses before and after combustion expressed as wt.%. S = Strawberry incense; AV = African Violet incense. 49
Table 4.2: EDX analysis of Strawberry and African Violet incense. S = Strawberry incense; AV = African Violet incense; C1-C3, F1-F5, I1-I5, and L1-L6 refer to the corresponding image (c, f, i, l) and position number in Fig. 4.3. 53
Table 4.3: Physical and emission characteristics of Strawberry and African Violet incense. S = Strawberry incense; AV = African Violet incense; 15, 100, 300 refer to distance from the measurement inlet in centimeters; 1, 2, 3 refer to the trial run. 56
Table 4.4: Burning duration and TPC for the total burning period and the 60 min post-burning period, as well as biexponential time constants for Strawberry and African Violet incense. S = Strawberry incense; AV = African Violet incense; 15, 100, 300 refer to distance from the inlet in centimeters; 1, 2, 3 refer to the trial run. 57
Table 4.5: EDX analysis of African Violet incense collected from a DLPI, corresponding to points in Fig. 4.10c and Fig. 4.10f. 62
Table 4.6: Pt NP experimental concentrations and dissolution. All data are mean ± SD (n = 3). *The dissolved Pt fraction (%) is provided in terms of ultracentrifugation in the cases of Pt NPs dispersed in water (5, 50, and 500 mg/L) and in terms of ultrafiltration in the cases of Pt NPs and arugula and Pt NPs and escarole. 67
Table 4.7: Characterization of stomata on arugula and escarole foliar surfaces. All data are mean ± SD (n = 10). *Significant difference from the control according to the Mann-Whitney test ($p < 0.05$). 69
Table 4.8: Dry weight leaf masses of arugula and escarole at harvest. All data are mean ± SD (n = 3, 5 plants per replicate). *Significant difference from the control according to the Mann-Whitney test ($p < 0.05$). 70
Table 4.9: Contact angle values for ultrapure water (W), diiodomethane (DM), and glycerol (G) on unexposed abaxial and adaxial arugula and escarole foliar surfaces to examine the effect of aging on SFE (three-liquid acid-base theory method). Measurements were completed every other day over a 10 day period, starting from the day on which Pt NP exposure would begin. All data are mean ± standard deviation (SD; n = 5 per liquid). 72
Table 4.10: Contact angle values from ultrapure water (W), diiodomethane (DM), and glycerol (G) on abaxial and adaxial arugula and escarole foliar surfaces before and following each day of foliar exposure to 5, 50, and 500 mg Pt NPs/L dispersion. All data are mean ± SD (n = 5 per liquid). 73

Table 4.11: Preliminary results: arugula leaf and root Pt concentrations as a function of exposure period (four weeks and one week).Unless otherwise notated, data are mean ± standard error (SE; number of replicates [n] = 3, 5 plants per replicate). *Data are mean ± SE (n = 2, 5 plants per replicate). †Significant difference between like exposure groups on the basis of exposure time according to the Mann-Whitney test ($p < 0.05$)... 75
Table 4.12: Pt concentrations in arugula and escarole leaf and root samples. All data are mean ± SE (n = 3, 5 plants per replicate). 78
Table 4.13: Total quantities of Pt in whole arugula and escarole plants (leaves and roots), and in leaves and roots. All data represent means from triplicate measurements for each replicate (n = 3, 5 plants per replicate). A = arugula; E = escarole; F = foliar exposure; R = root exposure. *Although it was not possible to remove all root tissue from the soil media, care was taken to remove as much as possible. 78
Table 4.14: Repeatability (expressed as SD and %RSD) of Pt measurements in arugula and escarole leaf and root samples. For all data n = 1, 5 plants per replicate. 79
Table 4.15: Soil pH values at harvest. All data are mean ± SD (n = 3)..... 80
Table 4.16: Proportion of open stomata (%) on abaxial and adaxial arugula surfaces with Pt NP foliar exposure (control, 50, and 500 mg/L). All data are mean ± SD (n = 10). *Significant differences from the control according to the Mann-Whitney test ($p < 0.05$). **The boundaries between areas where droplets of Pt NP dispersion were applied and areas where droplets were not applied is very clear since the droplets did not spread out over the arugula leaf surfaces. 81
Table 5.1: Complete numerical SFE and solubility parameter values for abaxial and adaxial arugula and escarole foliar surfaces before and following each day of foliar exposure to 5, 50, or 500 mg Pt NPs/L dispersion. All SFE (γs), solubility parameter (δ), and dispersive, non-dispersive, electron-donor, and electron-acceptor force component values (γsd,) *Significant differences from the control according to the Mann-Whitney test ($p < 0.05$). **The boundaries between areas where droplets of Pt NP dispersion were applied and areas where droplets were not applied is very clear since the droplets did not spread out over the arugula leaf surfaces. 90

Abbreviations

%RSD	... % relative standard deviation
AB	... acid base
ADME	... absorption, distribution, metabolism, and excretion
BET	... Brunauer Emmett Teller method
BMD	... benchmark dose
CCC	... critical coagulation concentration
CPC	... critical particle concentration
CTAB	... cetyltrimethylammonium bromide
DDL	... diffuse double layer
DLPI	... Dekati low-pressure cascade impactor
DLS	... dynamic light scattering
DLVO	... Derjaguin-Landau-Verwey-Overbeek
DMA	... differential mobility analyzer
DNA	... deoxyribonucleic acid
DOC	... dissolved organic carbon
DW	... dry weight
EC	... European Commission
EDX	... energy dispersive X-ray spectroscopy
ENP	... engineered nanoparticle
EU	... European Union
GI	... gastrointestinal
HA	... humic acid
ICP-MS	... inductively coupled plasma-mass spectrometry
LOAEL	... lowest observable adverse effect level
LW	... Lifshitz-van der Waals
M/E	... mucilage and exudates
MPS	... mononuclear phagocytic system
MW	... molecular weight
MS	... mass spectrometry
NP	... nanoparticle
NNP	... natural nanoparticle
NOAEL	... no observable adverse effect level
NOM	... natural organic matter
PAH	... polycyclic aromatic hydrocarbon
PEG	... polyethylene glycol
PLGA	... poly(D,L-lactic/glycolic acid)
PM	... particulate matter
PNC	... particle number concentration
PZC	... point zero charge
QD	... quantum dot
QSAR	... quantitative structure-activity relationship

RNA	... ribonucleic acid
ROS	... reactive oxygen species
SD	... standard deviation
SE	... standard error
SEM	... scanning electron microscopy
SFE	... surface free energy
SMPS	... scanning mobility particle sizer
SP-ICP-MS	... single particle-inductively coupled plasma-mass spectrometry
SWCNT	... single-walled carbon nanotube
TPC	... total nanoparticle concentration
TEM	... transmission electron microscopy
UFP	... ultrafine particle
VOC	... volatile organic compound
WCPC	... water condensation particle counter
WHO	... World Health Organization
XRD	... X-ray diffraction

Symbols

B ... mobility
C_c ... Cunningham slip correction factor
C_P ... projected area concentration
d ... diameter
d_a ... aerodynamic diameter
Dp ... particle diameter
e ... electron charge
e_c ... cohesive energy density
F_D ... drag force
I_0 ... intensity of incident light beam
I_θ ... intensity of scattered light
k ... constant
Kn ... Knudsen number
m ... mass
n ... number of electron charges
n ... number of replicates
q ... particle charge
r ... radius
Re ... Reynolds number
S ... distance traveled by a particle
$S(\theta)$ ... particle scattering coefficient
St ... Stokes number
v ... velocity
Z ... electric mobility
α ... particle attachment efficiency factor
γ_l^- ... electron-donor component of the liquid
γ_l^+ ... electron-acceptor component of the liquid
γ_l^d ... dispersive force component of a liquid
γ_l^h ... hydrogen-bonding force component of a liquid
γ_{lv} ... liquid-vapor interfacial tension
γ_s^- ... electron-donor component of the solid
γ_s^+ ... electron-acceptor component of the solid
γ_s^d ... dispersive force component of a solid
γ_s^h ... hydrogen-bonding force component of a solid
γ_{sl} ... solid-liquid interfacial tension
γ_{sv} ... solid-vapor interfacial tension
δ ... solubility parameter
η ... gas dynamic viscosity
η_0 ... particle attachment efficiency
η_r ... particle transport and attachment efficiency

θ . . . angle
λ . . . mean free path
π . . . pi
ρ_p . . . particle density
τ . . . relaxation time
v_0 . . . initial velocity
χ . . . dynamic shape factor

Chapter 1

Introduction

1.1 Nanoparticles

1.1.1 Characteristics

Nanoparticles (NPs) may be defined by their dimensions (e.g. 100 nm or less in at least one dimension) and/or their size-dependent physico-chemical properties [1], [2]. Nanoparticles are too big to qualify as atoms or molecules, but they express quantum effects (e.g., electron confinement) in addition to high surface reactivity due to the significant proportion of constituent atoms and molecules at their surfaces [3]. The novel characteristics of NPs have made them attractive to a wide range of industries (i.e., biomedicine, cosmetics, food, electronics, construction, and environmental remediation), while their large surface area to volume ratios and high reactivity have raised concerns about their potential risks to human health and environmental safety [4], [5].

1.1.2 Sources and Sinks

Nanoparticles are extremely diverse, arising from natural environmental and biological processes as well as intentionally and unintentionally through anthropogenic activities. Nanoparticle sources and types can be categorized as incidental and anthropogenic. Incidental NPs can be created from wind and water erosion processes, chemical weathering processes (e.g., acid mine drainage), microorganism metabolic processes, natural combustion events (i.e., forest fires and volcanic eruptions), and atmospheric nucleation processes [6]. Incidental NP types include viruses and endotoxins, humic and fulvic acids, organic acids, organic colloids, pollen fragments, dust, sand, and soil fragments, and inorganic minerals and clays [7].

Anthropogenic NP sources include combustion processes, metal-smithing and welding operations, municipal waste incineration operations, automotive catalytic converters, material wear and tear (e.g., tire wear), and NP production facilities and products associated with the nanotechnology sector. Anthropogenic combustion processes include biomass burning, incomplete diesel-fuel combustion, and secondary aerosol formation from stationary and mobile sources, which include industrial boilers, fireplaces, vehicles, diesel trucks, and meat processing enterprises. Anthropogenic NP types can be divided into organic and inorganic NPs. Organic anthropogenic NPs include carbon black, carbon nanotubes, fullerenes, and other carbon-based compounds. Inorganic anthropogenic NPs include metals (Ag, As, Au, Fe, Ni, Pb, Pd, Pt, Rh, and Zn), metal oxides (of Al, Ce, Cu, Fe, Mg, Ni, Si, Sn, and Ti), and other metal compounds [1].

Nanoparticle sinks are mostly associated with the sources producing them. For example, the atmosphere is a primary sink for combustion-derived NPs, whereas soil and water bodies are more likely sinks for NPs originating from NP-containing materials or directly from the nanotechnology sector (e.g., from accidental releases during manufacturing, packaging, or shipping processes). More specifically, NPs may end up in soil through the dumping of NP-containing material into landfills or from the application of NP-containing sewage sludge to fields as fertilizer. Water bodies may become a sink for NPs through the deposition and migration of NPs from dumping sites into nearby water bodies [3], and from the atmospheric deposition of NPs contained in droplets of rain.

Due mostly to their small size, high concentrations, and ubiquity, the amounts of NPs in the environment are largely unknown. In order to provide some perspective, it is estimated that about one billion metric tons of atmospheric dust at the nano-scale are produced every year, whereas only a relatively meager few thousand tons of engineered NPs (ENPs) are produced per year [8]. Attempts to quantify environmental concentrations of ENPs are almost completely absent and can be attributed to a number of instrumental limitations which are discussed in Subsubsection 1.2.4.5. [9].

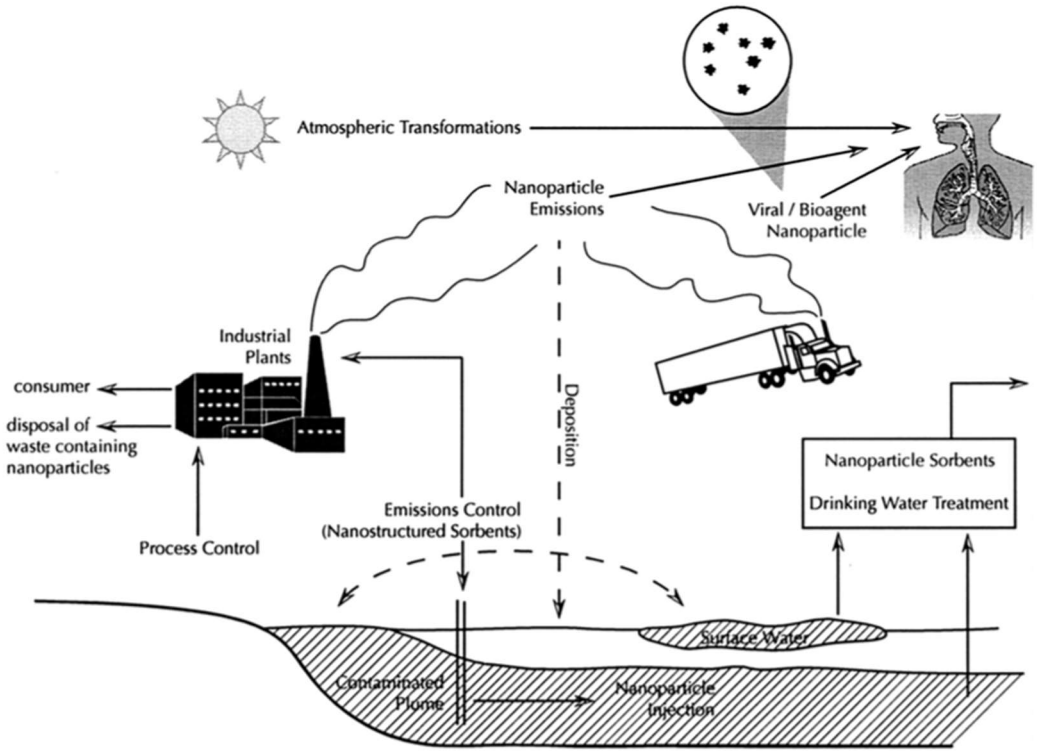

Figure 1.1: Diagram of NP sources and pathways in the environment[7].

1.2 Nanoparticles in Air

Nanoparticles are emitted into the air through three main processes. Combustion processes directly emit NPs into the atmosphere. Nanoparticles also form whenever hot supersaturated vapors undergo nucleation and condensation within a temperature gradient. Chemical reactions in the atmosphere constitute an indirect, but highly significant source of additional NPs [6], [10].

Particles in air are divided into several size categories, some of which share overlap with each other. Nucleation mode particles are 3-100 nm. Accumulation mode particles form a much larger category of particles spanning from 100-1,000 nm. These two categories of particles belong to the fine class of particles, which includes any particles less than 1000 nm. Particles larger than 1000 nm are categorized as coarse mode particles [11].

Nanoparticle concentrations and amounts in air are constantly evolving and mostly unknown. Nonetheless, emission inventories indicate that anthropogenic automobile exhaust is the main source of ultrafine particles (UFPs; i.e., NPs) in the atmosphere [12]. It is further estimated that anthropogenic emissions have more than doubled the amounts of UFPs in the atmosphere. In urban environments, it is estimated that over 80% of particle number concentrations (PNCs) consist of UFPs [13]. Normal number concentrations of UFPs are between 1 and $5 \times 10^4/\text{cm}^3$ whereas high number concentrations are around $3 \times 10^5/\text{cm}^3$ [10].

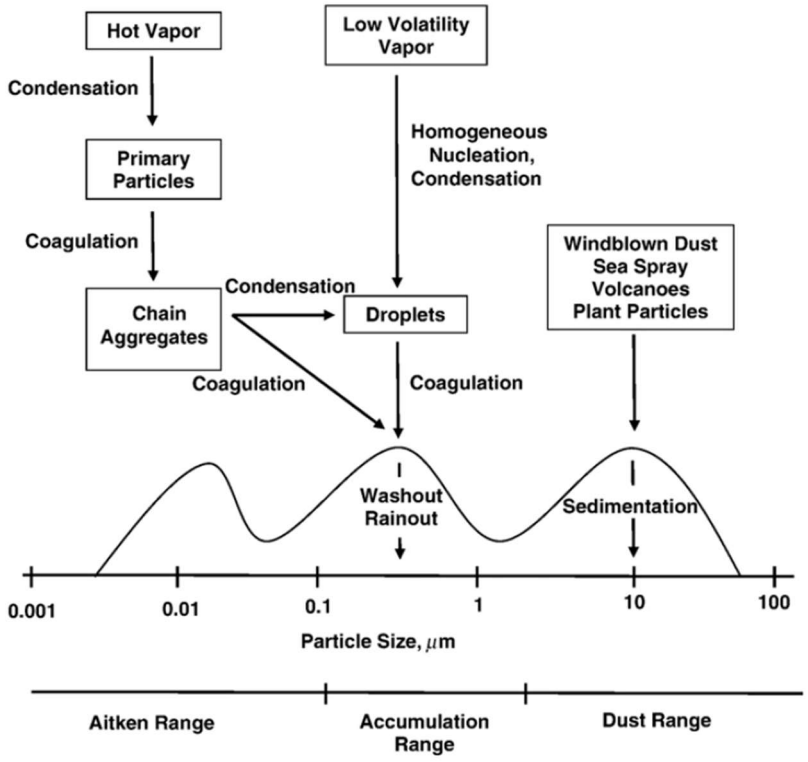

Figure 1.2: Factors affecting atmospheric aerosol formation and particle deposition [14].

The evolution of NP number concentrations in air can be attributed to nucleation, condensation, and coagulation processes. Ultrafine particles are produced wherever there exists vaporizable material, temperatures that are sufficiently high to produce vapors, followed by condensation and cooling within the presence of a large temperature difference [15]. Nucleation results when the partial pressure of the atmospheric gas is much greater than the vapor pressure of the nucleating substance(s) [11]. Therefore, nucleation is more likely to occur with substances of low volatility and low molar mass (e.g., sulfuric acid) [11], [16]. The effects of partial pressure, dilution ratio (i.e., the ratio of the nucleating species to air), and temperature on the nucleation process are proportional to each other in terms of their positive correlation with NP production. Nucleation is an extremely common process in the atmosphere and typically occurs in the form of water-sulfuric acid nucleation, water-sulfuric acid-ammonia nucleation, or ion-induced nucleation, with binary,

ternary, or organic vapors [11]. At particle concentrations greater than 100 μg/cm^3, condensation and coagulation become the primary mechanisms of particle dynamics [17].

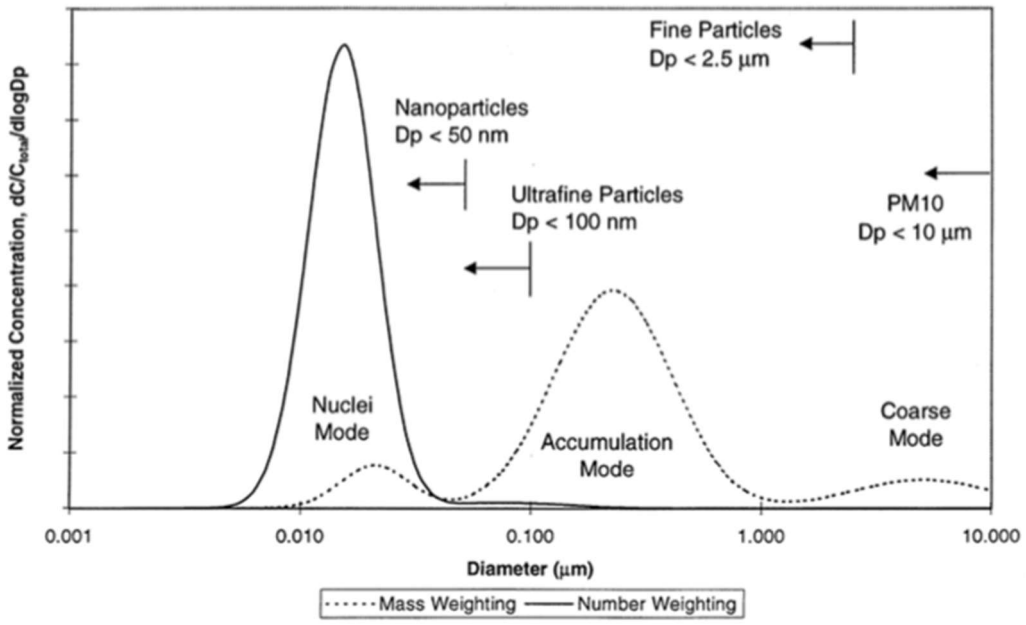

Figure 1.3: Engine exhaust particle characteristics. Particle size (i.e., particle diameter, [Dp]) distributions and concentrations of a typical engine exhaust in terms of mass and particle number [18].

The rationale behind the different particle size distribution categories is reflected in the different fates, transport mechanisms, and behaviors of particles within each category. Coarse mode particles are too large to remain airborne and usually settle within a timescale of hours. Nucleation mode particles (3 – 100 nm) typically only exist for about 15 minutes before coagulation mechanisms with accumulation mode particles dominate. Within this coagulated form, the initial nucleation mode particles and accumulation mode particles can remain airborne for about a week and can potentially travel for thousands of kilometers [18]. Ultrafine particles present unique safety and environmental health issues because they are highly reactive with surrounding materials in the atmosphere and can transport toxic substances such as oxidant gases, organic compounds, and transition metals which can then be inhaled by humans and deposited in the environment [10].

1.2.1 Nanoparticle Measurement and Collection from Air

Nanoparticle measurement techniques work by exploiting size-related characteristics. For example, by calculating the drag force on a particle due to the surrounding gas and comparing it with some other known force acting on it (e.g., gravity or an electrical force), it is possible to determine the NP size in terms of equivalent diameters. The aerodynamic diameter is the diameter of a spherical particle with a density of 1,000 kg/m^3 that possesses the same settling velocity as the particle being measured. The Stokes diameter is the diameter of a sphere with the same density and settling velocity as the particle being measured. The mobility diameter is the diameter of a sphere that moves in a constant electric field with the same velocity as the measured particle. Due to the appearance of quantum effects at the nano-scale, equations that describe the forces exerted on particles

at the bulk level require modifications when applied to NPs, while raising implications for NP measurement and collection [19], [20].

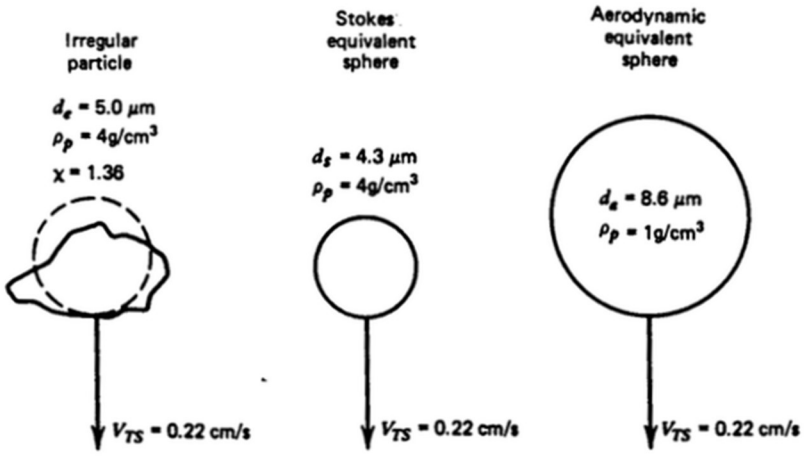

Figure 1.4: An example of equivalent diameters of an irregular particle[21].

The Knudsen number (Kn) is used to describe the flow regime of a gas around a particle, and hence differentiate between NPs and bulk materials. It is equal to the ratio of the mean free path (or average distance travelled by a particle between successive collisions with surrounding gas molecules), λ, to the radius of the particle, r:

$$\mathrm{Kn} = \frac{\lambda}{r} = \frac{2\lambda}{d} \tag{1.1}$$

When $\mathrm{Kn} \ll 1$, the particle exists in a continuum regime in which gas flow appears as an unbroken fluid due to the relatively large size of the particle in comparison to the size of gas molecules. For particles less than 1 μm in diameter, $\mathrm{Kn} \gg 1$ and particles approach the dimensions of individual gas molecules, existing in what is known as the free-molecular regime [22]. Such particles behave like large gas molecules, exhibiting Brownian motion (a kind of jerking movement) as a result of constant collisions with surrounding gas molecules. These collisions further result in diffusion (i.e., the net transport of particles down a concentration gradient) independent of external forces [22], [23]. In between the continuum regime and free-molecular regime is the transition regime in which $0.1 < \mathrm{Kn} < 1.0$ [22].

Stoke's law defines the drag force $\mathrm{F_D}$ of a fluid around a spherical particle of diameter d moving with velocity v in a fluid with gas dynamic viscosity η as:

$$F_D = -3\pi\eta v d. \tag{1.2}$$

This equation only works for particles in the continuum regime [22]. For particles in the free-molecular regime, a particle possesses a net velocity known as slip due to collisions with surrounding gas molecules. This has the net effect of decreasing the drag force, which leads to faster settling. To account for this effect, the Cunningham (slip) correction factor, C_c, must be applied in calculating drag:

$$C_c = 1 + \frac{\lambda}{d}\left[\alpha + \beta \exp\left(-\frac{\gamma}{2\lambda/d}\right)\right]. \tag{1.3}$$

In this equation α, β, and γ are experimentally determined constants specific to the system under consideration. By dividing the Stokes drag force by the Cunningham correction factor, the drag force can be appropriately modified for particles in the free-molecular regime [24]. The Reynolds number (Re) is a dimensionless value which provides additional information about the fluid flow around a particle, describing the velocity of a particle relative to the fluid in which it is moving. At low Re, the particle is said to move at approximately the same velocity as the fluid, and laminar flow occurs. At higher Re, turbulence occurs downstream of the particle [25].

The stopping distance and Stokes number, St, are used to evaluate particle size on the basis of the particle's inertia and ability to continue with a changing streamline. The distance S traveled by a particle traveling at an initial velocity v_0 with a relaxation time τ is:

$$S = v_0 \tau. \tag{1.4}$$

Relaxation time is related to mass:

$$\tau = mB = \rho_p \frac{\pi}{6} d^3 \left(\frac{C_c}{3\pi\eta d} \right) = \frac{\rho_p d^2 C_c}{18\eta} = \frac{\rho_0 d_a^2 C_c}{18\eta}. \tag{1.5}$$

In this equation, m is mass, B is mobility, ρ_p is the density of the particle, and d_a is the aerodynamic diameter. Equation 1.5 demonstrates that the stopping distance is only related to the mass (and hence inertial force) of the particle, and that in turn, it can be used to determine aerodynamic particle diameters. A larger relaxation time is indicative of greater mass and inertia. The Stokes number is the ratio of the particle stopping distance to the timescale that is characteristic of the flow distortion. A higher St indicates that the particle does not easily follow the streamline, whereas a lower St conveys the opposite [22], [23].

The same principles can be applied when a charged particle is placed in an electric field. The electric mobility, Z, of a charged particle below 1.0 μm placed into an electric field of unit charge is defined as:

$$Z = qB = neB = \frac{q\tau}{m} = \frac{neC_c}{3\pi\eta d}. \tag{1.6}$$

Here, q is particle charge, e is an electron charge, and n refers to the number of electron charges. One can see that electrical mobility is inversely related to mass.

Spherical particles are assumed in particle calculations, but this is rarely the case. To account for shape irregularities and resulting increased drag, a dynamic shape factor, χ, may also be applied to calculations alongside the Cunningham correction factor. The dynamic shape factor is the ratio of the drag force on the irregularly shaped particle to the drag force on a sphere of equal volume when moving at equal velocities and is applied by multiplying χ with the drag force. Equivalent diameters are used in measurement devices as a way to partly bypass the problem of irregular particle shapes [26].

The Dekati low-pressure, multi-stage cascade impactor (DLPI) provides mass-based particle size distribution concentrations on the basis of inertial impaction. Aerosol particles in the size range of 30 nm to 10 μm are collected and separated on 13 evenly spaced impactor stages on the basis of aerodynamic diameter (the diameter of a spherical particle with a density of 1,000 kg/m^3 that possesses the same settling velocity as the particle being measured). Each impactor stage consists of two plates: one with a varying amount of nozzles of different size to control the flow velocity of the incoming aerosol and another that serves as a collection plate [27]. Each impactor stage is given an experimentally

determined particle cut size value which specifies the particle size collected with 50% efficiency. It is not possible to obtain 100% efficiency because some larger particles bounce off the collection plate during sampling and end up on collection plates at lower stages designated for smaller particles, whereas some smaller particles adhere to collection plates at higher stages designated for larger particles [28].

Inside the DLPI, diffusion can lead to the movement of NPs away from a streamline, resulting in NP impaction at collection plates designated for larger particle sizes. Unlike air molecules, NPs have a tendency to agglomerate with each other and attach to surrounding surfaces [20]. Recall that due to their large surface area to volume ratios, NPs contain a disproportionate number of surface molecules and atoms, which leads to a certain amount of surface charge and enhanced reactivity [29]. Short-ranging van der Waals forces and surface tension from liquid films also play a role in enhanced NP surface adhesion [20].

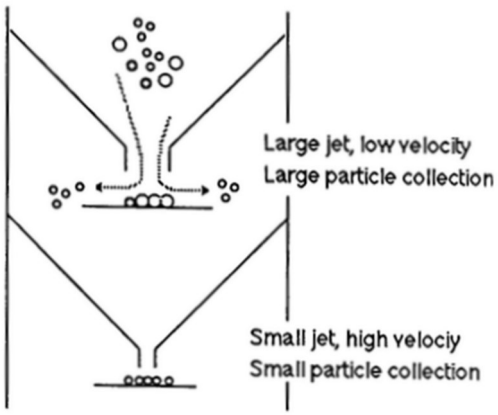

Figure 1.5: Schematic diagram of two cascade impactors in series [27].

After aerosol passes through the nozzle(s) of the first plate in the impactor stage, it is turned at a sharp 90° angle due to the internal geometry [27]. The ability of the particle to follow the streamline is dictated by the stopping distance and St. Particles of a larger mass are less able to follow changing streamlines. The St specifies the particle size that will impact on the collection plate, with a higher St indicating a higher likelihood of inertial impaction [22], [23], [30]. An attached pump at the base of the DLPI maintains a steady pressure of 100 mbar to control the sample airflow throughout the whole device [27].

A scanning mobility particle sizer (SMPS) provides real-time measurements of particles in air ranging from 7.5 nm to 1000 nm. Narrower size ranges are dependent upon the selected sample airflow rate. Aerosol inflow collected from a vacuum pump first passes through a desiccator to remove excess moisture. The aerosol continues by an inertial impactor, which removes particles above the maximum aerodynamic particle size being measured (i.e., the cut-point diameter) [19], [31].

The particles within the remaining aerosol are then divided into smaller size fractions for later counting on the basis of their electrical mobility. First, the aerosol is uniformly charged by ion-particle collisions in a neutralizer, with the aim of producing singly-charged particles. The charging process results in a distribution of particles containing no charge, single charges, and multiple charges. Although the charge distribution can be approximated by the Boltzmann equation, a modified equation must be used to estimate the charge distribution among very small particles in the free-molecular regime [32].

The charged aerosol then continues into a differential mobility analyzer (DMA) where a charge potential between two coaxial electrodes causes the NPs to separate according to their mobility diameter. At the top of the DMA, clean filtered air (i.e., the sheath airflow)

is directed through evenly spaced and sized radial holes and a mesh screen to ensure a smooth, even airflow towards the bottom of the DMA. The aerosol is separately pumped from the side into a separate narrow coaxial channel to ensure an even concentration of aerosol around the central electrode of the DMA. At the bottom of the narrow channel, the aerosol is directed into the main analyzing region where it joins with the clean sheath airflow. The clean airflow pushes the particles downwards and towards the outer part of the analyzing region, running parallel with the electric field produced by the coaxial electrodes. Particles with high electrical mobility cross through the sheath airflow, depositing onto the central electrode, whereas particles with low electrical mobility are carried out of the DMA with the main outlet flow [33]. Only NPs within a narrow size range have a unit charge that enables them to exit the DMA through a sampling slit. Throughout the course of every sample measurement, the potential within the DMA changes from smaller to greater in order to capture all size fractions of the aerosol [23], [31].

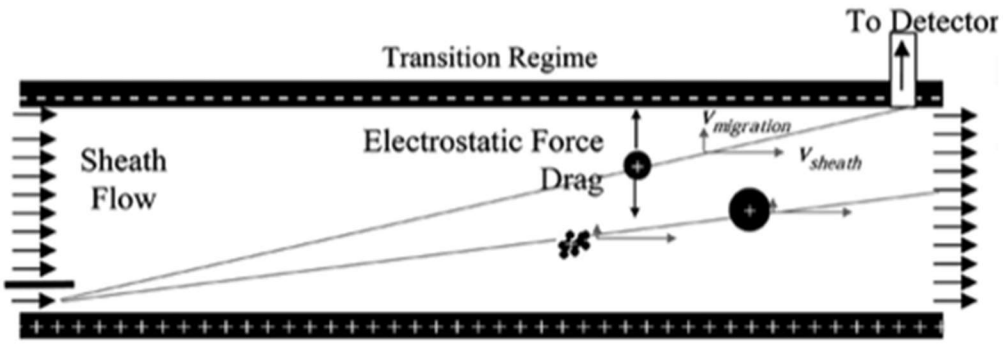

Figure 1.6: Schematic diagram of a DMA. The irregular particle has the same mass as the smaller spherical particle. Vector velocities are depicted by the arrows (the horizontal vector is due to the sheath flow and the vertical vector, movement from the electric field)[19].

After a specific size fraction has been separated from the rest of the collected aerosol, it travels to the water condensation particle counter (WCPC) for counting. There, particles are uniformly 'grown' with water condensation in an area of supersaturation achieved by convective cooling so that they are large enough for detection. Enlarged particles are then illuminated, and forward-scattered light (which is proportional to particle size and concentration) is measured by a detector. The intensity of scattered light at angle θ is given by:

$$I_\theta = \mathrm{k}\left[\frac{C_P S(\theta)}{\sin\theta}\right] I_0 \tag{1.7}$$

where I_0 is the intensity of the incident beam, C_p is the projected area concentration, k is a constant that includes information about the volume of aerosol onto which the light is incident and the angle at which it is received by the detector, and $S(\theta)$ is the particle scattering coefficient, or the ratio of light scattered by a particle per angle at an angle (θ) going in a forwards direction to the light geometrically incident on the particle. It is not usually possible to obtain this value. Individual air sample measurements are completed every few minutes. However, this time period can be modified by the user [23], [31].

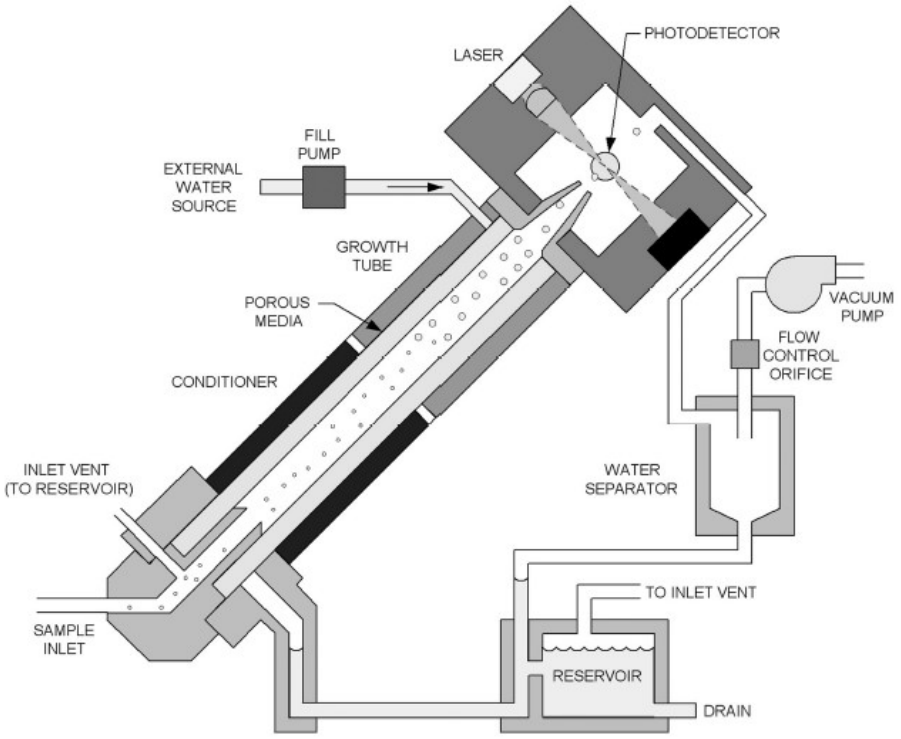

Figure 1.7: Schematic diagram of a WCPC [34].

After NPs have been collected and detected, information about the particle size distribution and PNC must be presented so as to accurately portray the relative and absolute concentrations of differently sized particles within a polydisperse aerosol. Because a typical aerosol contains less than 0.0001% particulate matter (PM) by mass or volume, gravimetric analysis is both impractical and inadequate for conveying the particulate load of an aerosol. Due to the very high relative number concentrations of NPs and the wide values of particle sizes normally collected and/or detected, results are best presented with the help of statistical tools [22]. When presenting PNCs, it is typical to express measurements in terms of units. A unit is defined as the total particle concentration in a measured particle size range (dN) divided by the difference of the logarithms of the differently sized particles (dp; i.e., the width of the size bin), leading to the unit: dN/(dlogdp). This unit provides normalized lognormal PNCs by size fractions, thus providing a way to easily view and compare number concentrations across particle size distributions without distortions due to differing widths between size bins [20].

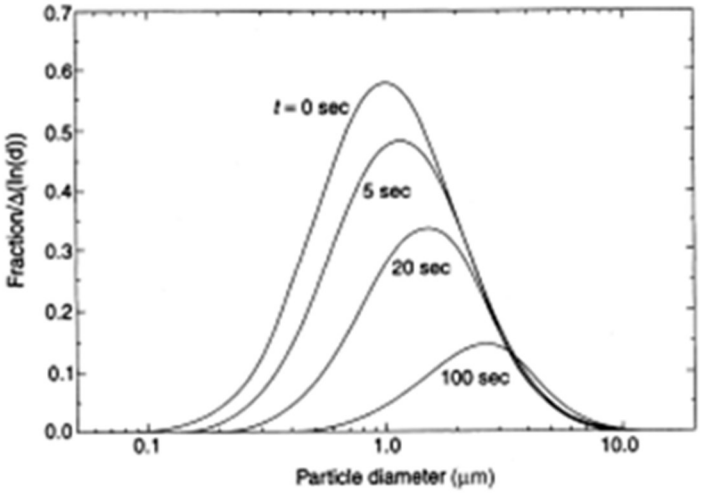

Figure 1.8: The time-dependent evolution of a particle size distribution in response to particle aggregation/agglomeration [22].

1.2.2 Incense Burning as a Health Hazard and Source of Nanoparticles in Air

Indoor activities, such as incense burning, can lead to extremely high, localized releases of UFPs into air. Incense combustion has been identified as a significant source of indoor PM and contaminant exposures due to its relatively widespread uses as an air freshener, insect repellent, and article of cultural expression and religious worship [35]–[37]. When compared with cigarette smoke emissions, another significant polluter of indoor air quality, incense emissions are comparable or greater [37]–[40]. Incense comes in many forms (e.g., cones, sticks, powders, rocks) and can be composed of numerous materials, including resins, aromatic plant materials, essential oils, and synthetic chemicals [41].

Despite its widespread appeal, harmful substances have been identified in incense smoke along with a number of adverse health impacts which have been attributed to its inhalation and deposition. Particulate matter in the form of solid particles and liquid droplets is abundantly present in incense smoke [41]–[43]. It was found that most of the airborne PM emitted from nine different types of incense sticks was smaller than 5.6 μm, with 95% of particles (by total weight) in this size range being smaller than 1.0 μm [44]. Carcinogens (e.g., polycyclic aromatic hydrocarbons [PAHs], volatile organic compounds [VOCs] such as benzene and 1,3-butadiene, and certain metals), suspected carcinogens (e.g., formaldehyde and acetaldehyde), irritants (e.g., acrolein and acetic acid), and allergens (e.g., geraniol) have also been detected in incense smoke [45]–[51]. Formaldehyde and acrolein concentrations were found in excess of World Health Organization (WHO) air quality guidelines in the interior and outside yard of a temple, as well as inside a home where incense was burned [46]. In a similar study, all types of PM (PM_{10} and $PM_{2.5}$) and benzene emissions from 10 types of incense exceeded the Recommended Indoor Air Quality Objectives for Office Buildings and Public Places in Hong Kong, while CO and formaldehyde limit objectives were exceeded by seven and six of 10 different types of tested incenses, respectively [38].

Particulate matter in the nanometer size range has a well-documented role in promoting pulmonary and cardiovascular disease due to its ability to enter the furthest (alveolar)

regions of the lung [43]. Reactive oxygen species (ROS) formation from interference with cellular mechanisms and inflammation can lead to fibrosis and cancer in the long term [52]–[54]. Furthermore, due to its large surface area and high reactivity, PM readily binds with metal(loids) and other pollutants in incense smoke increasing its oxidative capacity [35], [36]. In addition to exposure through inhalation, incense PM can be deposited onto exposed skin [55] and be ingested following deposition onto the surfaces of foods and drinks (e.g., if incense is burned to mask cooking odors) [56]. In previous studies, incense PM was found to cause dose-dependent oxidative damage in the Plasmid Scission Assay (particularly in the presence of metal[loid]s such as Cu) [36] and mutagenicity in the Ames Salmonella test [57]. Regular (i.e., daily) domestic incense use has been associated with decreased weight (among boys, but not girls) and head circumference at birth [58], decreased lung function among adolescents [59], and increased hypertension and blood pressure (especially among women) [60].

Although PM measurements have often been conducted using units of mass per unit volume, particle number concentrations per unit volume of air have been recognized as a more effective indicator of potential harm [22]. Currently, the European Union (EU) only sets a mass-based limit of 20 $\mu m/m^3$ for $PM_{2.5}$ over a 3-year averaging period (Directive/2008/50) [61]. Fine particle emission characteristics have been studied during incense burning [39], [42], [44], [62]–[65], however, fewer have studied particle decay following incense burning under conditions of low ventilation [53], [62], [66]. This information is relevant considering that different aerosol size fractions are known to exhibit different deposition characteristics, therefore affecting the relative level and duration of air pollution [67]. Two different studies described particle decay following incense burning, however this was completed in terms of mass per unit volume of air, and limited information was provided about the change in particle size distribution and concentration with time [53], [66]. In a third study in which particle decay was also investigated, the focus was on the dispersion of emitted particles to surrounding rooms within a multi-room domestic setting [62].

1.3 Nanoparticles in Aquatic Environments

Very few environmental modeling simulations or investigations into NP deposition and behavior in aquatic environments have been performed. Nonetheless, because NP concentrations are unknown and very difficult to track, aquatic colloids have been used as a predictive model. Aquatic colloids are within the same size range as NPs (1 nm – 1 μm) and are known to play a significant role in the chemistry, transport, and bioavailability of pollutants, nutrients, and microorganisms. Engineered NPs are expected to play a relatively minor role in comparison to natural NPs (NNPs)—whereas NNPs are present in concentrations of mg/L, ENPs are expected to appear in concentrations of μg/L.

Although NNPs are widely present at high concentrations in natural water and soil media, Handy et al. [8] argue that ENPs should still be taken seriously because (1) even certain naturally occurring NPs pose human and environmental health risks and (2) while NNPs quickly aggregate with other particles or become incorporated into natural materials, some ENPs may remain stabilized and available for much longer periods of time by intentional design (i.e., because of the addition of capping agents, such as surfactants). Despite findings from an environmental modeling simulation that potential quantities of Ag, TiO_2, and ZnO ENPs may pose risks to aquatic organisms based on known production rates, potential environmental emission routes, and ENP removal rates from the published literature, it was admitted that measurement uncertainties are very high due to a lack of information [9].

Aggregation mechanisms are extremely important to understanding the potential availability and risk of ENPs in aquatic environments. For example, NP aggregation with high molecular weight (MW) natural organic matter (NOM) is conducive to sedimentation and reduced availability whereas aggregation with low MW NOM is expected to increase availability and movement [12]. Various factors, including pH, ionic strength, dissolved mineral content, and organic matter content are expected to affect NP aggregation chemistry [8]. The speed of NP aggregation is described by aggregation kinetics which are divided into slow and fast aggregation regimes. The first stages of aggregation constitute the slow aggregation regime, which is reaction limited and strongly influenced by pH levels and ionic strength. At higher ionic strength, aggregation becomes more likely to occur because of decreasing energy barriers. The fast aggregation regime is diffusion limited and is not influenced by pH levels and ionic strength. The two regimes are separated by the critical coagulation concentration (CCC). At the CCC, energy barriers do not exist and aggregation is a function of Brownian diffusion [68]. Aggregation rates in aqueous media are dependent on particle-particle collision frequencies, collision energy, and attractive and repulsive charges on the colliding particle surfaces [8].

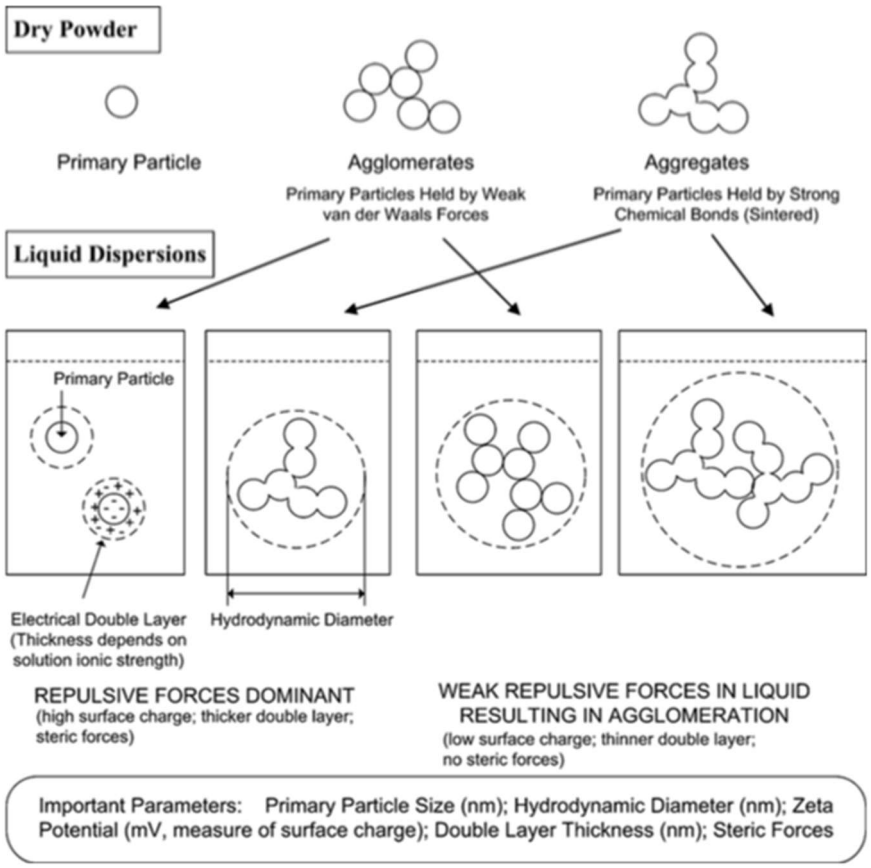

Figure 1.9: Important aggregation factors [69].

Another model for evaluating the potential aggregation and mobility of NPs in aquatic environments is the Derjaguin-Landau-Verwey-Overbeek (DLVO) theory. This theory states that the interaction energy between two compact, spherical particles results from attractive van der Waals forces and surface charge. If the kinetic energy of the particles moving in water (typically from Brownian motion) is greater than the repulsive forces,

aggregation occurs [70]. The thickness and zeta potential of the electrical double layer surrounding a particle also provides information on the likelihood of aggregation, with an increase in either leading to increased particle repulsion. Increases in ionic strength are accompanied by decreases in electrical double layer thickness. Steric repulsion is maintained across pH values and ionic strengths since it is the result of physical separation [69].

Experimental studies designed to measure the relative importance of different factors on aggregation kinetics have generally found that organic matter content far outweighs the impacts of pH, ionic strength, or NP material. In two different studies with similar findings, low and medium concentrations of amphoteric, negatively charged humic acid (HA) were found to stabilize negatively charged magnetite NPs under a range of pH values and ionic strengths due to NP surface charge modification from the binding of HA [68], [71]. Similar results were obtained using C60 fullerene NPs [72] and Ag NPs [73], [74]. Keller et al. [75] also found a high degree of NP stabilization from the addition of NOM regardless of NP material (i.e., TiO2, ZnO, and CeO2) and aqueous media (i.e., two different types of seawater, lagoon water, river water, and groundwater), although they found that increased ion strength resulted in increased aggregation. Organic matter is widely present in water bodies, signifying that NPs are likely to be stabilized in outdoor aqueous environments [68]. Since increased stabilization is correlated with decreased sedimentation, this implies that NPs are likely to be fairly mobile within typical aqueous environments with significant implications for potential contaminant and nutrient transfer over relatively large distances [1].

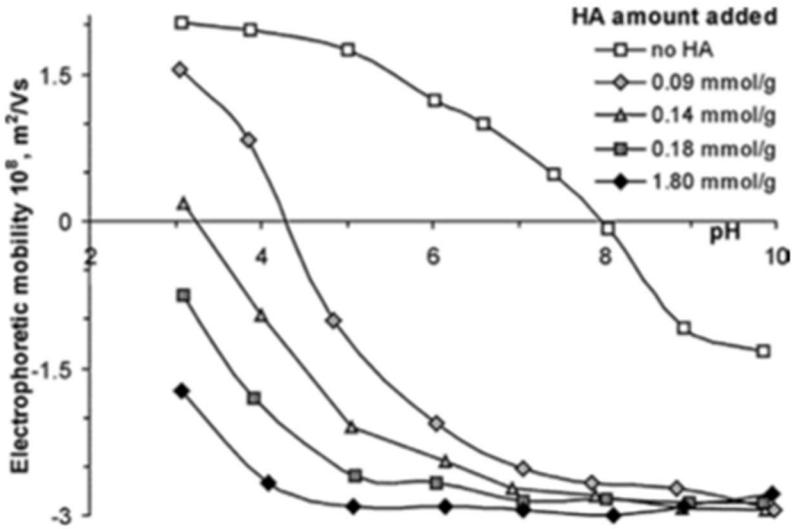

Figure 1.10: Electrophoretic mobility of magnetite NPs depicted as a function of pH at varying concentrations of HA in 0.002 mol/L NaCl solution [71].

1.4 Nanoparticles in Soil

Monitoring NPs in soil is a complicated endeavor due to the fact that large concentrations of organic and inorganic NPs already naturally exist in this matrix. Examples include clay minerals, metal (hydr)oxides of Al, Fe, and Mn, and humic substances. Humic substances include HA (which is alkali-soluble), fulvic acid (alkali- and acid-soluble), and humin

(alkali- and acid-insoluble). Nanoparticles in soil are responsible for carrying out a number of ecological services including water storage regulation and element cycling, binding and moving contaminants (e.g., volcanic allophane NPs which adsorb As), sequestering organic materials, and enhancing the bioavailability of plant nutrients [76]. Differentiating between natural background NPs and ENPs is an enormous challenge, which is reflected in the lack of research performed in this area [77]. Due to a lack of monitoring results of ENPs in soil matrices, findings from the field of colloid transport and colloid-contaminant adsorption are extrapolated to ENP mobility and behavior in soil.

As in aquatic environments, NP mobility (in this case, within water contained in pores) must be known to evaluate potential exposures and interactions between NPs, living organisms (e.g., plant roots and fungi hyphae), and contaminants [12]. This means that to a large extent, experimental findings from NP and colloid stability within aqueous media can be applied to NP mobility within soil matrices [68]. Many factors play a role in NP pore water mobility, but pore size, electrostatic charge, and NP agglomeration rate are the most relevant to soil experiments. Nanoparticle transport can be attributed mostly to direct interaction with soil particles and diffusion from Brownian motion [78].

Two main physical mechanisms can be used to explain particle immobilization in soil matrices. Fine particle filtration describes the processes of transport and attachment by which particles become trapped in pores that are larger than the particles. Particles are mobile so long as they flow with water streamlines, however, attachment may occur through electrostatic attractive forces, inertial impact, diffusion, and/or uneven forces that cause a particle to rotate, such as when one half of a particle moves in a faster streamline than the other side. *Straining* is used to describe particle immobilization that occurs when pore size is smaller than the size of the particle, thus leading to a physical blockage [79]. Clogging mechanisms—which occur when pores become clogged with a mass of particles smaller than the pore size—is also considered an important mechanism of particle immobilization [80].

The use of DLVO theory can be applied to NPs and soil particles to serve as a predictive model for NP mobility and behavior based on the sum of attractive and repulsive electrical forces. As already stated, DLVO theory is used to assess particle interactions by considering the relative strengths of attractive van der Waals forces and surface charges (or double layer charges). The potential energy between two particles is calculated by adding the diffuse double layer (DDL) and van der Waals forces and then dividing by the distance between them. The DDL potential results from the accumulation of ions at the surface of a charged particle to balance the particle surface charge [81]. As soil-suspended particles decrease in size, van der Waals forces and electrostatic forces become proportionally more significant in governing mobility and behavior. At higher ionic concentrations, NP agglomeration occurs, which leads to a larger role for van der Waals forces and a decreasing role for electrostatic forces [82].

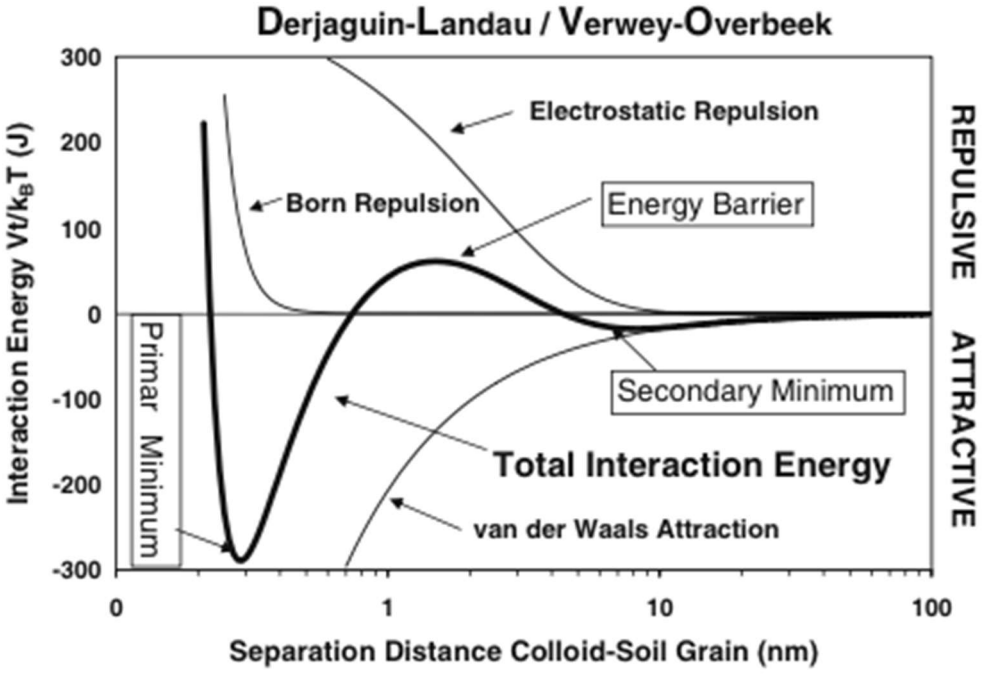

Figure 1.11: Diagram of DLVO theory illustrating the forces and energies that exist between a NP and soil grain [1].

Changes in chemical and hydrodynamic parameters can lead to the release of NPs from soil matrices. In chemically induced release processes, changes in the ionic strength and pH of pore water can lead to the release of particles. High pH and low ionic strength are specific features conducive to NP release [81]. Any addition of anions, surfactants, and reducing agents contributes further to this effect. In hydrodynamically induced release, the pore water flow velocity is high enough to dislodge particles. Dislodged particles tend to be larger because they experience a larger drag force than smaller particles, and the number of released particles increases with higher flow velocity. Analysis of hydrodynamic release is more complicated than chemical release because forces may act from different directions. Particles may experience a lifting force, a hydrodynamic force which causes the particle to slide, or torque, which causes the particle to roll [80].

Experimental results indicate that while organic content plays a large role in NP stability within soil matrices, surface charge appears to play an even larger role. In an analysis on Al NP migration through soil, moderately ionized conditions caused NP agglomeration, which restricted movement (as is the case in surface water conditions). In addition, particles with similar charges to the surrounding media travelled further than particles with charges that were opposite to those of the surrounding media [82]. Fang et al. [78], found that TiO_2 NP stability (and mobility) was positively correlated with dissolved organic carbon (DOC) and clay content in soil. Aggregation was more likely to occur with higher ionic strength, zeta potential, and pH, and resulted in lower mobility. Calculated maximum travel distances exceeded 30 cm in 10 days, signifying risks to deeper soil layers and groundwater environments.

In reference to current mobility and deposition models, experimental results have yielded some unexpected findings, pointing to the fact that mobility and deposition efficiencies are incompletely understood and not accurately described by current theories

and models. In studies by Lecoanet et al. [83], [84], C-based NPs (hydroxylated C_{60}, C_{60} clusters, and single-walled carbon nanotubes [SWCNTs]) in aqueous suspension did not follow expected predictions of velocity-dependent particle passage based on deposition theory when passed through a glass bead porous medium. For example, they did not exit the medium at increasing rates when subjected to a higher flow rate, and they were also found to exit at increasing rates with time, despite predictions that they would aggregate within the medium due to their hydrophobic characteristics. Based on prior knowledge of highly-ordered C_{60} NP stacking patterns, it was proposed that the stacking process is the rate-limiting step rather than mobility and deposition factors. In addition, the higher attachment efficiency of larger Si NPs did not correlate with DLVO theory, which predicts that smaller particles of the same material should have increased attachment efficiency due to decreased electrical potential between the particle and soil grains.

1.5 Nanoparticles in Food

The rapid growth of the nanotechnology sector has been said to outpace the Industrial Revolution with a predicted tenfold increase in value between 2009 and 2015 [2]. In the food industry, inorganic ENPs are being developed for applications as biosensors for toxins, microbes and food source traceability, food packaging additives for anti-microbial properties and enhanced durability, and as nano-encapsulated nutrients and additives for increasing nutrient bioavailability and absorption, coloring, and flavoring [85].

Given the unusual physico-chemical properties of NPs, their intentional addition into food and food packaging naturally raises concerns about their possible hazards, especially as they relate to oral exposure. Nanoparticle ingestion is potentially worrisome because their small size and high reactivity means that they can bypass cellular barriers. Toxicity studies have indicated that once inside the cell, NPs may cause a range of harmful outcomes from ROS formation and oxidative damage (i.e., cancer, immune reactivity, etc.) to necrotic cell death [86]. There is also evidence that they may act as carriers and distributors of microbes and contaminants [87]. While it is recognized that harmful effects are dictated by a NP's physicochemical properties, the effects of specific combinations of properties on toxicity and NP behavior remain poorly understood [88], [89].

With proposed uses for inorganic ENPs in the food industry comes a responsibility to ensure safety by properly assessing the risk associated with the oral ingestion of these substances. The completion of a risk assessment is dependent on the quantification of hazards and current and expected exposures. Nonetheless, completing these tasks is complicated by a number of unresolved issues including a lack of standardized vocabulary, inadequate study design protocols, and instrumental limitations in NP detection, to name just a few [90]. Presently, the lack of conclusive information about the potential toxicities and risks of ENPs is reflected in the absence of formal definitions and specific regulation in the food industry [91], [92].

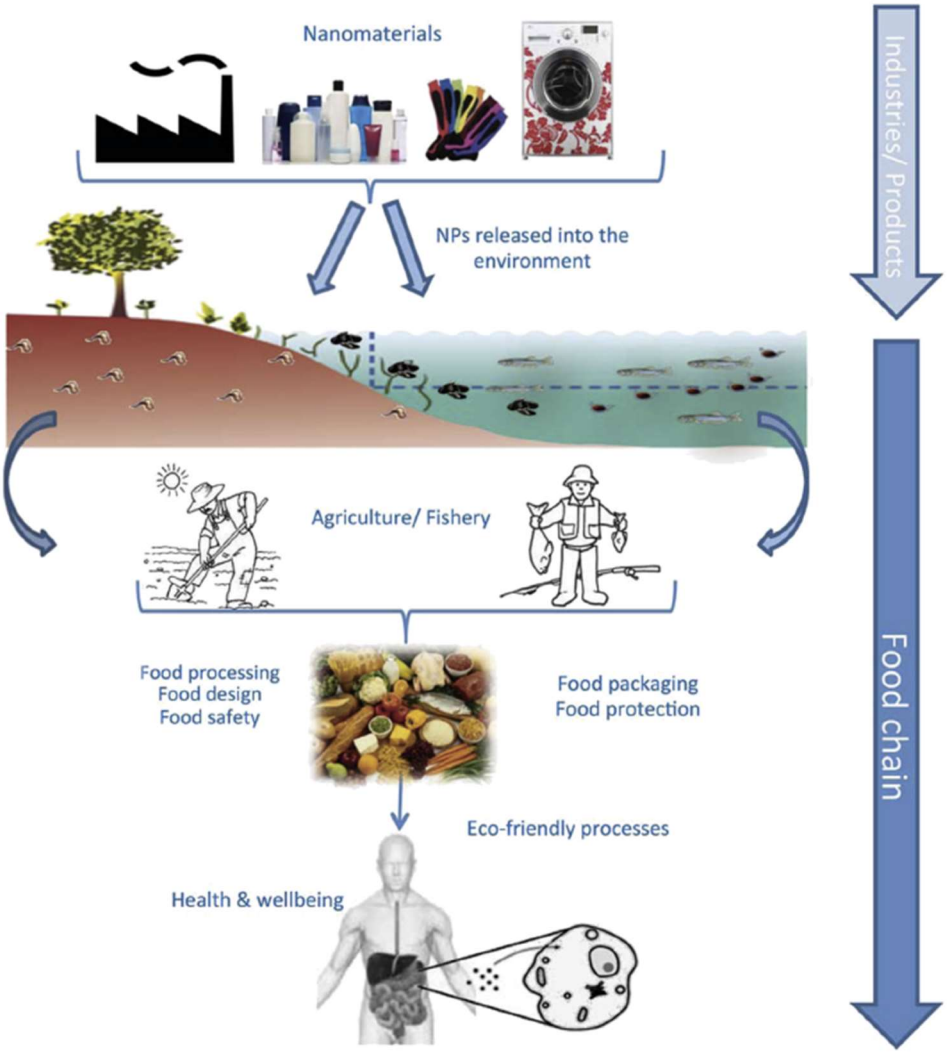

Figure 1.12: Possible sources of dietary NP exposures [93].

The growth of nanotechnology in the food sector has highlighted the likelihood that inadvertent NPs are present in food. Monitoring data of unintentional inorganic NP food contamination resulting from food production and processing practices is absent, although its likelihood has been voiced [85], [90], [92], [94]–[96]. It is plausible that inorganic NPs could be produced during the food production and processing stages through mechanical wear and tear during cutting, chopping, and other contact processes, and combustion associated with the use of machinery and/or indoor activities (e.g. smoking and incense burning). These NPs could in turn deposit onto food, comprising an unintended source of inorganic NP contamination.

The most relevant research regarding inadvertent food exposure to inorganic NPs deals with the foliar uptake of NPs from atmospheric deposition and from the manual application of NPs to plant leaves. Such studies demonstrate that atmospheric NP deposition can lead to inadvertent inorganic NP oral exposures if exposed plants are consumed and reveal the potential for exposure if plants are intentionally exposed due to the application of an agricultural nanotechnology.

1.6 Nanoparticle Measurements and Collection from Food and Other Biological Matrices

Of crucial importance for the rigorous assessment of NP ingestion risks and the creation and implementation of relevant legislation is the ability to accurately collect and measure NPs in food and other biological matrices (e.g., water and soil) which could come into contact with food during production and processing. When examining NP exposures, it is necessary to consider not just the individual particles, but also the size distribution of interest and PNCs. Food and other biological samples are complicated matrices containing many different substances of widely varying size. This makes NP detection and characterization in such samples a very complicated endeavor requiring many preparatory steps, instruments, and techniques [96].

According to Card and Magnuson [88], a thorough NP characterization for the purposes of toxicity evaluation should include a determination of: agglomeration and/or aggregation state, chemical composition, crystal structure/crystallinity, particle size/size distribution, purity, shape, surface area, surface charge, and surface chemistry (i.e., composition and reactivity). In addition, proper records should be kept of the media in which testing is completed to account for possible measurement discrepancies and artefacts. Despite the wide range of available instrumentation, very few can be used as an all-inclusive method in the analysis of complex samples. It is often necessary to analyze a single sample with multiple analytical techniques to provide an acceptable level of NP characterization [77]. Accurate measurement results often necessitate the extraction of NP analytes from complex biological matrices, although minimal interference is preferable to avoid artefacts and NP parameter changes. Digestion and fractionation (centrifugation and/or filtration) are often used for this purpose. Depending on whether the NP analyte(s) is organic or inorganic, additional steps may be required for effective isolation, such as chromatography or electrophoresis. After separation, analytical and characterization methods may then be used, encompassing microscopy, spectroscopy, and mass spectrometry [96]–[98].

1.6.1 Fractionation Techniques

Ultracentrifugation (which can reach accelerations of up to 1,000,000 g) is the centrifugation technique best suited to NP extraction. This technique can be further subdivided into analytical and preparative ultracentrifugation. In analytical ultracentrifugation, the use of an optical system (e.g., UV light absorption and/or interference optical refractive index system) makes it possible for the user to monitor the sample during use. Preparative ultracentrifugation is simply used to separate NPs within liquid samples. Generally, centrifugation is better suited for separating denser NPs which are more greatly influenced by their settling velocity than by Brownian motion. While this technique has the advantage of causing minimal disruption to particle characteristics, the descent of larger particles during centrifugation may lead to attachment and loss of smaller particles through aggregation/agglomeration [96], [97].

Filtration methods operate by passing a NP-containing solution through membranes containing pores of varying size. A typical membrane filtration system contains filters with holes of either 0.2 μm, 0.45 μm, or 1 μm. Despite its usefulness in separating NPs, an excessive operating sample flow speed, particle concentration, and/or electrostatic interactions between the membrane and particles can lead to filter-cake formation which leads to a reduction in pore size and the appearance of artefacts. Ultrafiltration and nanofiltration contain membranes with even smaller pore sizes (down to <1 nm in the case

of nanofiltration), however they are subject to a greater degree of filter-cake formation. [77], [97].

1.6.2 Electron Microscopy

Electron microscopy offers higher resolution than optical microscopy, but often requires extensive sample preparation (i.e., drying and application of a conductive coating), particularly if organic NPs are the subject of interest. Scanning electron microscopy (SEM) can be used to obtain three-dimensional images of sample NP surfaces to a resolution of ~0.2 nm. An electron beam from a heated source (e.g., a tungsten filament, LaB_6, Schottky emitter, or tungsten field-emission tip) is directed toward the sample surface by means of electron acceleration through an applied electric field, condenser lenses, and an objective lens. Surface images are recorded from the emission of low-energy, inelastically scattered secondary electrons and high-energy, elastically scattered backscattered electrons. The entire system operates in a vacuum, which prevents dispersion of the electrons by gas molecules and oxidation of the electron source [99], [100]. Transmission electron microscopy (TEM) is very similar to SEM except that the sample must be extremely thin (in the range of micrometers or nanometers). This technique is often used to examine sample cross-sections (e.g., to view internal cellular structures) rather than surface morphology. The sample image is created by non-transmitted electrons imaged onto a fluorescence screen or charge-coupled device camera. As in SEM, sample preparation is extensive and light elements (i.e., organic materials) require staining to be visible [77].

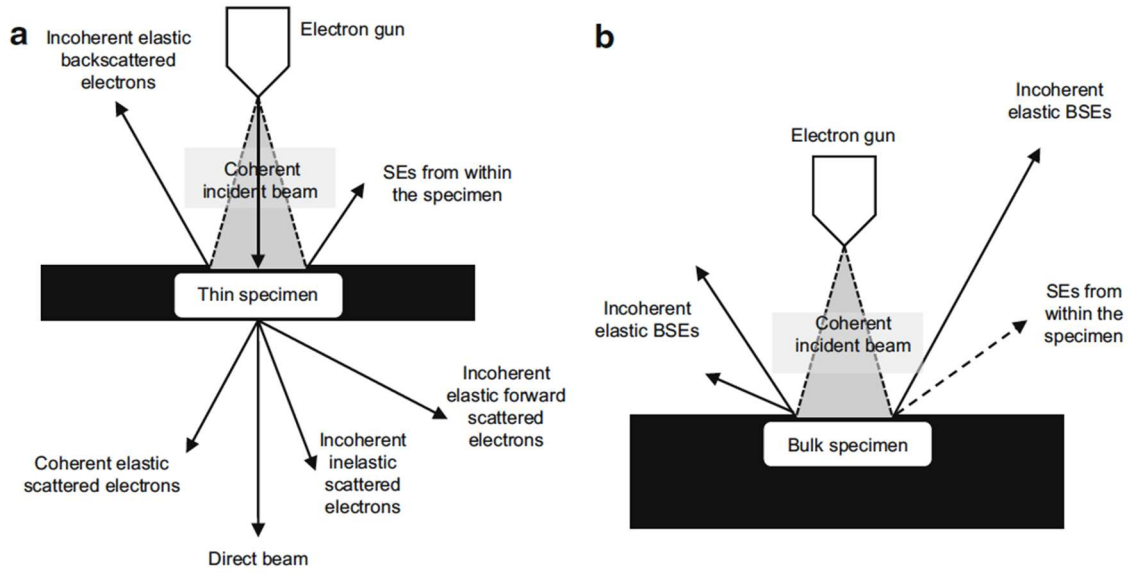

Figure 1.13: Electron beam interactions with samples in (a) TEM and (b) SEM. SE = secondary electrons, BSE = back scattered electrons [101].

1.6.3 Spectroscopy

Spectroscopic methods and techniques provide chemical information and NP sizes and size distributions of bulk samples on the basis of interactions between sample NPs and electromagnetic radiation (electromagnetic waves, photons, or electron beams) [102]. Light scattering spectroscopic techniques use a light sources (e.g., lasers, X-rays, or neutrons) to quickly determine NP sizes and size distributions by measuring the amount of scattering

from exposed particles. Dynamic light scattering (DLS; also known as photon correlation spectroscopy) is one such technique which is commonly used to measure the hydrodynamic diameter of particles in a dilute liquid suspension. Because the diffusion of a particle in solution is inversely related to its size, time-dependent light intensity fluctuations from illuminated particles can be used to measure this property. [77].

X-ray spectroscopic techniques use an electron beam to excite sample molecules and then use the resulting characteristic X-ray emissions for elemental and compositional analyses. Since quantum energy levels are specific to each element, the energy of the X-ray photons produced from the excitation and de-excitation of inner electrons can be used for chemical analysis. Energy dispersive X-ray spectroscopy (EDX) is often performed alongside electron microscopy analyses. Although it is useful for determining the chemical composition of elements heavier than oxygen, it is subject to high uncertainty (~20%) when used for quantitative analyses [99], [103].

X-ray diffraction (XRD) is a non-destructive analytical technique for inorganic and organic NPs in which X-ray beams are projected at an angle θ and diffracted rays are collected at an angle of 2θ. The results provide information about the chemical states, composition, and crystallographic structure of the sample. X-ray absorption spectroscopy (XAS) is used to locate local structural variations in NP samples (e.g., chemical bonding) that are not detectable using electron microscopy and XRD [104].

1.6.4 Mass Spectrometry

In its most basic form, mass spectrometry (MS) consists of an ionization source for gas-phase sample ionization, a mass analyzer for separating ionized sample components on the basis of mass-to-charge ratios (e.g., ion trap, quadrupole, time-of-flight, etc.) and a detector for measuring the amount of ions of each mass-to-charge ratio (e.g., Faraday cup, electron multiplier). Ionization sources can include an electron beam (produces positively charged ions and ion fragments) and a gas that has been ionized by an electron beam (reduces sample fragmentation and provides molecular weight information). Mass analyzers differ by the means used to separate the ionized particles (e.g., magnetic or electric field), as well as in range, sensitivity, and resolution. Variations in the choice of these components lead to different forms of MS—the techniques of greatest relevance for the detection of NPs in biological samples include: inductively coupled plasma MS (ICP-MS), single particle ICP-MS (SP-ICP-MS), and time-of-flight MS (TOF-MS) [96], [105].

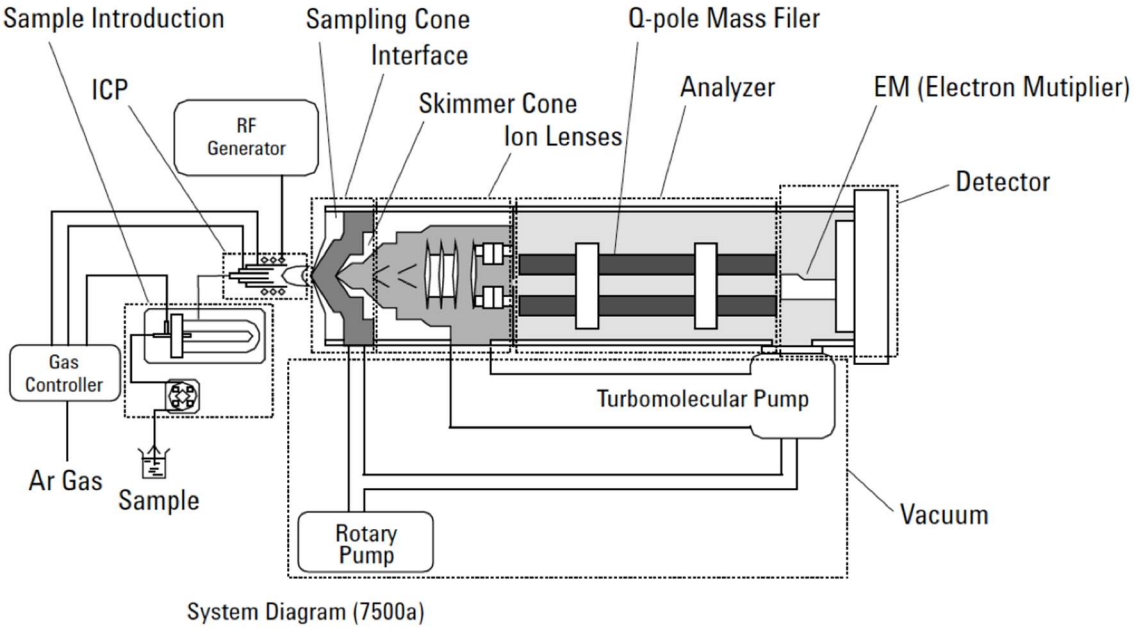

Figure 1.14: Schematic diagram depicting the main components of an ICP-MS [106].

With ICP-MS, it is possible to determine the elemental concentrations of a bulk sample with great speed and sensitivity (detection limits extend to the ng/L or ppt, range). During the first step of operation, a fine aerosol is created from a liquid sample passed through a nebulizer and temperature controlled spray chamber that removes larger aerosol droplets. The aerosol continues through heated argon plasma (up to 9,700°C) that dries, vaporizes, and atomizes the sample. The plasma is emitted in the center of a circular piece of highly charged, radiofrequency loaded copper wire. The high plasma temperature (up to 10,000 K) dries the aerosol droplets, which are decomposed, vaporized, atomized, and finally ionized, mainly as M^+ ions. The resulting positively charged ions are extracted into the vacuum system through a pair of interface (sample and skimmer) metal cones with small openings (≥1 mm) which make up the interface region. The interface region separates the high-vacuum ion focusing and MS portions of the ICP-MS from the preceding areas, which are maintained at atmospheric pressure. Here, grounding of the copper wire prevents secondary electrical discharge due to the large potential difference between the charged plasma and interface region, which would compromise the integrity of the ionized sample. Beyond the interface region, the ions are directed and focused by electrostatic lenses towards the mass spectrometer. In addition, the electrostatic lenses eliminate interfering species, such as oxides (i.e., a polyatomic ion containing an oxygen atom) and doubly charged species (i.e., an atom that loses two electrons instead of one), which decrease measurement accuracy. Once in the mass analyzer portion of the ICP-MS, the ions are separated on the basis of their mass-to-charge ratio. In a quadrupole mass analyzer, two sets of double metal rods have direct current (CD) and alternating current (AC) electrical fields placed on opposite rods such that only ions with one particular mass-to-charge ratio are able to reach the ion detector at the end. Throughout a measurement, the DC and AC currents are altered so that the concentrations of each ion are measured. The corresponding signals are detected and recorded to generate the results [107].

1.6.5 Brunauer Emmett Teller Method

Surface adsorption isotherms show amounts of adsorbate per unit mass of adsorbent as a function of pressure under constant temperature and are typically used when studying pollutant removal from wastewater and soil systems and for determining the specific surface area of solids (including NPs). A variety of surface adsorption isotherm models exist for different types of adsorbents (e.g., heterogeneous or homogeneous solids) and adsorbates (e.g., gas or liquid). Underlying these models is an assumption of thermodynamic equilibrium between the quantity of adsorbed and unadsorbed molecules of adsorbate [108], [109]. In the case of the Brunauer Emmett Teller (BET) method, an inert gas (usually N_2) is used to determine the specific surface area of a dry nanopowder. This model assumes molecular monolayering, uniform distribution of molecular attachment sites, lack of energy change with adsorption, and lack of interaction between adjacent adsorbed molecules. This method is deemed effective because NP aggregation/agglomeration does not affect the measurement [87], [108].

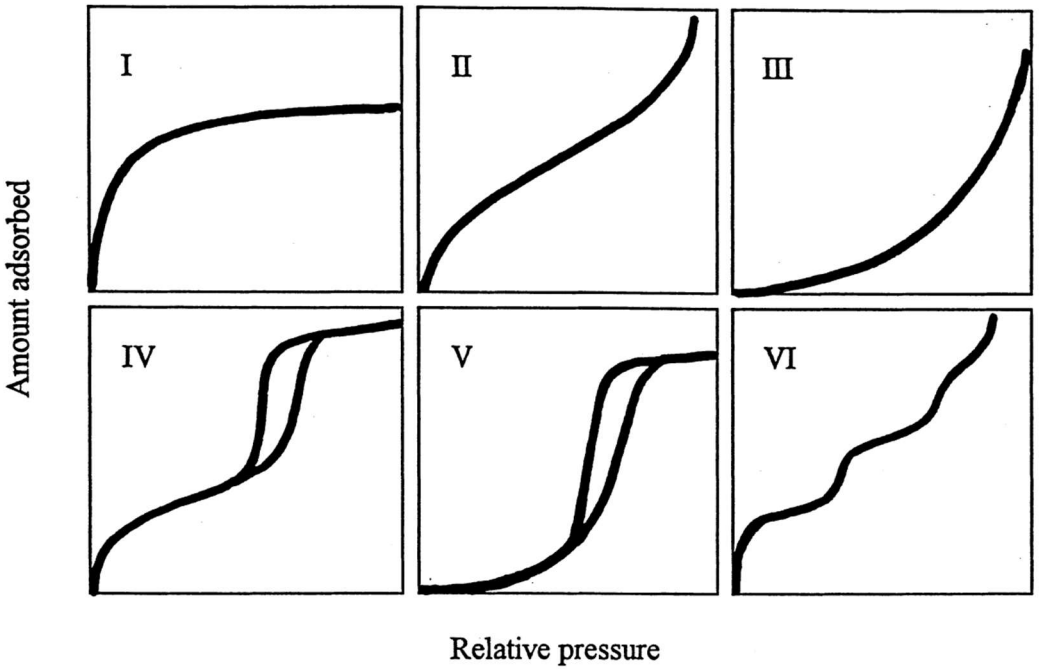

Figure 1.15: Examples of adsorption isotherms. The plateau in graph I indicates monolayering typical of microporous adsorbents. Graphs II and III present adsorption isotherms usually obtained with macroporous adsorbents. Graphs IV and V show both monolayering and multilayering along with capillary condensation, while Graph VI shows that stepwise increases in layering may occur with increasing pressure [110].

1.7 Risk Assessment and Application to Nanoparticles

A risk assessment is a methodology or process used to quantify the risk that a human faces as a result of exposure to a hazard. It is composed of four main parts carried out in the following order: hazard identification, dose-response assessment, exposure assessment, and risk characterization. The purpose of hazard identification is to classify potentially hazardous substances, determine expected exposure concentrations and scenarios, and

assess the mechanisms and extent of potential harm resulting from different frequencies and types of exposures (dermal, oral, or inhalation) to the substance. Data from in vitro and in vivo studies, as well as quantitative structure-activity relationships (QSAR) may be used at this stage. In vivo studies should evaluate absorption, distribution, metabolism, and excretion (ADME) patterns, as well as pharmacokinetics to assess biopersistence.

A dose-response assessment determines more specific relationships between doses of the substance and the corresponding severity of observed adverse effects. A 'no observable adverse effect' level (NOAEL), 'lowest observable adverse effect level' (LOAEL), or in other cases, 'benchmark doses' (BMDs) may be defined during this stage. The LOAEL and NOAEL values are obtained from dosing studies whereas BMDs are calculated through dose-response curve modeling.

Exposure assessments take into account the frequency, duration, and likely doses of the substance that populations receive, as well as which populations are more or less likely to be exposed to the substance. Dermal, oral, and inhalation pathways are evaluated, and acceptable exposure thresholds are considered by taking into account members of the population who have a decreased capacity to metabolize hazardous substances (e.g., the elderly, young children, babies, and immune-compromised individuals). Acute and chronic exposures are also evaluated as these may result in different adverse outcomes. Risk characterization evaluates all the data from the previous steps to estimate the risk of adverse health effects as a function of hazard and exposure to the substance [54], [111].

The risk assessment process was created for traditional chemicals, so there has been some debate as to whether it is suitable in its current form for application to NPs. For example, the naturally widespread existence of NPs within the ambient environment clearly distinguishes the risk assessment of ENPs from traditional chemicals [6]. Nonetheless, evaluations by several scientific and legislative bodies, including the European Food Safety Authority (EFSA) Scientific Committee [90], the Food and Agriculture Organization (FAO) and WHO [94], and the European Commission (EC) [2] have come to the conclusion that current risk assessment testing methods and models are appropriate for NPs. Nonetheless, a lack of available and/or validated NP detection, measurement and characterization methods, a scarcity of toxicity data, and the absence of formal NP-related vocabulary hinder the ability to perform a risk assessment at this time [112]. Potential red flags that a NP may be toxic include: high reactivity, complex morphology (in particular, NPs with high-aspect ratios), known interactions with biomolecules (e.g., enzymes and DNA) or metabolites (e.g., changes to or loss of coating [dynamic corona]), complex transformations (e.g., dissolution, aging effects, surface property changes, porosity), and antimicrobial properties (which could cause changes to the gut flora) [88].

1.7.1 Nanoparticle-gut Interactions

Oral exposures to NPs could potentially lead to their absorption into systemic circulation via the gastrointestinal (GI) tract. The gut epithelium consists primarily of enterocyte cells, which participate in the uptake of digested, nano-sized food particles. Smaller amounts of goblet cells produce a mucus layer (consisting of glycosylated proteins in an electrolyte solution) whose function is to prevent the passage of harmful materials through the gut epithelium. Also found within the gut wall are lymphoid nodules known as Peyer's patches. These contain M-cells which participate in the body's immune response by taking up foreign materials that pass through the mucus layer and then transporting them to nearby lymphocytes. Although M-cells only make up about 1% of the total surface area of the gut epithelium, they are relatively active in material transcytosis. Nanoparticles may be taken up either by active transport (endocytosis) via clathrin-coated pits and vesicles

in enterocytes and M-cells or by passive (paracellular) transport through intercellular spaces [113].

Nanoparticle characteristics influence absorption through the gut epithelium, however, most studies up to now have only examined the influence of one individual characteristic at a time. It is well accepted that the smaller the size of a particle, the greater the diffusion rate through the gut mucosal layer and the higher the likelihood of translocation through gut epithelial cells. In an in vivo study with rats, Szentkuti [114] found that smaller particle sizes correlated with increased diffusion rates through the gut mucosal layer: 14 nm spherical polystyrene particles were able to diffuse through the mucosal layer less than 2 minutes following luminal administration, however, the same process took 30 minutes for 415 nm particles and was not observed at all for 1.09 μm particles (transcytosis was not observed for any of the particles). Jani et al. [115] found a clear relationship between particle size and the percentage of orally administered particles translocated and detected in rat organ tissues: about 33%, 26%, 10%, 14%, and 5% of administered particles were detected for 50 nm, 100 nm, 300 nm, 500 nm and 1 μm particles, respectively, while 3 μm particles were not detected at all over a 10 day post-exposure period.

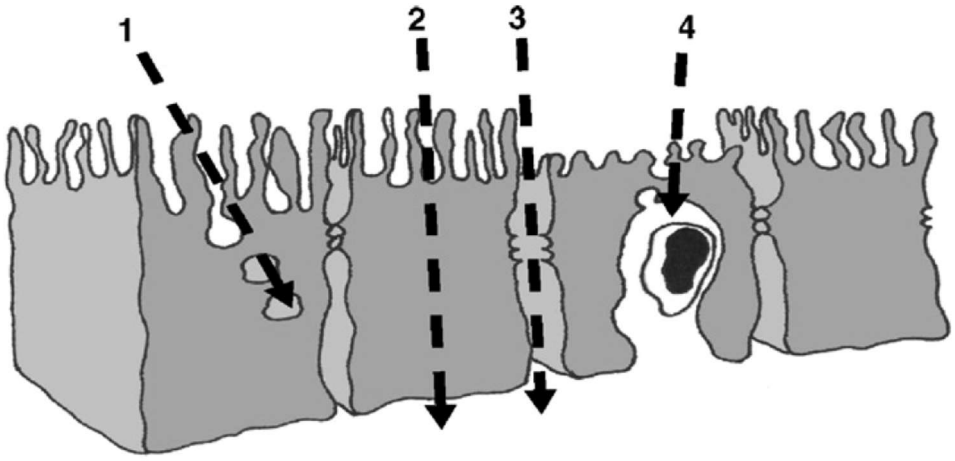

Figure 1.16: Transection of gut epithelium with possible routes for NP transcytosis via (1) enterocyte cells and (4) M-cells. Uptake may also occur by means of (2) passive diffusion or (3) paracellular transport [113].

The hydrophobicity/hydrophilicity of a NP is also important in dictating translocation through the gut epithelium, with hydrophobic NPs being taken up more frequently than hydrophilic ones. Florence et al. [116] found that after feeding rats equal amounts of poloxamer surfactant modified (hydrophilic) and unmodified (hydrophobic 60 nm polystyrene NPs for a period of 5 days, 3% of poloxamer 407 modified NPs and 1.5% of poloxamer 188 modified NPs were absorbed throughout the GI tract as compared to 10% of unmodified NPs. (Poloxamer 407 has a polyoxypropylene molecular mass of 4,000 g/mol whereas poloxamer 188 has a polyoxypropylene molecular mass of 1,800 g/mol). Despite being hydrophilic, the differences in uptake between poloxamer 407 modified NPs and poloxamer 188 modified NPs are in agreement with the fact that molecular mass is positively correlated with hydrophobicity. Hoshi et al. [117] administered doses of three different preparations of hydrophobic poly(D,L-lactic/glycolic acid) (PLGA) microspheres to chickens and found that 60 kDa and 100 kDa MW PLGA microspheres were taken up by Peyer's patches whereas 20 kDa MW PLGA microspheres were not.

Because the pre-epithelial mucus layer is negatively charged, NPs with a neutral or negative surface charge tend to be taken up more than NPs with a positive charge. Shakweh

et al. [118] found significantly larger uptake of negative and neutral PLGA NPs in mice 48 hours following ingestion relative to otherwise identical positively charged PLGA NPs. Jani et al. [119] compared the uptake between neutral polystyrene NPs and negatively charged carboxylated polystyrene NPs, finding that while both NP types were translocated through the gut epithelium, the neutral NPs were taken up to a larger extent than the negatively charged NPs.

Attempts to investigate the effects of multiple physicochemical characteristics at once on uptake through the gut epithelium have resulted in mixed findings, pointing to the need for further research and better inter-comparability between studies. For example, the use of different animal models and experimental protocols between studies has been frequently cited as a likely reason for contradictory findings. The only factor that has had consistently similar effects on NP uptake through the gut epithelium is size. Although particle size, hydrophobicity/hydrophilicity, and surface charge are very influential factors, gut physiology (i.e., the presence of excess bacteria) and the presence of specific ligands on the NP surface are also considered to disproportionately affect uptake [113].

Once a NP has been absorbed through the gut epithelium, it ends up in systemic circulation until it is either filtered into tissues or cleared by the immune system. Blood plasma is believed to contain up to 3,700 proteins, including an array of immune system components, or opsonins (e.g., immunoglobulins and complement system proteins). Contact with this complex mixture results in the instantaneous adsorption of proteins onto most particles in a process known as opsonization, leading to the formation of a 'corona.' Opsonization with immune system proteins labels foreign material for clearance by the mononuclear phagocytic system (MPS) which consists of Kupffer cells in the liver, dendritic cells in the lungs and lymph nodes, and B cells in the spleen, among others. The net result of opsonization with MPS proteins is a shortened circulation time and NP clearance in the organ containing the corresponding phagocyte (usually the liver or spleen). On the other hand, adsorption of other classes of proteins, such as dysopsonins (e.g., albumin) leads to increased circulation times. Although it is well established that the protein corona plays a major role in NP distribution, it is not entirely clear how NP physicochemical characteristics affect its formation, dynamics, and eventual influence on the particle's route through the body. It is also important to consider that as a particle moves through systemic circulation, the corona constantly changes as a function of the concentrations and binding kinetics (i.e., equilibrium constants and binding affinities) of the surrounding proteins [120], [121].

It is possible that size may be more influential than the corona in determining biodistribution. Pores in the epithelial linings of internal organs fundamentally limit passage to particles which are smaller than their diameters [122]. It has also been found that larger particles (with hydrodynamic diameters above 200 nm) experience relatively rapid clearance regardless of surface characteristics [123]. In one NP biodistribution study, an intravenous suspension containing 15, 50, 100, and 200 nm Au NPs was administered to mice, with a resulting pattern of higher particle retention in organ tissues with decreasing particle size. The liver was found to contain the highest numbers of NPs followed by the lungs, spleen, and kidneys [124]. Jani et al. [115] obtained similar results with non-ionic polystyrene NPs, finding the highest number of translocated NPs in the liver. However, these particular particles were not found in the lungs or kidneys (with the exception of 50 nm particles), indicating that size was a primary factor in the final distribution.

The relationship between particle hydrophobicity/hydrophilicity and distribution is less clear, but is nonetheless highly significant in opsonization and further distribution. Nanoparticle surfaces can be hydrophilized by the addition of long-chained polyethylene glycol (PEG) and PEG-containing copolymers onto NP surfaces. These camouflage the NPs, enabling them to resist opsonization through steric repulsion forces, leading to blood

circulation times that can last for many days. However, NPs with hydrophobic exteriors are opsonized within seconds and subsequently removed by organs of the MPS such as the liver and spleen within a matter of minutes [123]. Carrstensen et al. [125] found a positive correlation between hydrophobicity and opsonization after administering NPs with differing hydrophobicity/hydrophilicity in fetal bovine serum. Similar findings have been obtained by Müller et al. [126] and Normal et al. [127].

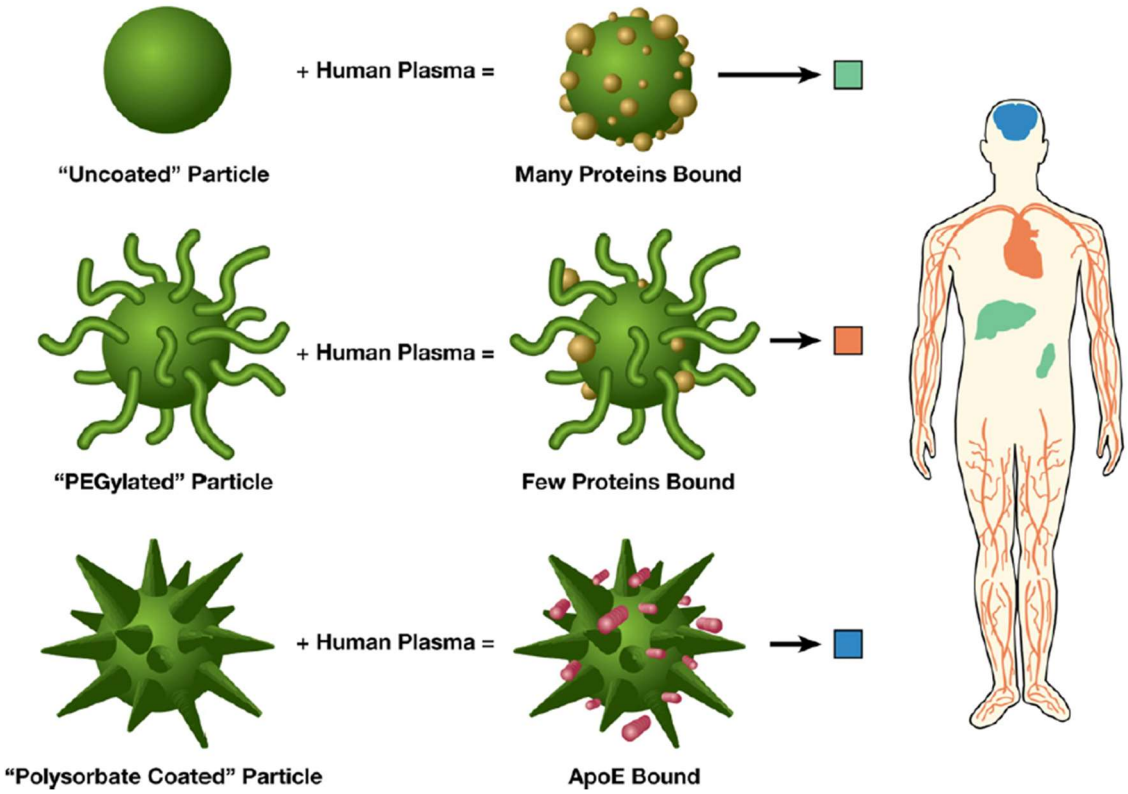

Figure 1.17: Diagram depicting in vivo NP biodistribution as a function of type and surface coating [120].

Charge is also particularly important in opsonization, since charged particles often adsorb proteins to a much greater extent than neutral particles. In one study, increased clearance by the MPS (i.e., opsonization and phagocytic uptake) was observed for NPs with higher surface charge following the introduction of biodegradable albumin NPs with neutral, positive, and negative charges into an in vitro cell culture model in the presence of complement factors. Nonetheless, when the same NPs were intravenously injected into rats, no difference was found in the clearance and accumulation rates between neutral and charged particles, indicating that other factors could more strongly affect NP distribution in vivo [128]. Qiu et al. [129] studied the in vitro cellular internalization of Au nanorods with different surface charges, finding that positively charged nanorods were opsonized the most quickly, leading to increased cellular uptake.

Once NPs have been opsonized, they are rapidly taken up by the MPS. Organs with large blood supplies, such as the liver, lungs, spleen, and kidneys, are most likely to accumulate NPs. The heart, stomach, brain, muscle, intestine, and skin are also likely candidates for NP uptake. As indicated by Sonavane et al. [124] and Jani et al. [115], the liver generally accumulates the largest fraction of NPs from systemic circulation. With regards to more specific trends in NP distribution, Owens and Peppas [123] have identified two consistent patterns from the published literature on this topic: (1) hydrophilic coatings

lead to longer NP circulation times, and (2) hydrophobic NPs accumulate in the liver and spleen whereas hydrophilic NPs accumulate more in the spleen relative to the liver. Once taken up by the MPS, NPs are exposed to a range of substances designed to metabolize biological materials (e.g., superoxides, oxyhalide molecules, nitric oxide, and hydrogen peroxide). However, since most NPs are non-biodegradable, they mostly remain sequestered in organ tissues, leading to bioaccumulation.

Despite their tendency to bioaccumulate, size-dependent and/or charge-dependent NP excretion may occur from the body via renal filtration in the kidneys or bile excretion from the liver [88]. In one study, intravenous injection of 80, 120, 200, and 360 nm mesoporous silica particles (both uncoated and with a PEG coating) into mice resulted in renal excretion, with larger NPs being excreted more rapidly than smaller NPs. Although NPs with the PEG coating generally had longer blood circulation times, decreased organ uptake, and lower excretion rates, the smallest particles (both coated and uncoated) evaded organ capture more easily than the larger ones, resulting in correspondingly lower excretion rates [130]. With regards to bile excretion, Souris et al. [131] found that while highly charged (+34.4 mV at pH 7.4) and less highly charged (-17.6 mV at pH 7.4) mesoporous silica NPs both accumulated in the liver of mice, those with a high positive charge also underwent hepatobiliary excretion into the GI tract. It was posited that higher charge not only results in increased opsonization and clearance, but also contributes to excretion.

1.7.2 Potential Mechanisms of Nanoparticle Toxicity

The main mechanisms of NP toxicity appear to be related to their large surface area to volume ratios and highly reactive surfaces [5]. These characteristics (regardless of chemical composition) may enable NPs to gain entry into cells where they may then cause ROS production, oxidative stress, mitochondrial interferences, inflammation, protein denaturation and degradation, DNA damage, endothelial dysfunction, neoantigen generation, and altered cell cycle regulation. Over extended timescales, these effects can lead to cancer, tumor formation, fibrosis, immune reactivity, neurodegenerative diseases (e.g., Alzheimer's disease and Parkinson's disease), and necrotic cell death [86], [132], [133]. High surface reactivity also means that NPs may bind contaminants, providing them access to areas they would not normally be able to enter on their own [87].

Knowledge of NP toxicity mechanisms is still in the early stages, however. In response to the idea that oxidative stress is the main mechanism of toxicity posed by NPs, Frölich et al. [86] studied the relative impact of other mechanisms as a function of particle size. In their study, 20 nm, 40 nm, and 200 nm carboxyl polystyrene latex beads were applied in varying concentrations to a cell culture (human endothelial cell line EAhy926) and a screening assay (CellTiter-Glo Luminescent Cell Viability Assay). Size-dependent cytotoxicity was observed, with only the 20 nm particles causing cellular damage. On the basis of caspase activation and lactate dehydrogenase release, it was concluded that the disturbance of membrane integrity associated with NP uptake could explain the cytotoxicity. This finding was in agreement with the observation that 20 nm particles were taken up to a much greater degree than larger particles. By contrast, oxidative stress was not found to be a significant mechanism of toxicity to cells, and no significant difference was found between 20 nm and 200 nm particles in the generation of oxidative stress. It was concluded that apoptotic and necrotic cell death and decreased proliferation are significant toxicity mechanisms and that therefore more time should be devoted to studying the signaling cascades involved in these processes.

Nanoparticles may also be more or less toxic or exhibit different types of toxicity depending on their location in the human body. For example, NPs which bypass the blood-brain barrier

may cause excessive damage because the high oxidative metabolism of the neurological system makes it especially vulnerable to the harmful effects of ROS production and metallic NP accumulation [134]. However in the bloodstream, NPs may cause hemolysis (leads to hemolytic anemia), complement activation, and thromboemboli formation. Proteins which opsonize onto the NP surface in the bloodstream dictate the likelihood of these adverse outcomes (e.g., fibrinogen can lead to an inflammatory response) [135].

1.8 Plant Exposure to Nanoparticles

Given the substantial quantities and widespread existence of NPs in the ambient environment, plant exposure is inevitable. Of greatest concern are exposures to: 1) nanoformulated pesticides and herbicides which are designed to be stable over long periods of time and which may be composed of elements not normally present in the environment [8], and 2) inadvertent pollutant NPs from anthropogenic sources (as discussed in Subsection 1.1.2), which may also include the application of NP-containing sewage sludges as crop fertilizers [90], [136]. Understanding how plants respond to NPs is an essential part of assessing the potential for NP bioaccumulation, transformation, and food chain transfer, and ultimately, their risk to food safety, human health, and ecosystem quality [137].

1.8.1 Plant Exposure to Atmospheric Deposits and Foliar Adhesion

Atmospheric deposition can be a major contributor to the pollutant load of plants, particularly in urban and industrial areas [138]–[140]. As already explained in Paragraph 1.1.2.1.3, deposition may occur through gravitational sedimentation, diffusion from Brownian motion, and from impaction and interception associated with air turbulence [20], [22], [23]. Nanoparticles are of particular relevance in this context because anthropogenic metal(loid) particle emissions are disproportionately concentrated in the finest particle size fractions [141]–[144], which can also be quickly transported over great distances through the atmosphere [14].

A handful of studies have demonstrated the impact of atmospheric deposition on above-ground plant contamination. Schreck et al [145] detected harmfully elevated concentrations of Pb in the leaves of lettuce (Lactuca sativa L.), parsley (Petroselinum crispum), and ryegrass (Lolium perenne L.) plants after one month growth in the yard of a secondary lead smelter. Already after 2 weeks of growth, concentrations of Pb were about 17 times higher than the maximum safety threshold level (6 mg Pb/kg dry weight [DW]) set by EC Regulation No. 221/2002 for leafy vegetables and fresh herbs. In a related study to compare the influence of soil and air pollution on leaf Pb concentrations, the leaves of lettuce and ryegrass plants contained eight and five times higher Pb concentrations, respectively, when exposed to atmospheric deposition in the courtyard of a secondary lead smelter in comparison to root exposure in Pb-contaminated soil (2,000 mg/kg dried soil; six week exposure period) [146]. Al Jassir et al. [147] traced elevated concentrations of Pb, Cd, Cu, and Zn in roadside market vegetables in Riyadh City, Saudi Arabia to the atmospheric deposition of nearby automobile and industrial emissions. In another study, Pb isotope ratio analysis indicated that approximately 70% of the Pb detected in the leaves of Aster subulatus plants in Nanjing, China originated from atmospheric deposition rather than from native Pb present in the soil [148].

Foliar characteristics have been observed to affect particle adhesion. Xiong et al. [149] speculated that decreased retention of metal(loid) PM by cabbage leaves in comparison to spinach leaves was due to a thicker surface wax layer. In an outdoor study to evaluate the

impacts of air pollution from an iron pelletization factory on three Brazilian plants: B. sericea, C. verbenacea, and P. guineense, Da Silva et al. [150] found that the highly wrinkled and less waxy leaves of C. verbenacea contained significantly more PM than the smooth and waxier leaves of B. sericea. In addition, increased amounts of deposited Fe particles were observed at trichome (i.e., plant hair) insertion points on the leaf surfaces of the three test plants following histochemical preparation and optical microscopy analysis. Using SEM, Song et al. [151] also observed that airborne particles preferentially deposited onto and near stomata (i.e., aqueous pores which participate in gas exchange), wrinkled areas, and trichomes on the leaf surfaces of five evergreen tree species.

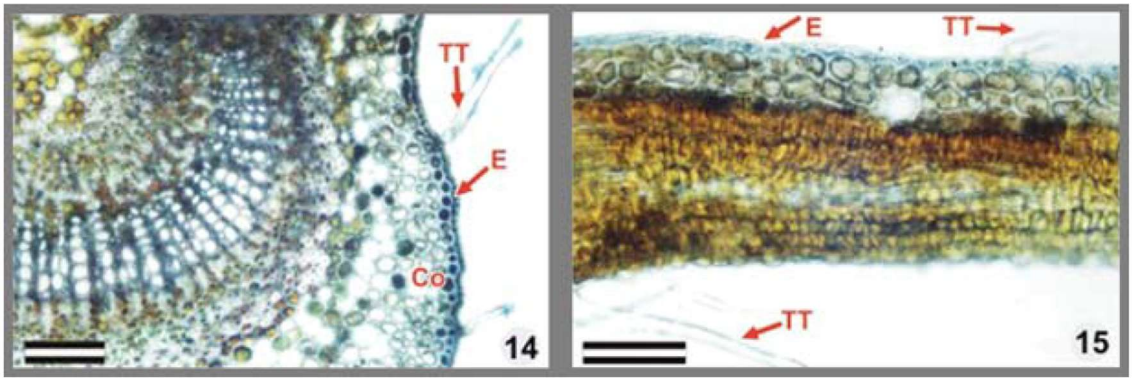

Figure 1.18: Optical micrographs of P. guineense leaf cross sections showing Fe particles at the bases of glandular and tector trichomes (GT and TT, respectively). E = epidermis. Scale bars = 50 μm [152].

Although leaf characteristics play a role in particle adhesion and retention, the influence of surface free energy (SFE), a quantitative measure of polar and dispersive forces which determine hydrophobicity/hydrophilicity (i.e., wettability), has not been investigated in the context of foliar NP exposure. Foliar SFE is dictated by the degree of surface roughness (i.e., wrinkling and presence of nano- and microstructures, which are positively correlated with hydrophobicity) and the chemical and structural composition of the cuticle covering the foliar surface (consisting mostly of cutin, with lower amounts of waxes, phenolics, and polysaccharides). The surface tension of a liquid droplet in combination with the foliar SFE determines the strength of adhesion (i.e., the contact area), which in turn also affects internalization [153], [154], since a higher contact area can be expected to result in greater internalization. Because SFE is partly determined by surface roughness, it is relevant to consider that it may be modified by particle deposition [155], hence potentially changing plant susceptibility to particle adsorption and retention with successive particle exposures.

1.9 Nanoparticle Uptake Mechanisms and Translocation in Plants

1.9.1 Roots

Nanoparticle internalization by roots is best understood through a basic knowledge of anatomical root structure. In the mature root, the outermost to innermost cell layers include the cuticle and epidermis, cortex, endodermis with Casparian strip, and the vascular cylinder containing the xylem and phloem. Compared to the leaf cuticle, the root cuticle is thinner to allow for water absorption. In mature root segments, elongated

epidermal cells form numerous root hairs which vastly increase surface area, further enhancing water and nutrient absorption. The cortex consists of multi-layered parenchyma cells, whose primary function is to store food. The endodermis is composed of a single layer of tightly bound cells whose walls contain suberin (i.e., Casparian strip), a waxy, hydrophobic material. Prior to reaching the endodermis, water and absorbed materials may follow either an apoplastic pathway, in which transport occurs between the cell wall and plasma membrane, or a symplasmic pathway, in which transport occurs intracellularly through interconnecting plasmodesmata. The presence of the Casparian strip prevents apoplastic movement, necessitating passage through the plasma membrane into the cell to access the vascular bundle. Inside the vascular bundle, the xylem transports water and solutes from roots to leaves, while the phloem transports the metabolites of photosynthesis from leaves to roots [156].

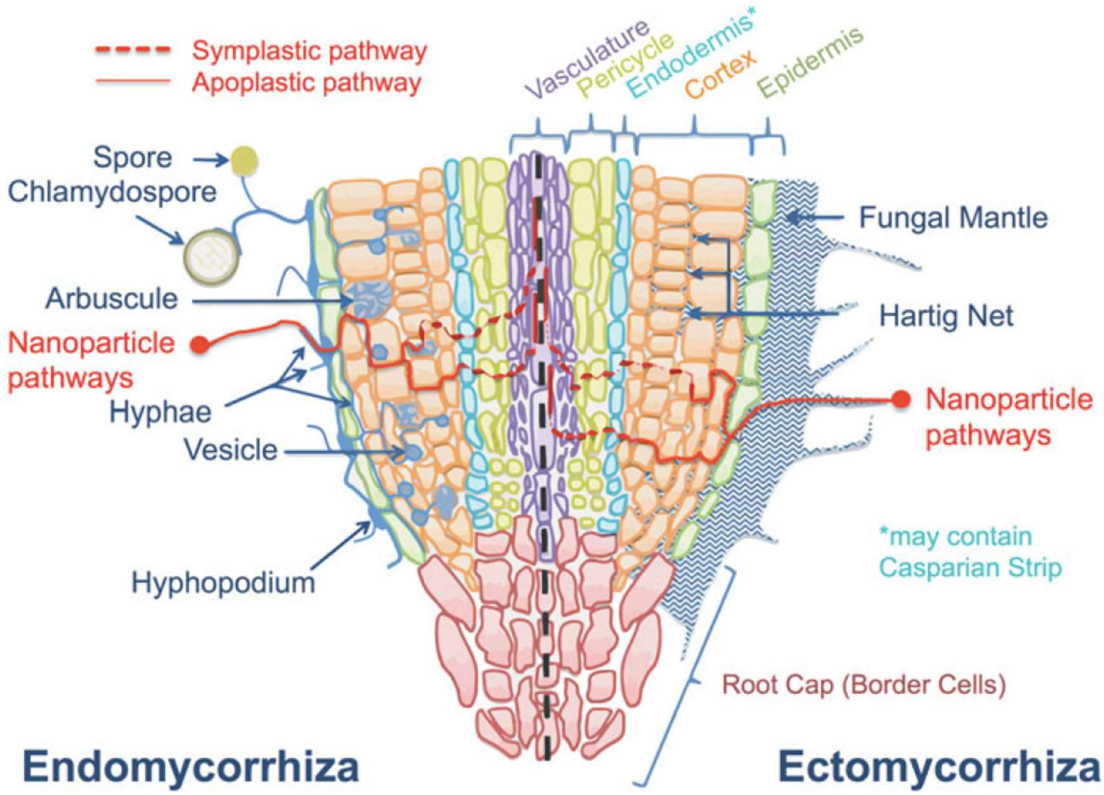

Figure 1.19: Possible NP pathways into roots in the presence of endomycorrhizal fungi or ectomycorrhizal fungi [136].

Plant transpiration (i.e., the movement of water from roots to leaves driven by evaporation from leaves) provides the driving force for NP transport [157], [158]. Zhai et al. [159] confirmed the use of this pathway in NP root to leaf translocation after detecting Au NPs (15, 25, and 50 nm) with TEM in the leaves and plasmodesmata of cells surrounding the xylem and phloem following root exposure of poplar plants (Populus deltoids × nigra, DN-34). Sabo-Attwood et al. [160] detected an identical NP biodistribution and pattern of uptake with TEM and X-ray absorption near-edge microspectroscopy after root-exposing tobacco plants (Nicotiana xanthi) to Au NPs (negatively charged, 3.5 nm and 18 nm).

Unlike with leaves where no barrier to atmospheric deposits is present, roots are surrounded by a complex mixture of materials which significantly affect NP internalization. Nearly all plant species exist in symbiotic relationships with MOs (e.g., N-fixing rhizobia

bacteria and Pseudomonas chlororaphis O6) and mycorrhizal fungi, which vastly increase the root surface area while also enhancing and regulating nutrient and mineral uptake. Ectomycorrhizal fungi form a thick mantle of mycelium (i.e., bundles of individual filaments called hyphae) around roots, with segments that extend between cells of the cortex. Endomycorrhizal fungi form a less dense network of mycelium, however individual hyphae grow into the root, both between and within cells of the cortex [161]. After root-exposing clover plants (Trifolium repens) with endomycorrhizal fungi to either Ag NPs or FeO NPs, Feng et al. [162] found metal-specific responses, with Ag NPs exhibiting greater toxicity at decreasing doses, and FeO NPs exhibiting greater toxicity at increasing doses. It was surmised that the fungi was unable to reduce the toxicity of Ag exposure below a threshold exposure concentration and that at higher concentrations, increased Ag NP agglomeration reduced dissolution and bioavailability. For the FeO NP exposure, it was concluded that excess Fe inhibited the production of glomalin by the fungi, resulting in decreased plant growth. It is interesting to note that mycorrhizal fungi may also reduce metal toxicity by inducing the formation of NPs from dissolved metals as Manceau et al. [163] found after exposing Phragmites australis and Iris pseudoacorus plants with endomycorrhizal fungi to Cu-contaminated soil.

Roots also excrete mucilage and exudates (M/E) which acidify the rhizosphere (i.e., the soil immediately surrounding and affected by the roots), enhancing the bioavailability and uptake of soil nutrients [136]. With NP exposure, M/E may reduce uptake through both dissolution [164]–[167] and interception [136], [168], [169]. These responses are likely to be element- and plant-specific, as Lin and Xing [158], for example, did not find enhanced dissolution of ZnO NPs following root exposure to ryegrass plants. Since the rhizosphere is acidified by M/E, surface charge logically has an effect on NP uptake by roots, with negatively charged NPs tending to be internalized at higher rates into plant tissues in comparison to positively charged NPs [170], [171]. The rhizosphere may also change NP zeta potential, resulting in larger particle sizes due to increased agglomeration, thereby decreasing internalization [158].

Despite the existence of intricate mycorrhizal fungi networks and M/E, size appears to be the main determinant of NP uptake, with smaller NPs consistently being internalized at much greater rates than larger NPs, all other factors aside. This is in line with the frequent observation that the pores of the root cuticle and epidermis act as a sieve or filter, blocking access to NPs above threshold sizes [136], [159], [160], [169], [172]. Sabo-Attwood et al. [160], for example, found internalized 3.5 nm Au NPs in tobacco plant tissue with TEM, but was unable to find 18 nm Au NPs.

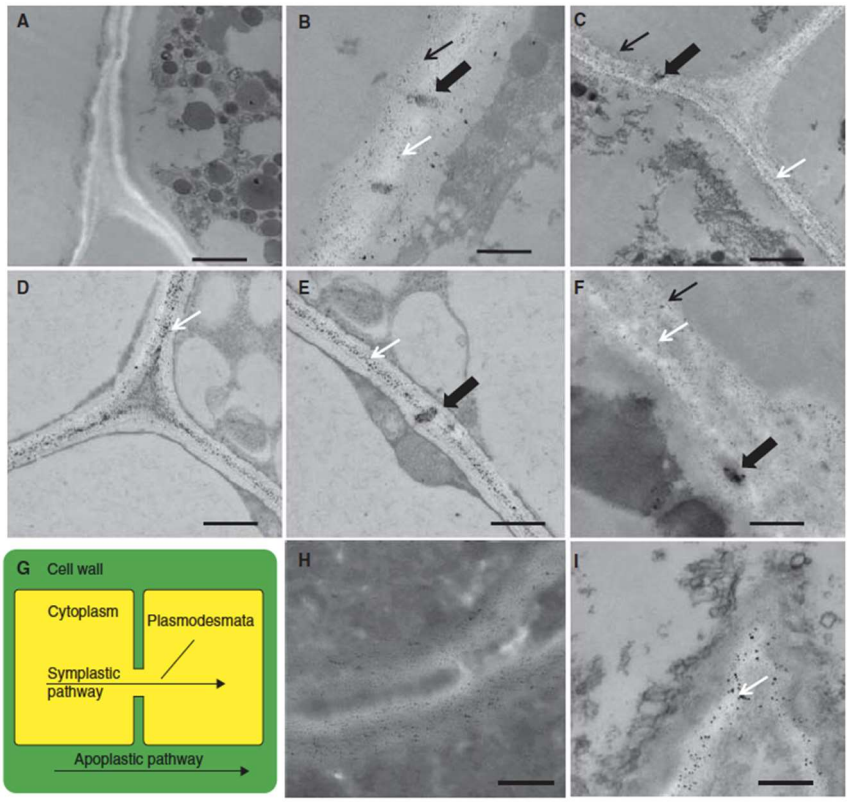

Figure 1.20: TEM micrographs of Ag NPs in Arabidopsis thaliana root tissue and diagram of cellular transport routes. No Ag NPs can be seen in the control root (A) or following exposure to Ag^+ ions (H), whereas Ag NPs (20 nm) can be seen on the cell wall (B, C) and in the middle lamella (D, E; a pectin layer between adjacent cell walls). Larger Ag NPs 40 nm (F) and 80 nm (I) in size can also be seen in the cell wall. Thick black arrows indicate the location of plasmodesmata, thin black arrows point to Ag NPs in the cell wall but not in the middle lamella, and thin white arrows point to Ag NPs in the middle lamella. A diagram shows the pathway followed during apoplastic transport and symplasmic transport (G). Scale bars = 1 μm (A, C, D, E) and 350 nm (B, D, F, H, I) [169].

1.9.2 Leaves

Plant leaves are constantly exchanging gases, nutrients, and contaminants with the environment, however their interactions with NPs have been less well studied relative to root exposures. The available evidence indicates that NP penetration and uptake is variable, showing dependence on weather conditions (e.g., humidity), plant species, element speciation, and overall plant condition, as well as the size, type, chemical composition, and stability of the NPs which deposit onto the plant surface [173], [174].

A typical leaf contains three primary components: the epidermis, mesophyll, and veins, or vascular bundle. The epidermis is the outer-most single-celled layer of the leaf, responsible for producing the overlying cuticle. The mesophyll is comprised of specialized chloroplast-containing cells responsible for converting the sun's light energy into biochemical energy that can be used by the plant. The veins, or vascular bundle, are comprised of the xylem and phloem which transport water and nutrients throughout the plant [156]. Therefore in order for NPs to be translocated from leaves to roots, NPs must bypass the cuticle, epidermis, and mesophyll in order to reach the phloem, which transports

carbohydrates throughout the plant. It is also a possibility that NPs may enter and accumulate in cells, resulting in potentially toxic effects.

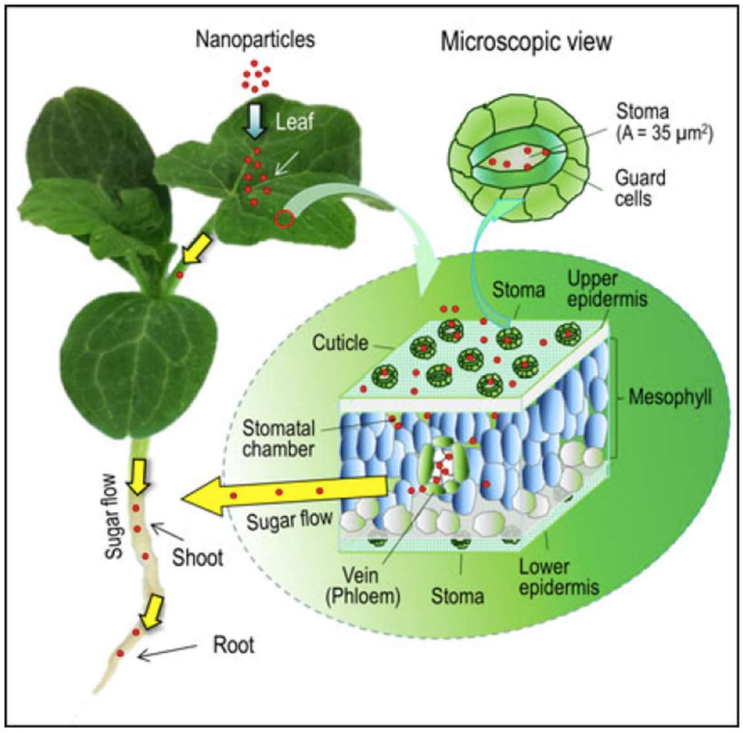

Figure 1.21: Leaf structure and NP uptake and leaf to root translocation pathways [175].

Passage through the plant cuticle can occur through lipophilic and hydrophilic pathways. The lipophilic pathway consists of translocation through the waxy cuticle whereas the hydrophilic pathway involves passage into the leaf through the bases of trichomes, stomata, and other plant openings where a cuticle covering is absent, such as hydathodes (i.e., specialized pores which exude excess water) [12], [176], [177]. In studies where foliar surfaces were examined following exposure to PM or NPs, particle entrapment in the lipophilic cuticle has been observed with electron microscopy [145], [146], [149], [178]–[180], with evidence of diffusion where depth analysis with ToF-SIMS was performed [145], [178], [180]. Using foliar cross-section analysis with TEM, Larue et al. [178] observed that pristine anatase TiO_2 NPs (4 nm) damaged the surface cuticle and underlying cell walls of lettuce (Lactuca sativa) leaves, which was speculated to be the result of their photocatalytic properties.

More evidence is available to support the use of the hydrophilic pathway, with stomata considered the most likely route of entry due to their large size (10 nm – 1 μm) and high transport velocity [173]. Using SEM-EDX, NP aggregates near and/or within stomatal openings on leaf surfaces have been observed following exposure [145], [146], [149], [178], [180]. Using TEM, Wang et al. [175] and Hong et al. [181] observed NPs in the vascular system of watermelon (Citrullus lanatus) and cucumber (Cucumis sativus) plants, respectively, suggesting that internalization occurred through stomata. Size has been noted to play a major role in uptake. Following foliar exposure of cabbage (Brassica oleracea) and spinach (Spinacia oleracea) plants to PM, Xiong et al. [149] found that particles below 1 μm were not detected in stomata nearly as frequently as particles below 0.1 μm during analysis with environmental SEM-EDX. Eichert et al. [176] also observed the stomatal uptake of 43 nm sized fluorescent polystyrene particles by the leaves of broad bean (V. faba

cv. Condor) plants using confocal scanning laser microscopy, but not of 1.1 µm particles. Internalization of NPs by stomata may be strongly modified by external factors. Burkhardt et al. [177] found that foliar uptake may be significantly enhanced by the presence of fungal hyphae, bacteria, and hygroscopic particles in stomatal chambers, which reduce hydrophobicity and promote the formation of microscopic liquid films connecting the inner and outer portions of plant leaves.

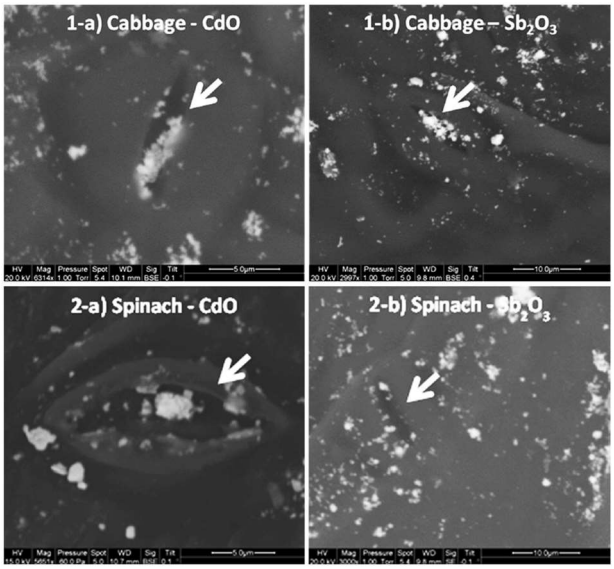

Figure 1.22: SEM micrographs showing NPs in and around stomata [149].

Although NP uptake into plants is normally a highly selective process, any physical injury to the plant compromises protective boundaries, leaving interior cells vulnerable to NP infiltration [136], [182]. Nonetheless, a study by Al-Salim et al. [168] showed very low uptake of CdSe/ZnS quantum dots (QDs) coated with either glycine, cysteine, or mercaptosuccinic acid (average 6.5 nm) by the cut stalks of chrysanthemum (Chrysanthemum sp.), ryegrass (Lolium perenne 'Maverick G2'), and onion (Allium cepa). Similar findings were obtained by Lü et al. [183] after exposing the cut stalks of rose (cv. Movie Star) flowers to Ag NPs (2-5 nm). These results are consistent with the fact that plants possess mechanisms to quickly respond to wounding, by, for example, blocking plasmodesmata around wounded and infected areas with callose, a cell wall polymer, and other materials to promote healing and prevent the spread of harmful substances [184].

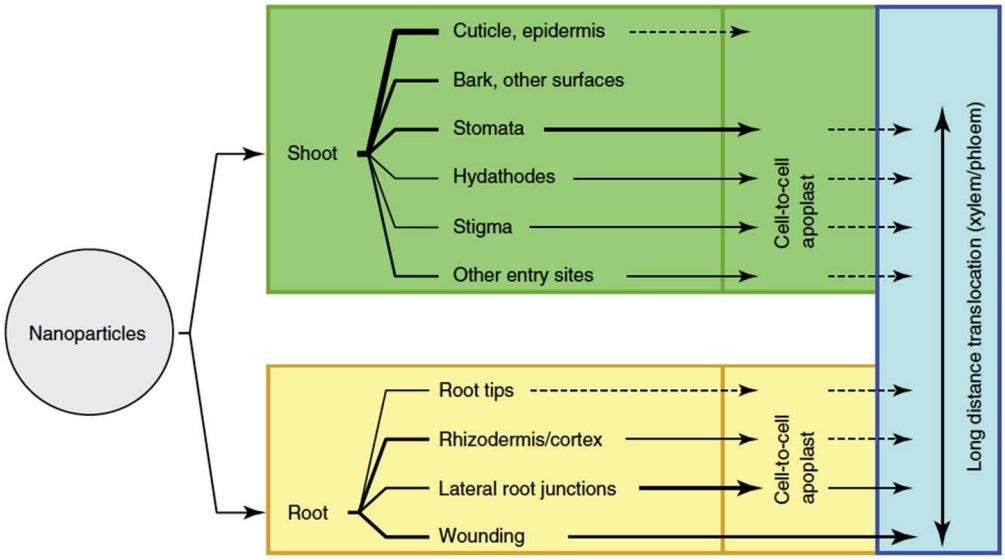

Figure 1.23: Possible internalization and translocation pathways in plants. Line thickness is associated with the presumed significance of the pathway while dashed lines signify very low likelihood of the pathway being used [182].

1.9.3 Cellular Uptake

Once NPs bypass the cuticle, cellular access is limited by the cell wall and plasma membrane. The cell wall is a firm semipermeable layer consisting mainly of cellulose (carbohydrates and proteins). Although the cell wall was for many years believed to contain pores of 3.5-5.2 nm, recent findings have shown that they can be very flexible, expanding enough to allow particles as large as 50 nm to pass through [136]. It has also been proposed that NPs, through their high reactivity, may interact with cell walls in ways that result in pore damage and enlargement [139], [145].

If NPs are able to pass through the cell wall, the plasma membrane, or bilayer lipid membrane, forms one last barrier to cellular access. Several paths are available for NPs to pass through the plasma membrane, including via endocytotic processes, or through embedded transport carrier proteins or ion channels. Available evidence suggests that endocytotic pathways (responsible for cellular nutrient cycling) are likely to be the main point of NP entry. Endocytotic entry can further consist of clathrin-dependent endocytosis or clathrin-independent endocytosis. In clathrin-dependent endocytosis, invaginations in the clathrin layer of the cellular membrane lead to vesicle budding into the cell. Less is known about clathrin-independent endocytosis, however three different pathways have been identified: caveolae- and lipid-raft-mediated (involves vesicle formation through invaginations, or 'caveolae' which are involved in signal transduction and cellular uptake), fluid-phase endocytosis, and phagocytosis [139].

Once NPs gain access to a cell, they may bind with cellular components such as the endoplasmic reticulum, Golgi, or endo-lysosomal system and lead to ROS production through interference with metabolic processes [12]. Currently, little is known about the specific interactions that may occur between NPs and various cellular components or where NPs are likely to congregate within a cell [185].

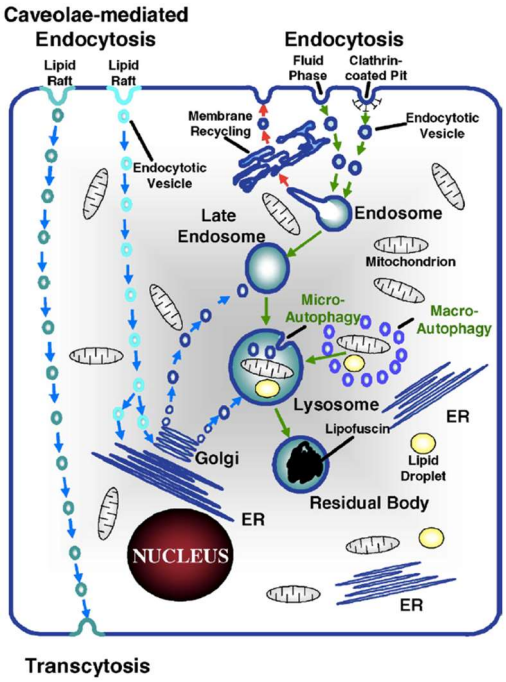

Figure 1.24: Diagram of NP uptake pathways into cells [186].

Chapter

Aim of the Work

The aim of this dissertation is to illustrate how the behavior of NPs in air and atmospheric deposition of NPs might inadvertently affect food and edible plant exposure to NPs, and how edible plants could be expected to respond to them. Specifically, we are investigating two pathways of food exposure to NPs: 1) indoor air pollution from burning incense and the following dynamics and decay mechanisms of the emitted NPs from air in an unventilated room setting and 2) the exposure of arugula (low surface free energy; SFE) and escarole (high SFE) to Pt NPs, which are emitted from catalytic converters from trafficked roadways, and their adhesion, internalization, and translocation to roots. These results have implications for food safety, human health, and the use of nanotechnologies in agriculture (i.e., nanopesticide application) and engine technologies, making them relevant to risk assessment efforts.

The hypotheses of this work are as follows:

- Indoor emissions produced by incense burning remain airborne for a considerable amount of time (i.e., hours) under conditions of low ventilation due to the dominant presence of accumulation mode particles (100-1,000 nm in size), which have inefficient removal mechanisms,
- Particle number concentrations decrease with increasing distance from the incense source due to coagulation between nucleation mode particles (up to 100 nm),
- High foliar SFE is associated with increased adhesion of Pt NPs,
- Higher foliar SFE is associated with increased internalization and translocation of Pt NPs to roots due to a higher contact area between droplets of applied Pt NP dispersion and the leaf surface relative to droplets of Pt NP dispersion on leaves with low SFE,
- A higher fraction of Pt NPs are internalized and translocated from roots to leaves than from leaves to roots due to the role of roots in regulating metal and nutrient uptake from soil, in addition to a higher surface area and larger size exclusion limits of roots in comparison to leaves [136], and
- Foliar SFE changes in response to Pt NP exposure due to alterations in micro- and nano-surface roughness.

Therefore the goals of this work were to:

- Examine particle dynamics and decay mechanisms from air before, during, and following incense burning in an unventilated indoor room setting in terms of NP size distributions and concentrations and size-based mass distribution,
- Determine the relationship between particle number distributions and concentrations during incense burning as a function of distance from the incense emission source,

- Determine the effect of foliar SFE on Pt NP adhesion, uptake, and translocation from leaves to roots using arugula (low SFE) and escarole (high SFE) plants,
- Quantify and compare the internalization and translocation of Pt NPs following root exposure and foliar exposure (i.e., the fraction of Pt in leaves following root exposure and the fraction of Pt in roots following foliar exposure),
- Quantify and determine the effect of foliar Pt NP exposure on SFE.

Chapter

Materials and Methods

3.1 Incense

3.1.1 Incense Burning Protocol

Incense burning measurements were performed using incense sticks of two different incense types: African Violet and Strawberry (Hem Corporation, www.hemincense.com). These two incenses were selected as they were the most common ones on the market and from the same manufacturer, in order to assure repeatability of the experiments. Measurements were carried out at varying distances from the measurement inlet (15 cm, 100 cm, and 300 cm). For each distance, three measurements were performed (with nine measurements in total for each incense). Hence, particle number distributions and concentrations as a function of distance from the incense source could be determined. All measurements were completed in an empty room 2.7 m in length, 3.8 m in width, and 3.1 m in height (volume of 31.8 m^3). As seen in Fig. 3.1, the room has one door and one wall of windows, as might be observed in a typical room of a residential dwelling (i.e., bedroom, office, or living room). The door and windows were closed during measurement. In addition, the room was completely empty during measurements, with no additional elements that could act as impact surfaces for the particles. The air exchange rate was not measured, however, there was no detectable draft in the room as the windows were newly installed and the conditions for all the measurements were roughly the same. The temperatures and humidity for each measurement were recorded and are presented in Table 3.1.

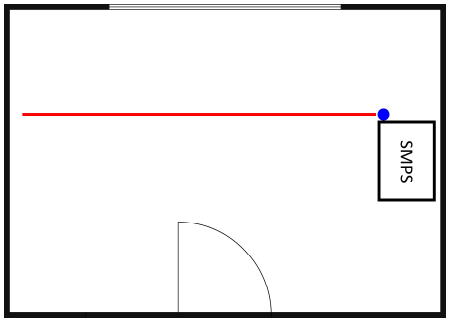

Figure 3.1: Schematic diagram of the incense burning testing room. The grey line at the top represents the windows while the bottom middle portion represents the location of the door. The incense was moved along the red line and the particles were collected at the inlet of the SMPS, represented as a blue circle.

After measuring the background particle concentrations, a gas lighter was used to light each incense stick. It was shown that this combustion source does not noticeably influence subsequent particle measurement readings. Each incense stick was allowed to burn to completion, followed by an additional measurement of the background particle concentrations to monitor the particle concentration decrease. After completion of the experiment, the room was vented overnight, and the background levels tested before starting a new measurement. The shortest and the longest burning times were 39 and 58 minutes, respectively.

Table 3.1: Humidity and temperature at the beginning of each measurement. S and AV stand for Strawberry and African Violet incense, respectively. The number next to the incense abbreviation indicates the distance of the incense from the measurement inlet while the number following the hyphen indicates the repetition (from 1 to 3). Therefore, e.g., S15-1 denotes the first measurement of the Strawberry incense placed 15 cm from the inlet.

Measurement	Humidity (%)	Temperature (°C)
S15-1	30	24
S15-2	40	25
S15-3	28	24
S100-1	28	24
S100-2	22	21
S100-3	32	18
S300-1	32	24
S300-2	23	24
S300-3	30	24
AV15-1	34	22
AV15-2	50	22
AV15-3	41	20
AV100-1	23	23
AV100-2	24	25
AV100-3	30	24
AV300-1	32	23
AV300-2	24	24
AV300-3	19	24

3.1.2 Chemical Analysis of Unburned and Burned Incense

The amounts of C, H, and N were determined by elemental analysis using an Elementar vario EL cube elemental analyzer. The samples for the chemical analysis were decomposed using the alkali fusion method. The amounts of Al and Fe were determined by ICP-MS, Ca was quantified by complexometric titration, and Si was quantified spectrophotometrically.

X-ray diffraction was performed using a D4 Endeavor diffractometer (Bruker AXS) at room temperature. A quartz monochromator Cu Ka1 radiation source ($\lambda = 0.1541$ nm) and a Sol-X energy dispersive detector were used. The angular range (2θ) was chosen from 5° to 75° with a step size of 0.02° and collection time of 4 seconds. The unburned (pure)

incense was prepared by removing the contents with a knife, while for the burned incense, the remaining ash from burning was collected and measured.

For analysis with SEM-EDX, burned and unburned incense samples were applied to double-sided carbon tape and sputter coated with ~10 nm Au using an SCD 005 cool sputter coater (BAL-TEC GmbH, Switzerland).

3.1.3 Nanoparticle Distributions and Concentrations

Nanoparticle distributions and concentrations in burning incense emissions were measured with the use of a TSI SMPS 3638L85 equipped with an attachable desiccator, SoftXray neutralizer, long DMA, and a Model 3785 WCPC. This model measures the particle size distribution from 15 to 700 nm based on electrical mobility. The DMA first separates the NPs with respect to size while the WCPC counts them. The measurements were performed as successive 3 minute scans.

Additional information on the mass distribution and content of the emitted incense particles in air was obtained with the use of a DLPI. The DLPI collects the particles using 13 diameter-selected filters from 30 nm up to 10 µm. This way, by knowing the initial mass of the filters, the mass of the emitted particles can be obtained in a size-selected manner. The DLPI was operated alongside the TSI SMPS for a period of 4 to 10 hours. The same setup was previously used for measuring the NP size distribution emitted from sparklers [187].

3.2 Pt Nanoparticles

Pt nanopowder (<50 nm) was purchased from Sigma-Aldrich. Platinum was selected because of its low environmental abundance (2.7 ppb) [188], resistance to dissolution, and direct connection to anthropogenic activity (especially through catalytic converters [189]. Morphology and chemical composition were analyzed using SEM (Jeol JSM-7600F, Japan) coupled to EDX (INCA Wave, 500, Oxford Instruments Analytical, Ltd., UK) and TEM (Jeol JEM-2010F, Japan). The average particle size and size distribution were obtained from a random sample of 300 particles from TEM images using ImageJ v. 1.50i software. Specific surface area was determined with the BET method using single point nitrogen adsorption with a FlowSorb II 2300 instrument (Micromeritics, USA). In accordance with recommendations by Taurozzi et al. [190], 10 mL of a 500 mg Pt NPs/L dispersion were prepared by pulse probe sonication (10 s pulse, 5 s rest) in a 2.5 cm diameter glass vial on ice for 3 min at 8.58 W. From this dispersion, a 50 mg Pt NPs/L dispersion was analyzed with DLS for the hydrodynamic size and zeta potential using a ZetaPALS instrument (Brookhaven Instruments Corporation, USA) using a red laser (λ = 658 nm) for illumination with a scattering angle of 90°.

Two methods were used to examine Pt NP dissolution in ultrapure water at the experimental concentrations (5, 50, and 500 mg Pt NPs/L): 1) ultrafiltration for 30 min at 1800 × g and 20°C using Amicon Ultra-4 centrifugal filter units composed of regenerated cellulose (nominal molecular weight limit of 3 kDA), and 2) ultracentrifugation for 30 min at 100,000 × g and 20°C (Beckman Coulter L8-70 M class H preparative ultracentrifuge; fixed-angle 70 Ti rotor; 15 mL Beckman Coulter Quick-Seal Polyallomer Centrifuge Tubes, USA). The supernatant from both methods was acidified to 5% HNO_3 (Suprapur 65% HNO_3, Merck, Germany), however samples from ultracentrifugation were carefully removed with a pipette and filtered (0.45 µm, hydrophilic PVDF, Millipore Millex-HV, Germany) before this step. In addition, samples of 5, 50, and 500 mg Pt NPs/L dispersions were dissolved in a 1:1 ratio of dispersion to aqua regia (25%: Suprapur 65% HNO_3, Merck,

Germany; 75%: puriss. p.a. 37% HCl, Merck, Germany) to assess the actual amount of Pt in the experimental dispersions. These samples were diluted to 5% HNO_3 (Suprapur 65% HNO_3, Merck, Germany) prior to analysis.

To examine the possibility that Pt NP dissolution was affected by application onto the foliar surfaces, arugula and escarole leaf samples exposed to the 500 mg Pt NPs/L dispersion (as described in Subsection 3.3.1) were submerged in ultrapure water (final nominal concentration of 5 mg Pt NPs/L) and homogenized using a T10 basic ULTRA-TURRAX homogenizer (IKA®-Werke GmbH & Co. KG, Germany), as shown in Fig. 3.2. The blended mixture was then treated by ultrafiltration and ultracentrifugation in the same manner as the bare dispersions. All samples were prepared in triplicate with at least one blank and analyzed for Pt content using ICP-MS (7500 series, Agilent Technologies, Inc., USA) as described in Subsection 3.3.4.

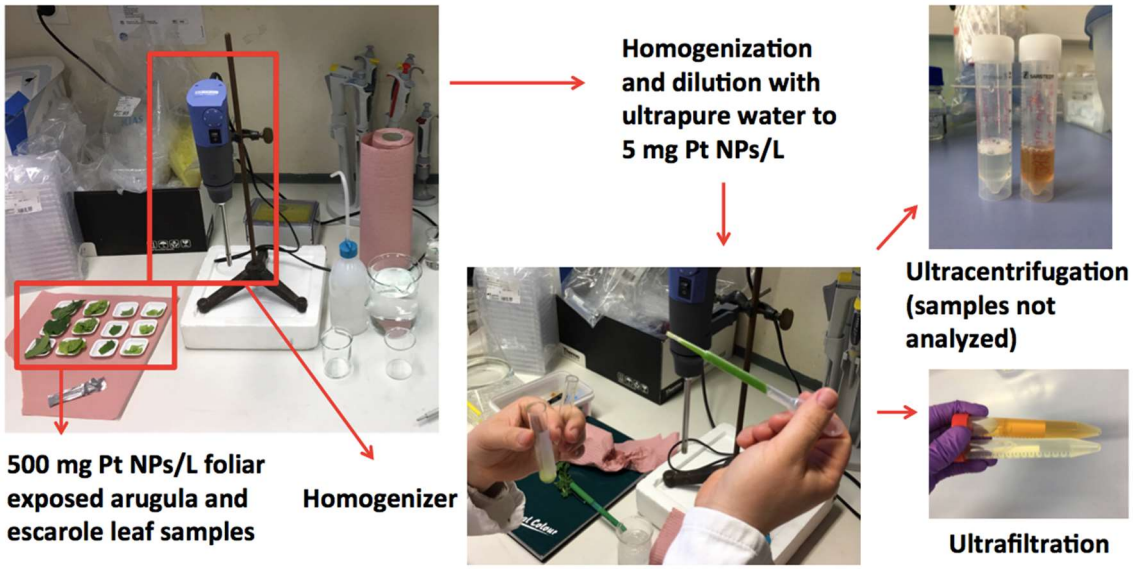

Figure 3.2: Preparation of foliar exposed arugula and escarole leaf samples (500 mg Pt NPs/L) for Pt NP dissolution analysis using ultracentrifugation and ultrafiltration. The clear and colored supernatant originate from arugula and escarole, respectively.

3.3 Arugula and Escarole Plants

3.3.1 Cultivation and Exposure to Pt Nanoparticles Through Leaves and Roots

Arugula and escarole were grown according to a modified version of OECD test no. 208 (terrestrial plant test: seedling emergence and seedling growth test) using plastic pots (diameter: 11 cm; height: 10 cm) filled with biological 100% finely milled peat (pH: 6.5; Bio Plantella START special soil for sowing and potting, Unichem LLC, Armenia). Ten seeds were placed into each pot, followed by the removal of nine seedlings upon germination. Three replicates containing five plants each were cultivated for every exposure (15 plants in total). The soil pH was evaluated before planting and after the experimental period for control and Pt NP exposed plants using ISO 10390: soil quality – determination of pH. All plants were raised in growth chambers (day/night period: 16h/8h; temperature: 21°C/17°C; humidity: 45%/65%) with a photosynthetic photon flux density of 110 µmol

m^{-2} s^{-1}. Plants were watered with tap water using a self-watering device to ensure constant and even hydration. An image of the plant cultivation setup is shown in Fig. 3.3a.

Figure 3.3: Representative plant photographs of the cultivation and exposure setup on the day of planting (a) along with photographs of arugula (b) and escarole (c) immediately following foliar application of 500 mg Pt NPs/L dispersion.

After reaching a four-leaf (arugula) or five-leaf (escarole) growth stage, either the leaves or roots of the plants were exposed. Plants in the foliar exposure group were administered Pt NPs dispersed in ultrapure water at concentrations of 5, 50, or 500 mg/L using a probe sonication procedure developed in accordance with recommendations by Taurozzi et al. [190]. Exposure was completed over a five day period during which abaxial and adaxial foliar surfaces were covered daily with 2 µL droplets applied with a pipette per 0.5 cm^2 leaf surface (Fig. 3.3b and c). On the day of each exposure during the five day exposure period, 10 mL of a 500 mg Pt NPs/L dispersion were prepared by pulse sonication (10 s pulse, 5 s rest) in a 2.5 cm diameter glass vial on ice for 3 min at 8.58 W. Soil surfaces were covered with Parafilm® to prevent unintended deposition onto soil. In the root exposure group,

one application consisting of 20 mL of 50 mg Pt NPs/L dispersion was evenly applied to the soil surface. Following the week of exposure, plants were grown to maturity for an additional one week (arugula) or four weeks (escarole) before harvesting to reflect their natural life cycles.

3.3.2 Foliar Surface Morphology

Arugula has relatively hydrophobic leaves [191], whereas escarole forms a head of relatively hydrophilic leaves. Hydrophobicity/hydrophilicity (i.e., wettability) is typically assessed by the contact angle formed by a droplet of water on the leaf surface, with lower contact angles (<90°) indicating a hydrophobic surface, and higher contact angles (>90°) indicating a hydrophilic surface [192], [193]. The leaves of both may range from glabrous to mildly hairy. Unexposed and 500 mg Pt NPs/L foliar exposed, lyophilized arugula and escarole leaf samples were mounted on a SEM holder with double-sided carbon tape and coated with ~10 nm Au using an SCD 005 cool sputter coater (BAL-TEC GmbH, Switzerland). The samples were then analyzed with SEM using an accelerating voltage of 15 kV under ultra-high vacuum conditions (9.6×10^{-5} Pa) operating in secondary electron mode. No fewer than 10 images (×250 magnification) of the abaxial and adaxial foliar surfaces were analyzed for stomatal density, proportion of open stomata, and morphological characteristics.

3.3.3 Foliar Surface Free Energy

Surface free energy (SFE) is a quantitative measure of polar and dispersive forces which determine hydrophobicity/hydrophilicity (i.e., wettability). The foliar SFE of plants is dictated by the degree of surface roughness (i.e., wrinkling and presence of nano- and microstructures, which are positively correlated with hydrophobicity) and the chemical and structural composition of the cuticle covering the foliar surface (consisting mostly of cutin, with lower amounts of waxes, phenolics, and polysaccharides). The surface tension of a liquid droplet in combination with the foliar SFE determines the strength of adhesion (i.e., the contact area), which in turn affects internalization [153], [154].

Surface free energy is often estimated using indirect methods which consider the case of liquid droplets from two or three liquids of different polarity on the solid surface of interest (Fig. 3.4). The contact angle, θ, formed between the liquid-vapor interface and the solid surface is related to the surface tension of the solid (SFE) by Young's equation:

$$\gamma_{sv} = \gamma_{sl} + \gamma_{lv}\cos\theta \tag{3.1}$$

in which γ_{sv} is the solid-vapor interfacial tension, γ_{sl} is the solid-liquid interfacial tension between the solid and the liquid droplet, and γ_{lv} is the liquid-vapor interfacial tension, or the surface tension of the liquid droplet [194], [195]. Since the equation contains an additional unknown variable: γ_{sl}, different variations of Young's equation have been developed to deal with this issue [196].

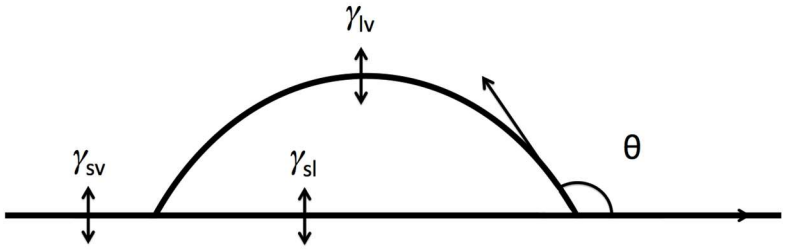

Figure 3.4: Schematic diagram representing the four variables in Young's equation as exhibited in the case of a liquid droplet on a flat, solid surface.

The geometric mean (GM) method is a two-liquid method which considers SFE in terms of the sum of dispersive and hydrogen-bonding forces between the solid and liquid:

$$\gamma_{lv}(1+\cos\theta) = 2\left(\sqrt{\gamma_s^d\gamma_l^d} + \sqrt{\gamma_s^h\gamma_l^h}\right) \tag{3.2}$$

where γ_s^d and γ_l^d and γ_s^h and γ_l^h denote the dispersive and hydrogen-bonding force components of the solid and liquid, respectively. The solid-liquid interfacial tension is represented by $\gamma_{lv}(1+\cos\theta)$ by treating it as the sum of the solid and liquid facial tensions minus the work of adhesion. Solving for SFE is possible because the dispersive and hydrogen-bonding forces can be treated as a geometric mean[197].

The harmonic mean (HM) method was developed by Wu in response to shortcomings of the GM method in estimating SFE for polar solid, polar liquid systems [198]. Instead of treating dispersive and hydrogen-bonding forces as a geometric mean, they are treated as additive forces expressed as reciprocal means:

$$\gamma_{lv}(1+\cos\theta) = \frac{4\gamma_s^d\gamma_l^d}{\gamma_s^d+\gamma_l^d} + \frac{4\gamma_s^h\gamma_l^h}{\gamma_s^h+\gamma_l^h} \tag{3.3}$$

Acid-base theory treats surface tension as the sum of Lifshitz-van der Waals forces (LW: "apolar" or dispersive forces, including London dispersion forces, Keesom dipole-dipole forces, and Debye dipole-induced dipole forces) and acid base (AB: "polar" force) components:

$$\gamma_{lv}(1+\cos\theta) = 2\left(\sqrt{\gamma_s^d\gamma_l^d} + \sqrt{\gamma_s^+\gamma_l^-} + \sqrt{\gamma_s^-\gamma_l^+}\right) \tag{3.4}$$

where γ_s^+ and γ_l^+ and γ_s^- and γ_l^- represent electron-acceptor and electron-donor components of the solid and liquid, respectively [196]. By using one apolar liquid and two polar liquids with known γ_l^d, γ_l^-, and γ_l^+ values, it is possible to determine the LW, or dispersive, and AB surface tension components of the solid [199].

The solubility parameter, (δ) of a foliar surface is related to γ_{sv} through the cohesive energy density (e_c) [192]:

$$e_c = \left(\frac{\gamma_{sv}}{0.75}\right)^{3/2} \tag{3.5}$$

which in turn is used to solve for δ:

$$\delta = (e_c)^{1/2} \tag{3.6}$$

Surface free energy values were calculated using all three methods for the abaxial and adaxial foliar surfaces of both test plants applying recommendations and mean liquid surface tension values provided by Fernández and Khayet [192]. Static contact angles were obtained by applying droplets of ultrapure water, diiodomethane (99% Sigma-Aldrich, Germany), and glycerol (99+%, Alfa Aesar, USA; 5 repetitions each) with a pipette to the foliar surfaces of the test plants. Droplet images were obtained within 10 s of droplet application and measured using a Theta Lite T101 optical tensiometer (Attension, Biolin Scientific, Finland) connected to a computer with Attension Theta software. Contact angle measurements were made for unexposed and exposed leaves at all exposure concentrations after each day of application to compare the daily and cumulative effects of foliar exposure to Pt NPs on SFE. Due to separate locations of the tensiometer and plant chamber, leaves were detached for transport and analysis. To minimize potential variations from leaf to leaf, contact angle measurements were obtained from at least four leaves for each plant surface and exposure condition.

3.3.4 Pt Nanoparticle Adsorption Patterns on Foliar Surfaces

Nanoparticle adsorption patterns on foliar surfaces were investigated using SEM-EDX. Leaf samples were lyophilized at -50°C and 0.2 mbar for 48h before being mounted on a sample holder with double-sided carbon tape and sputter coated with ~10 nm Au. Samples were analyzed at 15 kV under ultra-high vacuum conditions (9.6×10^{-5} Pa) in secondary electron mode. Analysis with EDX was carried out on individual spots of interest.

3.3.5 Pt Measurement in Leaves and Roots

Sample preparation was based on procedures used by Kroflič et al. [200]. During harvesting, fresh roots and leaves were separated, washed, weighed, and frozen until further preparation. Minor amounts of yellowed and rotten leaves (from normal aging) in control and exposed plants were discarded. Leaves were washed in accordance with U.S. Food and Drug Administration [201] and EFSA [202] recommendations for home produce preparation: 30 s under cool running tap water, followed by two consecutive baths in ultrapure water for 1 min each [146]. Samples of the wash water were analyzed with ICP-MS to check for the presence of Pt. Roots were thoroughly washed under cool running tap water and rinsed with ultrapure water. Plant tissues were then stored in a freezer at -20°C until lyophilization at -50°C and 0.2 mbar for 48h. Leaf samples were finely milled with a Fritsch planetary micro mill Pulverisette 7 (Fritsch GmbH, Idar-Oberstein, Germany) and root samples were cut into small (~5 mm) pieces.

Approximately 0.3 g of leaf material or 0.15 g of root material were mineralized in closed Teflon tubes with 4 mL 65% HNO_3 (Suprapur, Merck, Germany) and 0.1 mL HF (Suprapur, Merck, Germany) in a Milestone UltraWAVE microwave digester (Milestone Inc., USA). Samples were heated to 220°C at 100.0 bar (1500 W) over 20 min, maintained under these conditions for a further 15 min (1500 W), and then cooled back to room temperature over a 30 min period. Samples were diluted to 30 mL with ultrapure water. Each sample was prepared in triplicate. Blanks prepared in the same way as samples were included in each run.

Measurement of the Pt concentration in the digested samples was made by ICP-MS in connection with an ASX-510 autosampler (Teledyne CETAC Headquarters, Omaha, NE). The operating conditions were as follows: Babington nebulizer, Scott-type spray chamber,

spray chamber temperature of 5°C, plasma gas flow rate of 15 L/min, carrier gas flow rate of 0.8 L/min, make-up gas flow rate of 0.1 L/min, nebulizer pump 0.1 rps, RF power of 1,500 W, and reaction cell gas He at a flow rate of 4 mL/min. The isotope measured was ^{195}Pt and external calibration was used for quantification. Calibration standards were prepared by dilution of 1,000 mg/L Pt solution (Merck, Germany). Because there are no certified reference materials for the detection of Pt in plant tissues, the efficiency of the analytical procedure was evaluated by spiking samples of leaves and roots from both plants with a known amount of Pt solution before digestion. Analysis of the Pt content following digestion showed that the recovery was 95% ± 9% (mean ± standard deviation [SD], $n = 6$). The limit of detection for Pt was 1.1 µg/L.

3.3.6 Statistical Analysis

Differences in Pt concentrations in different plant segments (leaves and roots; $n = 3$), proportion of open stomata on foliar surfaces ($n = 10$), leaf mass ($n = 3$), and dissolved Pt concentrations between samples treated by ultracentrifugation and ultrafiltration ($n = 3$) were ascertained using the Mann-Whitney test at the $p < 0.05$ significance level. Foliar SFE differences between the abaxial and adaxial surfaces of arugula and escarole as a function of foliar Pt NP exposure were analyzed using a paired t-test ($n = 5$) at the $p < 0.05$ significance level. Normality of the data was tested with the Shapiro-Wilk test and homoscedasticity of the variance was determined using Levene's test [203]. All analyses were completed using OriginPro 2015 software.

Chapter 2

Results and Discussion

4.1 Incense Powder and Emission Characteristics

4.1.1 Incense Chemical Analysis

Results of the elemental analysis indicated the presence of Ca, Si, Fe, and Al together with different organic compounds in the unburned material (Table 4.1). According to the results of XRD and chemical analysis, $CaCO_3$ and SiO_2 were the major inorganic components in both samples. These were probably added as a filler [204]. Organic compounds undergo evaporation and decomposition during slow combustion of the incense stick, with a mass reduction of 86.5% for the African Violet incense and 60.2% for the Strawberry incense. As a consequence, the content of the inorganic compounds is increased. $CaCO_3$ is carboxylated during the combustion and basic CaO is formed, resulting in further absorption of acidic CO_2 from the air, making the speciation difficult to determine. It was previously reported that the presence of Ca in incense sticks decreases the emission of C particles [205]. In order to avoid the influence of CO_2 absorption, the chemical analysis was performed immediately after decomposition and all the samples were kept in a desiccator. Ash obtained after the combustion was found to consist of SiO_2, CaO, and $CaCO_3$, with small quantities of Al_2O_3, Fe_2O_3 and $CaSO_4$.

Table 4.1: Elemental composition of the two incenses before and after combustion expressed as wt.%. S = Strawberry incense; AV = African Violet incense.

Element	S	S, burned	AV	AV, burned
Ca	9.8	12.5	2.2	12.5
Al	0.41	5.36	0.77	5.36
Fe	0.17	2.43	0.242	2.43
Si	7.9	17.2	3.5	24.36
C	44.96	6.02	51.15	6.02
H	3.66	0.25	4.76	0.25
N	0.32	0.03	0.36	0.03
S	0.03	0.13	0.04	0.13
Cl	0	0	0	0
Sum	67.25	51.08	63.02	51.08

Fig. 4.1 shows XRD spectra of Strawberry (Fig. 4.1a) and African Violet (Fig. 4.1b) incenses, both unburned (red line) and burned (black line). For both, the burned sample

is sharper since the leftover ash is more crystalline as all moisture has been removed by burning. All the peaks are preserved after burning for both incenses, with some relative change of intensities. This effect can be attributed to both changes in the chemical composition following burning and to changes in the orientation of crystallites in the samples.

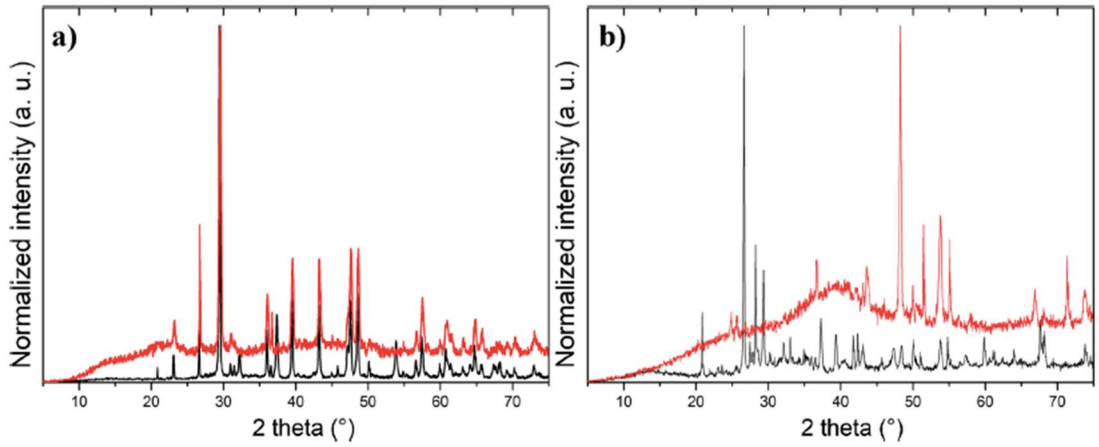

Figure 4.1: Incense XRD spectra: Strawberry (a) and African Violet (b) both unburned (red line) and burned (black line).

For the Strawberry incense before burning, the XRD spectrum corresponds predominantly to the mixture of $CaCO_3$ (ICSD number 024-0027) and SiO_2 (ICSD number 083-0539), with traces of Fe_2O_3 (ICSD number 024-002) and $CaSO_4$ (ICSD number 003-0163). Upon combustion, in addition to $CaCO_3$ and SiO_2, CaO becomes a dominant species (ICSD number 037-1497). African Violet incense has a more complicated pattern, with $CaCO_3$, SiO_2, and CaO as the most prominent compounds, together with small additions of Al_2O_3 (ICSD number 008-0013), Fe_2O_3, and $CaSO_4$. All of these peaks are preserved after burning. These spectra are depicted in more detail in Fig. 4.2. It should be noted that various VOCs (such as nicotinic acid $C_6H_5NO_2$, ICSD number 049-2089 or malononitrile $C_3H_2N_2$, ICSD number 033-1737) can be a match, but they overlap with the much stronger peaks of $CaCO_3$ (024-0027) and SiO_2. Many of these VOCs have been previously identified in incense smoke [206].

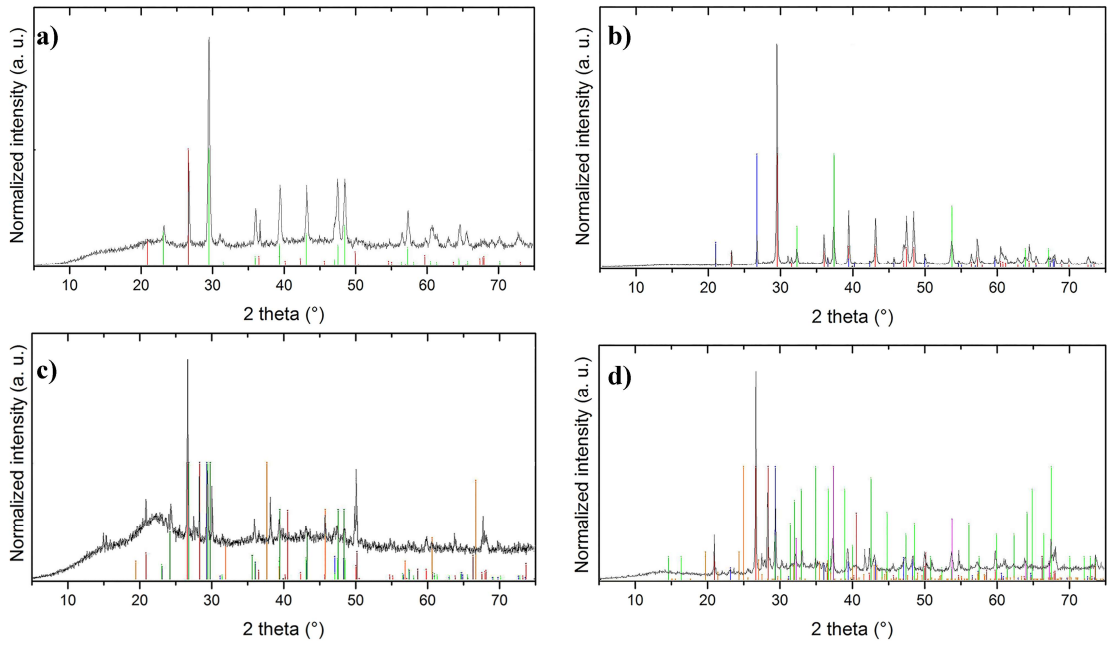

Figure 4.2: Detailed incense XRD spectra of Strawberry incense before (a) and after (b) burning and African Violet incense before (c) and after (d) burning.

Figure 4.3 presents SEM images of both burned and unburned incenses, together with a representative EDX image. The EDX analyses corresponding to Fig. 4.3c and Fig. 4.3f for the Strawberry incense and for Fig. 4.3i and 4.3l for the African Violet incense are summarized in Table 4.2.

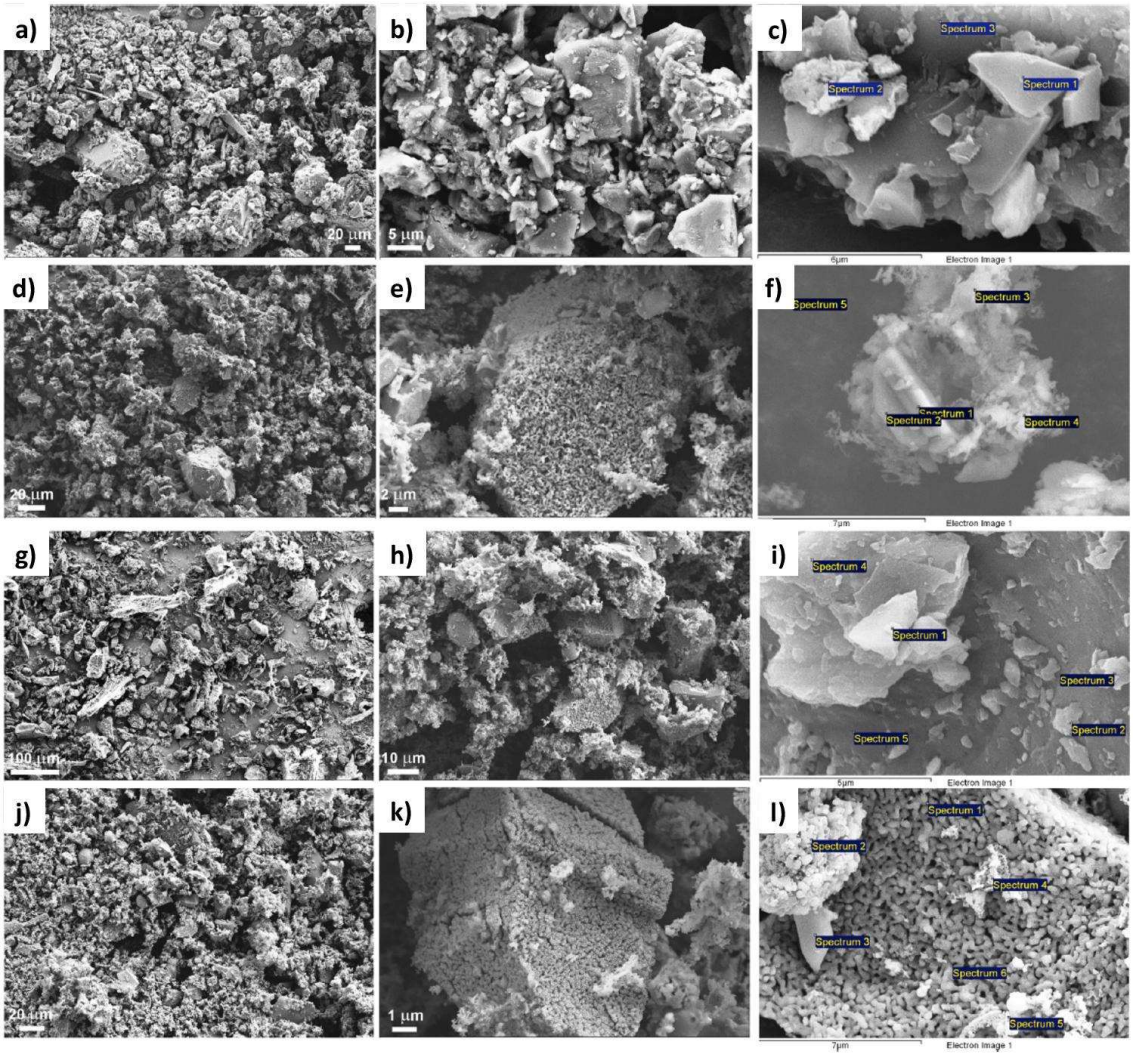

Figure 4.3: SEM micrographs of both incense types. Strawberry incense: unburned (a-c) and burned (d-f) samples; African Violet incense: unburned (g-i) and burned (j-k) samples. Micrographs representing sampling areas for EDX analysis of unburned and burned samples from both incense types are included (c, f, i, l).

The EDX analysis shows that a variety of elements are present inside the incense, with C, O, and Ca being the most abundant. Smaller amounts of Si, Mg, K, Al, and Cl were also detected. Although the presence of Cl was confirmed, this element occurred only sporadically, explaining why it was not detected in the elemental analysis. The exceptionally high amount of oxygen may be attributed to the formation of hydrates. If the incense powder is exposed to ambient conditions, it can absorb water, forming hydrates. It appears that the burning process reduces the size of the material blocks, leaving behind a powder ash. While the bigger blocks have a fairly uniform composition, the powder form is much more complex and contains many different elements.

Table 4.2: EDX analysis of Strawberry and African Violet incense. S = Strawberry incense; AV = African Violet incense; C1-C3, F1-F5, I1-I5, and L1-L6 refer to the corresponding image (c, f, i, l) and position number in Fig. 4.3.

Analysis site	C	O	Mg	K	Al	Si	Cl	Ca	Fe	P
S-C1	81.2	18.1		0.1		0.1		0.5		
S-C2	68.9	28.8	0.2	0.2	0.3	0.4	3.9	1	0.1	
S-C3	85.8	14		0.1				0.1		
S-F1	29	59.7						11.3		
S-F2	26	59						15		
S-F3	27	63				0.2		9.3		
S-F4	25.6	59.6	1.1	1.7	1.8	2.1	0.4	7.1		0.5
S-F5	21	79								
AV-I1		96.2						3.8		
AV-I2		93.1		3.6		3.3				
AV-I3		92		3.7				4.2		
AV-I4		95.3		3				1.7		
AV-I5		72.9					27.1			
AV-L1	9.3	44.4						46.3		
AV-L2	25.1	73.7	1.2							
AV-L3		46.7	1.1	3.8	7.6	22.1		18.7		
AV-L4	27.5	69.2	2.9	0.4						
AV-L5	33.2	64.9	1		0.3	0.6				
AV-L6	31.4	68.6								

4.1.2 Size Distributions and Concentrations of Emitted Incense Particles

The size distribution and total particle concentrations (TPC) of the Strawberry and African Violet incenses released 100 cm from the measurement inlet are shown in Fig. 4.4. The stages at which the initial background particle concentrations were measured, as well as the times when the incense was lit and when it released maximum emissions (close to when the incenses burned out) are clearly visible from the plots. During each burning cycle, the incense was lit following a background measurement period. During burning, the particle concentration kept increasing with time, reaching a maximum concentration just before the incense burned out. Fig. 4.4 contains measurements labeled as S100-2 and AV100-2 in Table 4.3, referring to Strawberry and African Violet incenses, respectively, at the incense distance of 100 cm from the inlet. Two-dimensional (2D) plots for each of the 18 measurements are presented in Fig. 4.5.

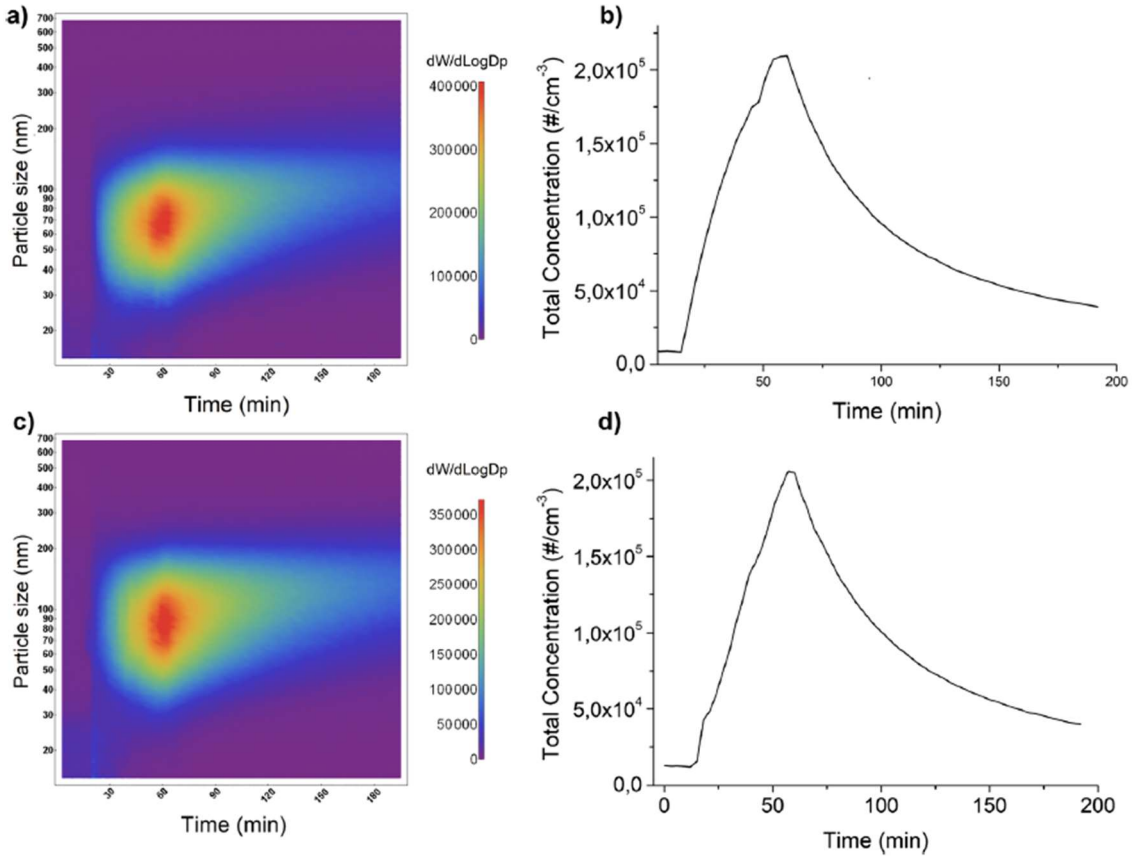

Figure 4.4: Incense particle distribution plots and TPC evolution for Strawberry (a, b) and African Violet (c, d) incense, respectively, burned 100 cm from the measurement inlet.

When the Strawberry incense was measured 100 cm from the inlet, the TPC of the background before the burning of incense commenced was 8 × 10^3 particles/cm^3 while the maximum measured concentration was 2.2 × 10^5 particles/cm^3. Therefore, burning of the Strawberry incense stick resulted in an almost 30-fold increase in the particle concentration with respect to the background levels. Specifically, the first scan after lighting the incense stick (after 3 min) already showed a four-fold increase in the particle concentration. Furthermore, even 100 min after the incense stick burned out, the TPC did not return to the initial levels, remaining six-fold higher than the initial background concentrations at that time. Similar trends were observed for the African Violet incense stick, with the initial background levels being 12 × 10^3 particles/cm^3 and the maximum measured concentration being 2.1 × 10^5 particles/cm^3, or almost 20-fold higher than the initial background concentrations. Similarly, after 100 min, the background concentration was four-fold higher than at the initial point of the measurement. These results are summarized in Table 4.3.

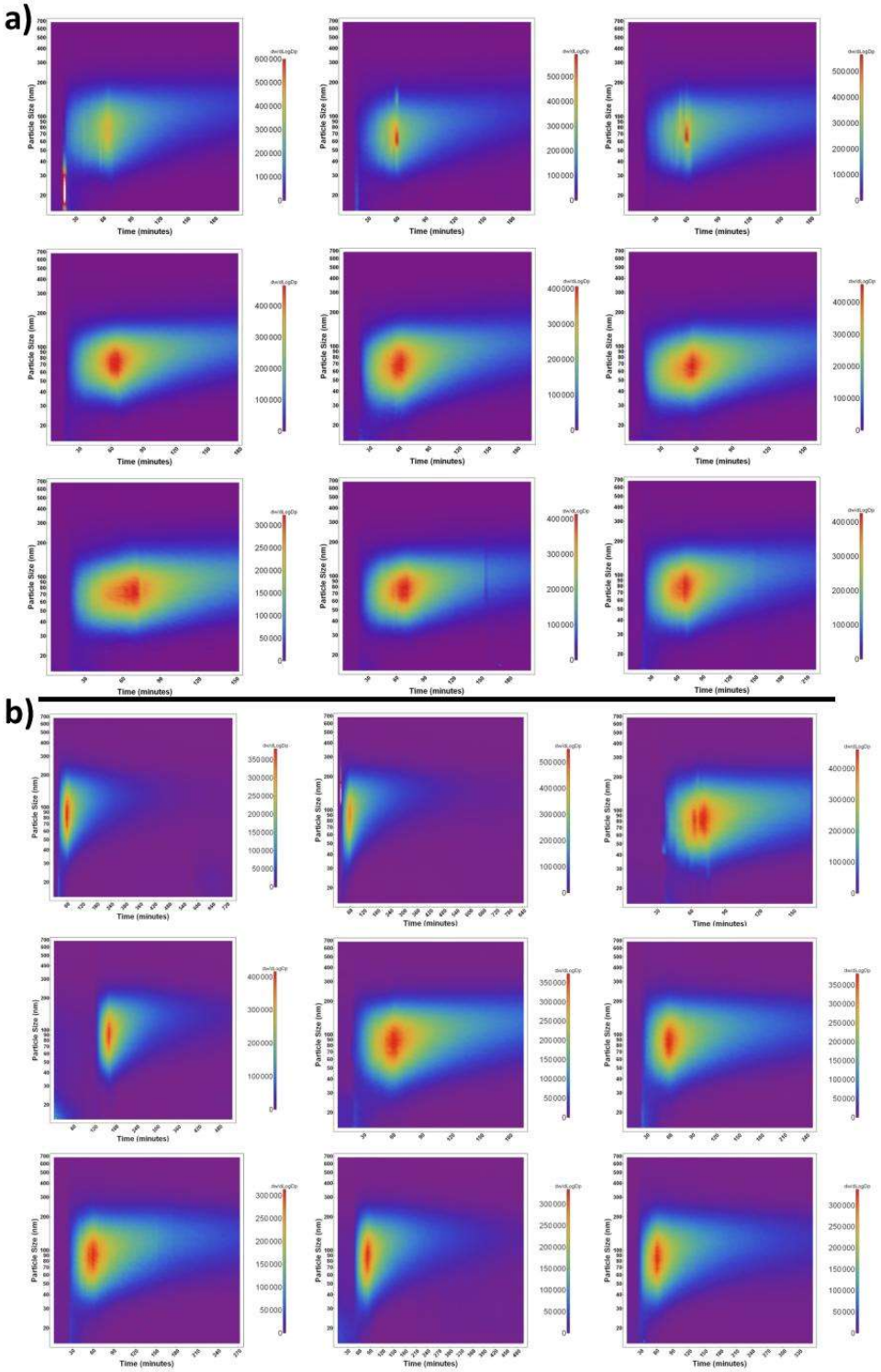

Figure 4.5: Incense particle distribution plots for Strawberry (a) and African Violet (b) incense at the distance of 15 cm (top panel), 100 cm (middle panel), and 300 cm (bottom

panel) from the measurement inlet. Three measurememements were performed at each distance.

Table 4.3: Physical and emission characteristics of Strawberry and African Violet incense. S = Strawberry incense; AV = African Violet incense; 15, 100, 300 refer to distance from the measurement inlet in centimeters; 1, 2, 3 refer to the trial run.

Trial run	Incense mass (g)	Combusted mass (g)	Burning duration (min)	Background TPC (particles/cm^3)	Maximum TPC (particles/cm^3)
S15-1	1.26	0.97	48	0.9×10^4	2.4×10^5
S15-2	1.08	0.81	45	0.8×10^4	2.6×10^5
S15-3	1.03	0.79	45	0.5×10^4	2.4×10^5
S100-1	1.23	0.93	51	0.5×10^4	2.2×10^5
S100-2	1.09	0.75	35	0.8×10^4	2.1×10^5
S100-3	1.23	0.84	45	0.8×10^4	2.2×10^5
S300-1	1.1	0.8	57	0.8×10^4	1.6×10^5
S300-2	1.17	0.9	57	0.4×10^4	1.9×10^5
S300-3	1.23	0.96	54	0.7×10^4	2.1×10^5
AV15-1	0.98	0.83	42	0.4×10^4	2.2×10^5
AV15-2	1.19	1.03	45	0.8×10^4	2.6×10^5
AV15-3	1.12	0.97	48	1.1×10^4	2.9×10^5
AV100-1	0.94	0.81	42	$1{,}1 \times 10^4$	2.1×10^5
AV100-2	0.99	0.87	45	1.2×10^4	2.1×10^5
AV100-3	0.87	0.73	39	0.9×10^4	2.1×10^5
AV300-1	0.89	0.74	36	0.5×10^4	1.7×10^5
AV300-2	1.00	0.85	39	1.7×10^4	1.9×10^5
AV300-3	0.94	0.81	36	0.7×10^4	2.1×10^5

The 2D plots (Fig. 4.4) show that the highest particle concentration, on average, is in the 60 to 100 nm diameter range during incense burning. This is also shown in Fig. 4.6 where the particle concentration over the course of the measurement period is plotted for selected NP sizes (15, 50, 80, 200, and 685 nm). For the smallest measured particle size of 15 nm, the concentration maximum appears at the time when the incense is lit, with the concentration falling immediately after lighting and quickly reaching the initial background levels. This trend is observed for particles up to 30 nm in diameter and has been previously attributed to aggregation, which readily occurs at high particle concentrations (>20,000 particles/cm^3) [37], [53]. Aggregation is especially favored among smaller particles (<50 nm) due to the presence and influence of Brownian motion and van der Waals forces [67]. For particles with a diameter of >30 nm, the concentration increases steadily until the incense burns out, reaching maximum concentrations for particles around 70-80 nm in diameter. The total concentration drops off significantly as the particles reach sizes of >150 nm, while the concentrations of particles ≥300 nm in diameter are consistent with background levels.

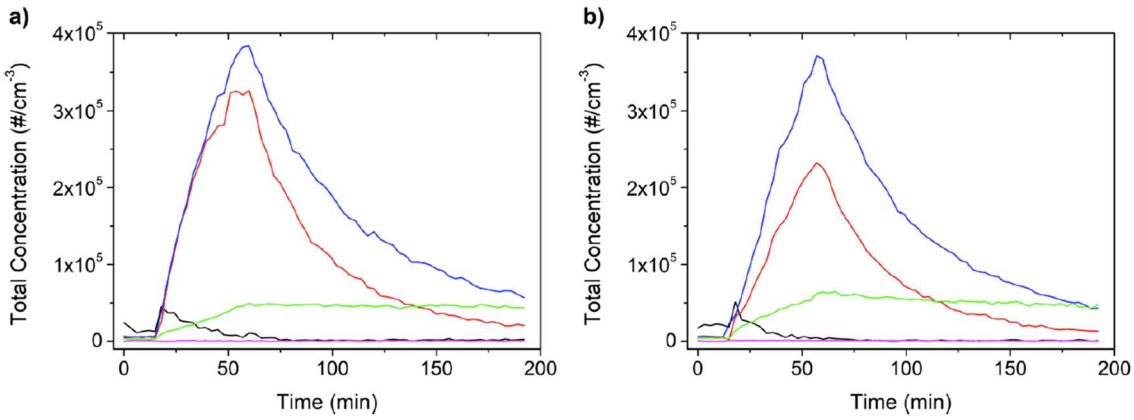

Figure 4.6: Incense total concentration dynamics for different particle sizes: 15 nm (black), 50 nm (red), 80 nm (blue), 200 nm (green), and 685 nm (pink) for Strawberry (a) and African Violet (b) incenses, respectively.

The mass of the incense together with the combusted mass (i.e., the mass of the particles emitted into air, which was calculated by subtracting the mass of the burned incense from that of the unburned incense) and the burning duration are summarized in Table 4.3 for both Strawberry and African Violet incenses. Note that this measurement was conducted differently from the method used for the elemental analysis. In the latter, only the incense powder was used (i.e., scraped from the stick), while for this analysis the stick was burned as well, as in the case of conventional usage. The results suggest that the mass of the incense is not the only parameter governing the burning dynamics; other factors may be shape irregularities and environmental dynamics.

The burning duration together with the TPC for two time periods are summarized in Table 4.4 for both African Violet and Strawberry incenses. The first time period encompasses the burning period of the incense and the second time period comprises the first 60 min following the end of incense burning. The correlation between the burning time and the TPC during both periods is very good. Nevertheless, a better correlation is achieved when the TPC is compared with the combusted mass, as shown in Fig. 4.7. It can be observed that the TPC increases with increasing combusted mass and that this parameter is more influential than the distance from the inlet. Previous researchers have also found that combusted mass is a significant factor affecting PM emissions [63], [66].

Table 4.4: Burning duration and TPC for the total burning period and the 60 min post-burning period, as well as biexponential time constants for Strawberry and African Violet incense. S = Strawberry incense; AV = African Violet incense; 15, 100, 300 refer to distance from the inlet in centimeters; 1, 2, 3 refer to the trial run.

Trial run	Burning duration (min)	TPC during burning (particles/cm^3)	TPC during burning (particles/cm^3)	Time constants (min)
S15-1	48	6.7×10^6	8.8×10^6	8, 66
S15-2	45	4.9×10^6	7.2×10^6	20, 98
S15-3	45	4.5×10^6	6.8×10^6	5, 90
S100-1	51	6.0×10^6	7.8×10^6	22, 112
S100-2	35	5.7×10^6	8.2×10^6	23, 103

S100-3	45	5.8×10^6	8.5×10^6	28, 133
S300-1	57	5.6×10^6	6.0×10^6	33, 151
S300-2	57	6.0×10^6	6.6×10^6	41, 155
S300-3	54	6.7×10^6	7.8×10^6	21, 92
AV15-1	42	4.6×10^6	7.7×10^6	17, 113
AV15-2	45	6.3×10^6	9.4×10^6	18, 110
AV15-3	48	6.4×10^6	9.1×10^6	25, 116
AV100-1	42	4.1×10^6	7.1×10^6	23, 82
AV100-2	45	4.4×10^6	7.0×10^6	37, 148
AV100-3	39	$4{,}4 \times 10^6$	7.7×10^6	19, 90
AV300-1	36	3.7×10^6	6.9×10^6	20, 101
AV300-2	39	3.9×10^6	6.8×10^6	16, 75
AV300-3	36	3.9×10^6	7.5×10^6	30, 130

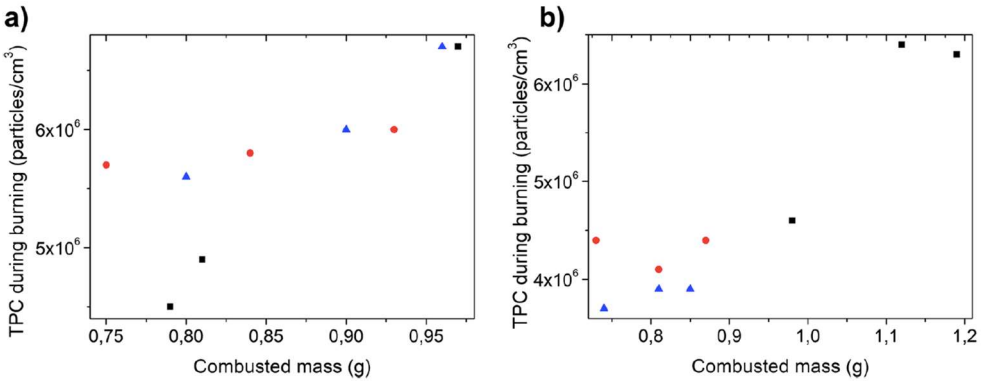

Figure 4.7: Incense TPC as a function of combusted mass for Strawberry (a) and African Violet (b) incense, respectively.

The evolution of the TPC (number of particles/cm^3) with time for all 18 measurements is shown in Fig. 4.8. The particle concentration was observed to decrease following biexponential decay after the burning period. The shorter lifetime was in the range of several tens of minutes, while the longer lifetime was >100 min. The measured data (normalized with respect to the maximum TPC and with the zero time set at the point when the incense burned out) together with a biexponential function fit (shown in the insets) are shown so that the settling of the NPs could be monitored. The R^2 for all the spectra were >0.99. The physical properties of aerosols, including their dynamic behavior, is determined by particle size, which is classified into three modes [207], [208]. Aerosol particles with diameters of <100 nm constitute ultrafine nucleation mode particles whose lifetimes are shorter due to their coagulation or random impaction on surfaces. The second mode observed by this detector is the accumulation mode, comprising particles with sizes of up to 1 µm. These NPs have less efficient removal mechanisms and therefore have longer lifetimes. They can also be formed by the clustering of smaller particles and condensation of vapors onto existing particles. The third, coarse mode, comprises particles that are >1 µm; we did not observe such particles in our measuring system since the impactor removes particles of this size. Therefore, we can attribute the two time constants to the settling time of the two different NP modes: nucleation and accumulation [208].

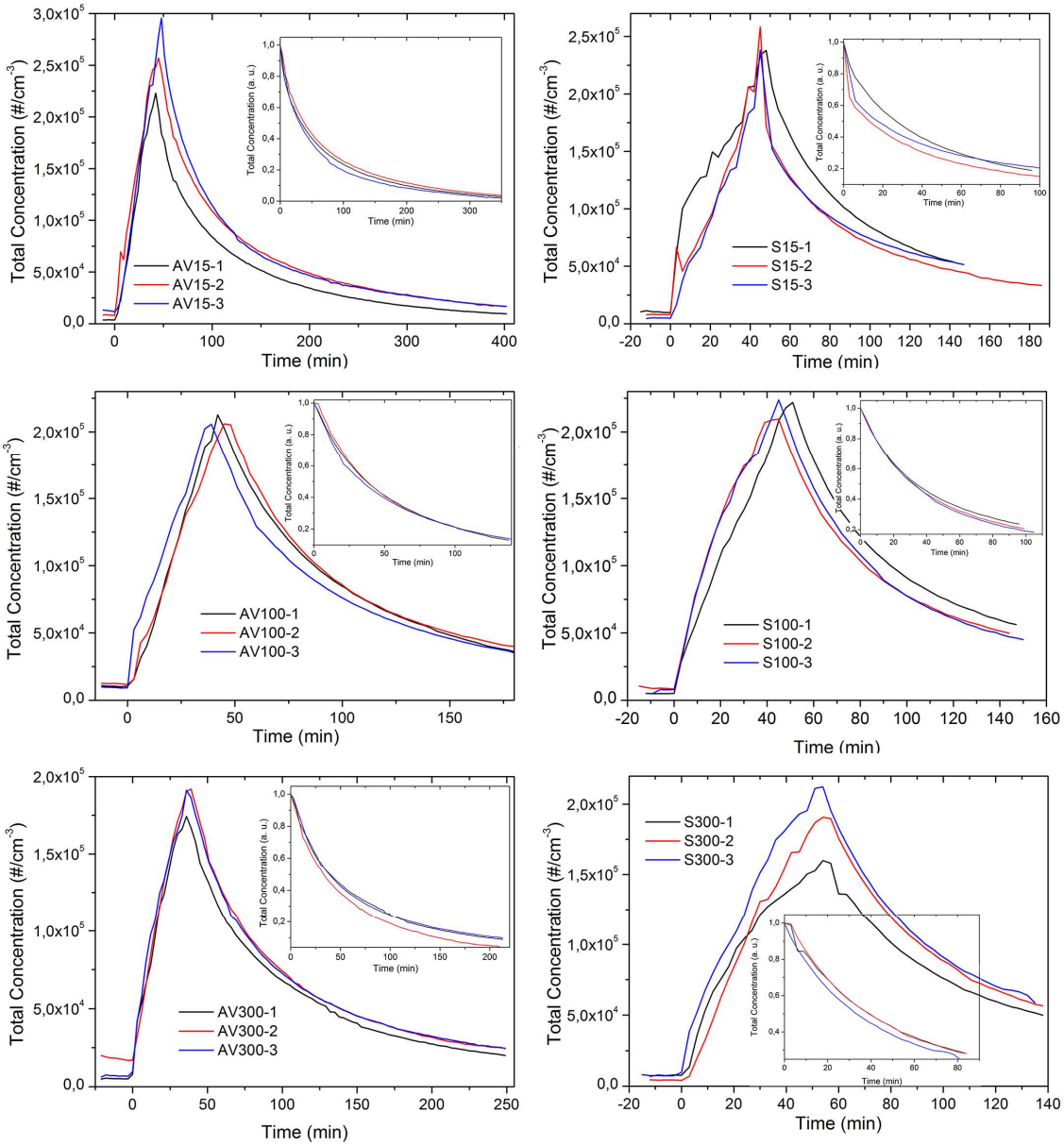

Figure 4.8: Incense TPC with normalized data fitted to a biexponential function: for Strawberry and African Violet incense. S = Strawberry incense; AV = African Violet incense; 15, 100, 300 refer to distance from the inlet in centimeters; 1, 2, 3 refer to the trial run.

The results show slight distance-dependent effects on the size distribution and concentration of the emitted particles. The TPC was found to be higher with decreasing distance to the measurement inlet, primarily due to higher concentrations of particles in the 60-100 nm size range. This observation is consistent with the emitted PM not having as far to travel before reaching the measurement inlet and therefore, nucleation mode particles did not coagulate to as significant a degree as those emitted from burning incense located further from the measurement inlet. Similar observations were reported in a comparable study in which incense particle emissions were measured at varying distances from a measurement inlet under conditions of low ventilation in a room setting [42], [50].

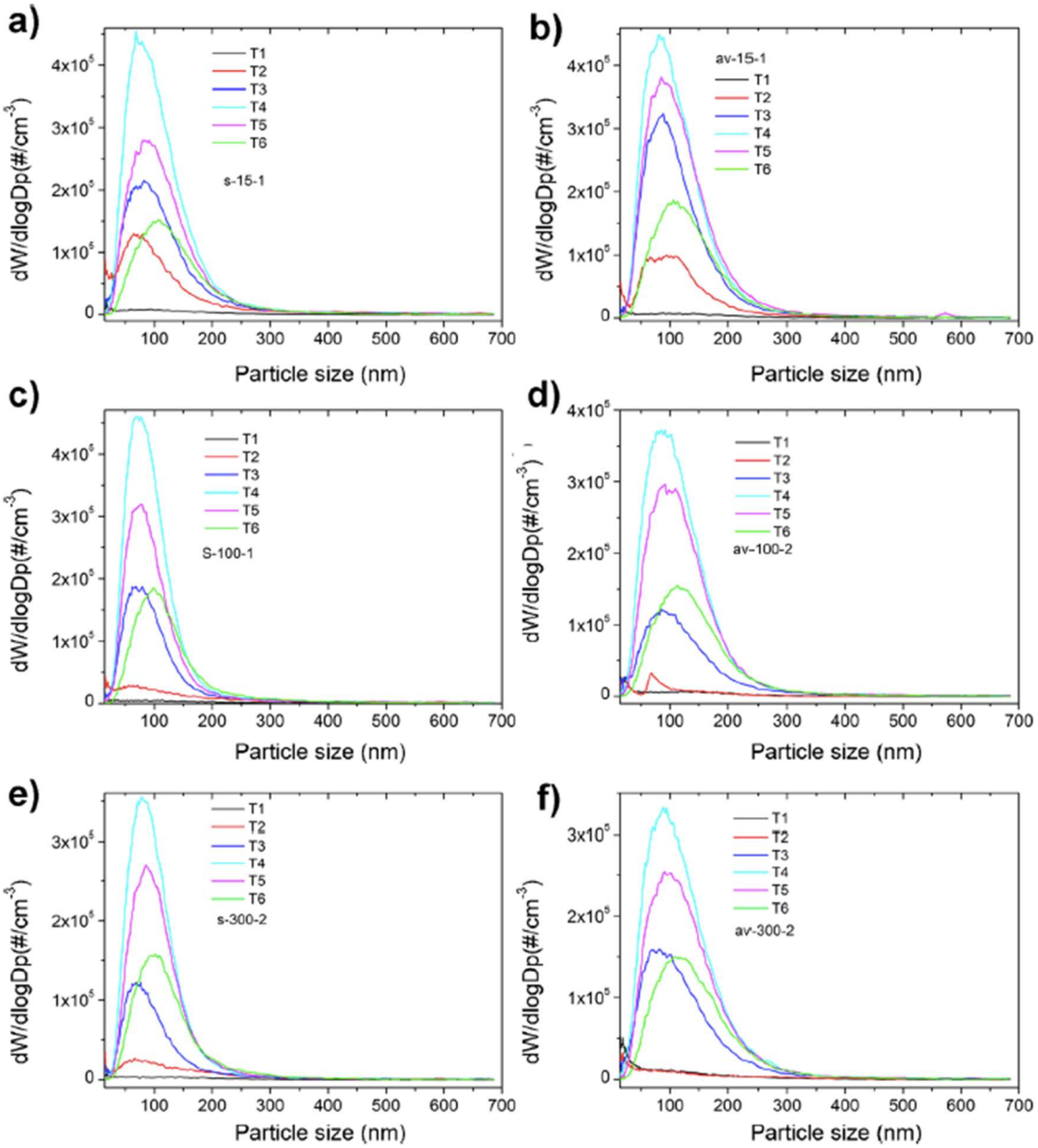

Figure 4.9: Incense particle size distribution spectra for selected timepoints including the background prior to the incense being lit (T1, black line), the first measurement after the incense was lit (T2, red line), 15 min into the burning period (T3, blue line), burnout of the incense (T4, cyan line), 15 min after burnout (T5, pink line), and 1 h after burnout (T6, green). Particle size distribution spectra are shown for Strawberry incense placed 15 (a; S-15-1), 100 (c; S-100-1), and 300 (e; S-300-2) cm from the measurement inlet and for African Violet incense placed 15 (b; AV-15-1), 100 (d; AV-100-2), and 300 (f; AV-300-2) cm from the measurement inlet.

Particle size distributions, depicted in Fig. 4.9, are shown for selected time points during and after the burning period. The chosen time points include the background period prior to the incense being lit (T1, black), the first measurement after lighting the incense (T2, red), 15 min into the burning period (T3, blue), burnout of the incense (T4, cyan), 15 min after burnout (T5, pink), and 1 h after burnout (T6, green). It can be seen throughout the

burning period that the peak particle size (maximum NP concentration) varies only about 5 nm (averaging around 85 nm for African Violet incense and 80 nm for Strawberry incense). When the burning process is over, the peak can be seen to shift to larger sizes (by approximately 25 nm), indicating that NPs undergo agglomeration as they settle. Furthermore, the pink line representing the distribution at 15 min after the burnout shows that the peak does not shift significantly, confirming that this time period is not sufficiently long for particle agglomeration.

4.1.3 Size-Specific Mass Distribution of Emitted Incense Particles

Information on the size-specific mass distribution of particles emitted during incense combustion was obtained using a DLPI. In the case of Strawberry incense, the total collected mass after 350 min of measurement was 0.854 mg. By weighing the filters individually, we found that NPs (diameters ranging from 30-100 nm) amounted to 0.416 ± 0.1 mg, or 50 ± 10% of the total mass of the emitted particles; particles with sizes of 100-1,000 nm amounted to 0.378 ± 0.1 mg, or 40 ± 10% of the total mass of the emitted particles; and particles with diameters from 1-10 µm constituted only 0.6 ± 0.1 mg, or 7 ± 10% of the total mass.

For African Violet incense, the total collected mass after 500 min of measurements was 1.422 mg. For this incense, NPs (up to 100 nm in diameter) amounted to 0.349 ± 0.1 mg, or 25 ± 10% of the total mass of emitted particles; particles in the 100-1,000 nm range constituted 0.998 ± 0.1 mg, or 70 ± 10% of the total mass of emitted particles, and particles in the range of 1-10 µm amounted to only 0.075 ± 0.1 mg, or 5 ± 10% of the total mass of emitted particles. These observations are consistent with the total NP concentration evolution analysis which implies that NPs larger than a few microns in size were not present. These results are in close agreement with a previous study which found that among the fraction of emitted incense particles <5.6 µm in diameter, 95% (by mass) were <1.0 µm in diameter [209].

The filters were subsequently analyzed with SEM-EDX, as the amount of material was not sufficient for other methods such as XRD. In Fig. 4.10, SEM images of collected particles from the DLPI are shown. Particle diameters range from a few microns down to 20 nm. The smallest NPs usually agglomerate into micron-sized particles, as seen in Fig. 4.10a. The EDX analysis is summarized in Table 4.5 and shows that most of the particles are made from C, but other elements can also be found. An Al substrate is used in the DLPI; therefore, the Al concentration cannot be determined from EDX measurements. Our finding that emitted incense particles were predominantly carbonaceous particles containing small proportions of metal(loids) is consistent with the findings of previous studies [35], [36], [39]. It has been found that emitted particles may also be composed of liquids which solidify prior to coagulation with surrounding particles [42].

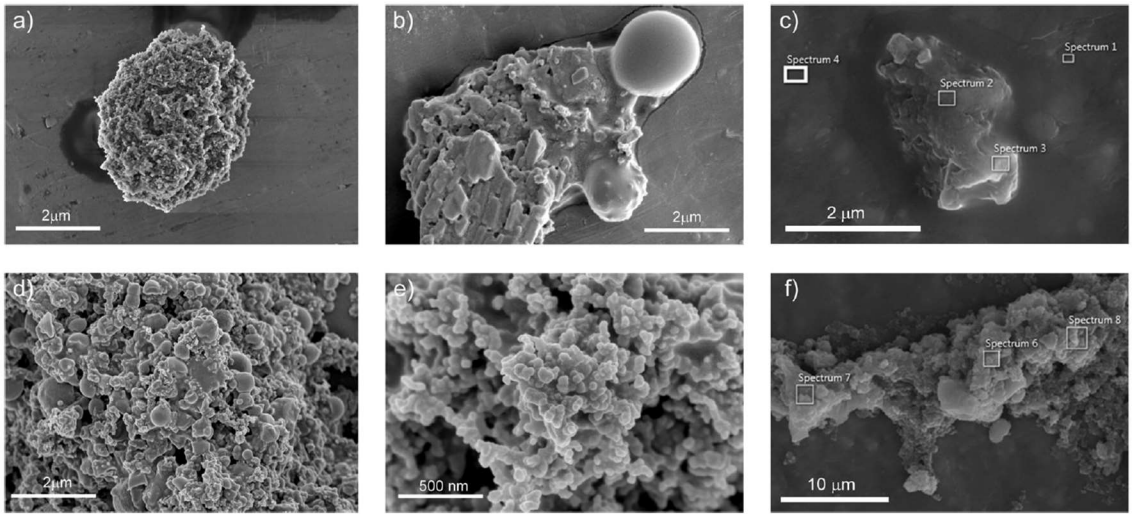

Figure 4.10: SEM micrographs of African Violet incense collected with a DLPI, including representative images (c, f) for EDX analysis.

Table 4.5: EDX analysis of African Violet incense collected from a DLPI, corresponding to points in Fig. 4.10c and Fig. 4.10f.

Analysis site	C	O	Na	Mg	Al	Si	S	Cl	K	Ca	Fe
C1	24.2				75.5						
C2	70.3	12.8	0.2	0.2	13.8	0.7	0.2	0.4	0.1	0.8	0.3
C3	46.3	35.4	1.6		9.0	6.0		0.1		1.0	0.3
F6	59.0	29.3	1.6	0.8	2.0	0.4	1.2	0.5	4.2	0.6	
F7	50.5	28.8	5.9	0.3	4.6	0.3	1.3	4.0	2.6	0.9	0.4
F8	72.9	20.9	0.8	0.2	1.2	0.2	0.9	0.2	1.3	0.1	1.0

4.1.4 Discussion

This work supports previous findings that incense burning greatly contributes to air pollution both in terms of TPC and in terms of the dominant fraction of total emitted particles that is present as NPs. Under conditions of low ventilation it was shown that concentrations of emitted particles remained elevated up to 100 min past the completion of incense burning, with the particles exhibiting size-dependent biexponential decay [210].

Incense burning at a distance of 100 cm from the measurement inlet increased the TPC by nearly 30 times and 20 times in the cases of Strawberry and African Violet incense, respectively. In other studies, increases in TPC from background levels have ranged from three- to five-fold higher [42], [62] to more than nine-fold higher [50]. This variation can be attributed to different experimental burning periods (shorter burning periods result in less emitted PM) and to differences in the combusted mass, with greater mass combustion resulting in higher concentrations of emitted PM [48], [63], [66].

The highest particle concentrations measured during incense burning were in the range of 60-100 nm. This finding is consistent with most studies conducted to date which have reported the highest particle concentration of emitted incense particles as being in the size range of approximately 70-180 nm [42], [43], [62], [64]. However, Jetter et al. [41] detected

the highest concentration of particles in the 30-60 nm size range for 23 different types of incense. This result was likely due to the design of the testing chamber. It has been shown that variations in the peak particle size are in general mostly related to the degree of ingredient milling [42], with finer milling being associated with higher concentrations of smaller particles from incense burning [64]. Other factors, such as testing room/chamber size, temperature, and humidity, have been found to have a negligible effect on the count median diameter and size distribution of emitted incense particles [42].

Once burning was completed, the total NP concentration was found to decay exponentially with two lifetimes of several tens of minutes for particles up to 100 nm and for longer than 100 min for particles >100 nm in size. Various modeling techniques for studying indoor particle dynamics have been reported [208], [211]–[213]. Some of the main parameters governing the modeling are ventilation supply, direct emissions of the particles, surface deposition, and mixing and resuspension of the particles. Therefore, deciphering the exact decay mechanisms requires an exacting control of all these external parameters, which was beyond the scope of this study. Nevertheless, the biexponential fitting of data, although a simplified model, matched the experimental data to a high degree. In previous related studies, exponential decay was clearly demonstrated in graphs depicting TPC decrease with time, but this phenomenon was not labeled as such and not described [37], [62], [64]. In two other studies, particle decay was examined, but because the results were obtained and presented in units of mass per unit volume of air, it was not possible to discern the size- and concentration-dependent mechanisms responsible for the decrease in TPC [53], [66]. In yet another study, particle decay was examined primarily in terms of particle dispersion to adjacent rooms within a multi-room setting [62]. Given the generally close similarity of the emission characteristics of burning incenses across different studies (particularly in terms of predominant fine particle emissions), we would expect to find similar particle decay patterns under varied conditions of our experimental setup so long as low ventilation would be maintained [41]–[44], [62], [64].

In this study, it was also shown that under conditions of low ventilation, the TPC remained approximately six-fold higher even 100 min after the completion of incense burning. This finding is consistent with the fact that accumulation mode particles comprise the main fraction of the TPC. It is difficult to compare our findings with those from other studies due to differences in incense type, burning duration, and ventilation rate. Complete particle decay has been found to take place in as little as 40 min [64] and in as much as 1-2 h [62] and >6 h [50]. Many factors influence particle decay, including surface deposition from sedimentation, diffusion, and impaction (e.g., walls, floors, and other available surfaces), particle agglomeration, and changes in particle mass due to the evaporation and condensation of volatile components [53], [66]. Generally, the TPC decreases much more quickly under conditions of high ventilation due to increased surface deposition [53]. In one study, ventilation decreased PM_{10} concentrations by approximately nine times in comparison to unventilated conditions [50].

On the basis of our results and the findings of previous studies, incense emissions can be expected to pose a significant health risk if used regularly. This is partly due to the chemically complex nature of incense PM emissions. Chuang et al. [42] found that the presence of multiple chemicals and metal(loids) on the surfaces of emitted incense particles was responsible for approximately 30% of oxidative DNA damage in the Plasmid Scission Test in comparison to nano-carbon black. In particular, it has been noted that the more water-soluble metals, such as As, Cd, Mn, and Ni, which have previously been identified in various brands of incense, are especially hazardous due to their increased bioavailability in comparison to water-insoluble metal(loids) (See & Bala 2011). Yang et al. (2007) reported that the toxic equivalency value of solid-phase PAHs was 40-fold greater than the toxic equivalency value of gas-phase PAHs emitted by incense. In this work, chemical

analysis indicated substantial quantities of Ca and Si (in the forms of $CaCO_3$ and SiO_2, and CaO), along with smaller amounts of Al and Fe (in the form of Al_2O_3 and Fe_2O_3). These findings generally concur with previous studies despite expected variations between different brands and types of incense. On average, Ca has been identified as a dominant element in incense, along with lesser amounts of Al, Fe, Mg, and K [36], [63]. See and Balasubramanian [39] found Al and Fe to be the dominant metals in six types of unburned incense, while Chuang et al. [35] identified relatively large concentrations of Zn and Cu in two out of three types of incense they tested, with Fe falling below the limit of detection for all three types of incense. Although the relationship between elemental content and emission factors was not identified in this study, previous investigations have shown that an increased metal content in unburned incense is associated with decreased PM emissions, while increased C content is associated with increased PM emissions [39]. In the case of C content, a 1% decrease led to a 2.6 mg/g decrease in emitted material [63].

Another significant risk factor associated with incense burning is the size of the emitted particles. The finding that the peak particle size during incense burning was 85 nm is concerning given that particles ≤100 nm (i.e., ultrafine particles) are most likely to be inhaled into the alveolar region of the lungs, where they pose the greatest risk to human health [64]. At 1 h after completion of the burning period, the peak particle size only increased to approximately 110 nm. This indicates that a substantial proportion of ultrafine PM emissions remained airborne and available for inhalation for significant periods of time after incense burned. In one study investigating the respirable fraction of fine PM emitted from five different indoor household activities, the total lung deposition fraction of emitted incense particles was found to be 0.32 ± 0.03, of which 56.7-68.1% were found to be capable of depositing in the alveolar region of the lungs [43]. Emitted particles are also likely to be ingested any time incense is burned in the vicinity of food and drinks, such has when incense is burned to mask cooking odors [214].

While in this investigation we focused on PM emissions from incense burning, this does not fully portray the human health risks of this activity. Harmful CO, NO_X, SO_2, VOCs (e.g., formaldehyde), and PAHs are also emitted, often at concentrations that exceed national and international ambient air quality guidelines [37], [41], [46]–[48], [51], [62], [209]. Furthermore, emitted gases were found in one study to decay over longer periods of time in comparison to PM (Cohen 2013). Various measures can be taken to reduce exposure to incense PM and gas emissions, including the use of smokeless or short-burning incense, the selection of incense with non-toxic ingredients, and increasing ventilation to sites of incense burning [37], [39], [42], [50], [62], [209]. It should be noted that while smokeless incense releases fewer total particles [209], it has been found to release higher quantities of ultrafine particles in comparison to regular incense [64]. In another study, incenses marketed as 'environmentally friendly' were found to emit higher concentrations of PAHs and oxygenated PAHs compared to regular incenses [49]. Therefore, incenses claiming to emit fewer pollutants should still be used with caution.

4.2 Arugula and Escarole Responses to Pt Nanoparticle Exposure

4.2.1 Pt Nanoparticle Characterization

Examination of the Pt NPs by SEM and TEM (Fig. 4.11a and b, respectively) showed that they were spherical in shape. Measurements of 300 randomly selected Pt NPs in TEM images with ImageJ software indicated an average particle size of 13 ± 6 nm and a size distribution from 3-56 nm. The specific surface area measured with BET analysis was

10.65 m^2 g^{-1} Pt NPs and the chemical identity of the Pt NPs was confirmed using EDX (Fig. 4.11c).

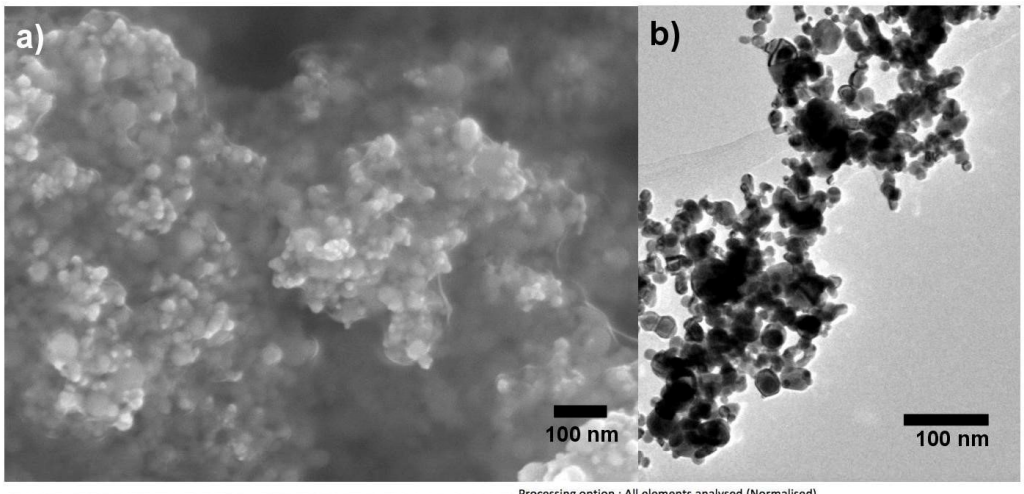

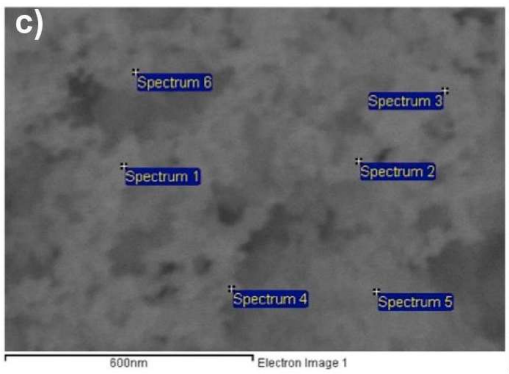

Processing option : All elements analysed (Normalised)

Spectrum	In stats.	C	O	S	Pt	Total
Spectrum 1	Yes	19.30	2.52		78.18	100.00
Spectrum 2	Yes	18.71	2.01		79.27	100.00
Spectrum 3	Yes	22.47	3.03	0.96	73.54	100.00
Spectrum 4	Yes	12.17	2.13	0.83	84.87	100.00
Spectrum 5	Yes	16.89	2.49		80.61	100.00
Spectrum 6	Yes		2.92	1.15	95.93	100.00
Max.		22.47	3.03	1.15	95.93	
Min.		12.17	2.01	0.83	73.54	

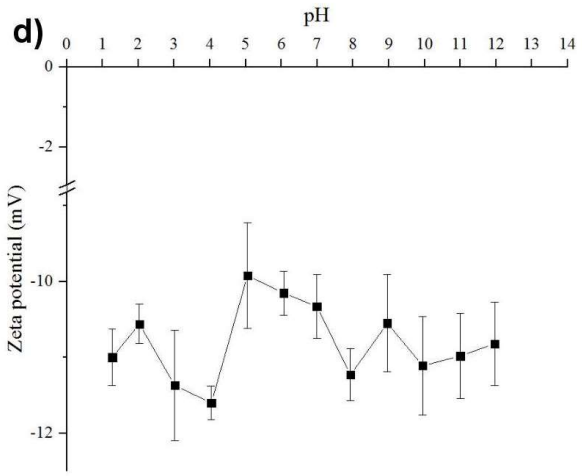

Figure 4.11: Results of Pt NP characterization including: SEM and TEM micrographs of Pt NPs (a and b, respectively), Pt NP EDX data along with a corresponding SEM micrograph indicating the points of analysis (c), and a graph depicting the zeta potential of Pt NPs dispersed in ultrapure water (50 mg/L) across the pH scale (d). Error bars represent the standard error (SE; number of replicates [n] = 5).

In aqueous dispersion, Pt NPs had an average hydrodynamic diameter of 121.6 ± 1.4 nm with an average polydispersity index of 0.15 ± 0.03, as obtained from

triplicate DLS measurements. The zeta potential of the dispersions was measured throughout the pH range, but the point of zero charge was not reached (Fig. 4.11d).

The total concentrations of Pt detected in the acidified experimental Pt NP dispersions were in excellent agreement with the nominal values, exhibiting ≤ 3.0% deviation (Table 4.6). Concentrations of dissolved Pt in the supernatant of samples treated by ultracentrifugation and ultrafiltration were extremely low, confirming reports from the literature that Pt NPs barely dissolve [189], [215]. However, the supernatant of ultracentrifuged samples contained higher concentrations of dissolved Pt compared to the supernatant of ultrafiltered samples (Table 4.6). These results are consistent with the fact that dissolved metal concentrations tend to be overestimated in ultracentrifuged samples due to the difficulty of removing the liquid supernatant containing the dissolved metal ion fraction without re-suspending some of the sediment particles. Conversely, dissolved metal concentrations tend to be underestimated in ultrafiltered samples due to the adsorption of metal ions onto the filter [216]. Nonetheless, statistical differences were not detected when dissolved Pt concentrations measured in ultracentrifuged and ultrafiltered samples were compared (Mann-Whitney test, $n = 3$, $p < 0.05$).

Table 4.6: Pt NP experimental concentrations and dissolution. All data are mean ± SD (n = 3). *The dissolved Pt fraction (%) is provided in terms of ultracentrifugation in the cases of Pt NPs dispersed in water (5, 50, and 500 mg/L) and in terms of ultrafiltration in the cases of Pt NPs and arugula and Pt NPs and escarole.

Sample	Nominal Pt concentration (mg/L)	Total measured Pt concentration (mg/L)	Pt concentration in supernatant after ultracentrifugation (µg/L)	Pt concentration in supernatant after ultrafiltration (µg/L)	Dissolved Pt fraction (%) with corresponding Pt concentration in supernatant (in parentheses)*
Pt NPs	5	5.019 ± 0.073	2.070 ± 0.412	0.178 ± 0.022	0.041 ± 0.008 (2.070 ± 0.412)
	50	50.409 ± 0.914	5.993 ± 0.413	1.718 ± 0.063	0.012 ± 0.001 (5.993 ± 0.413)
	500	514.485 ± 11.055	36.277 ± 6.160	19.145 ± 5.523	0.007 ± 0.001 (36.277 ± 6.160)
Pt NPs and arugula	5	5.019 ± 0.073		0.709 ± 0.044	0.014 ± 0.001 (0.709 ± 0.044)
Pt NPs and escarole	5	5.019 ± 0.073		0.457 ± 0.005	0.009 ± 0.000 (0.457 ± 0.005)

The concentrations of dissolved Pt ions in the supernatant of samples containing Pt NPs with either arugula or escarole leaves were approximately 4.0 and 2.6 times greater, respectively, than the corresponding concentration of dissolved Pt measured in the bare dispersion treated by ultrafiltration (the mean leaf mass ± SD was 0.243 ± 0.022 g arugula and 0.156 ± 0.026 escarole; Table 4.6). Due to incomplete sedimentation of the samples treated by ultracentrifugation and the frothy appearance of the liquid after filtration, only samples treated by ultrafiltration were analyzed to avoid measurement discrepancies (Fig. 3.2).

4.2.2 Leaf Surface Characteristics and Pt Nanoparticle Adsorption Patterns

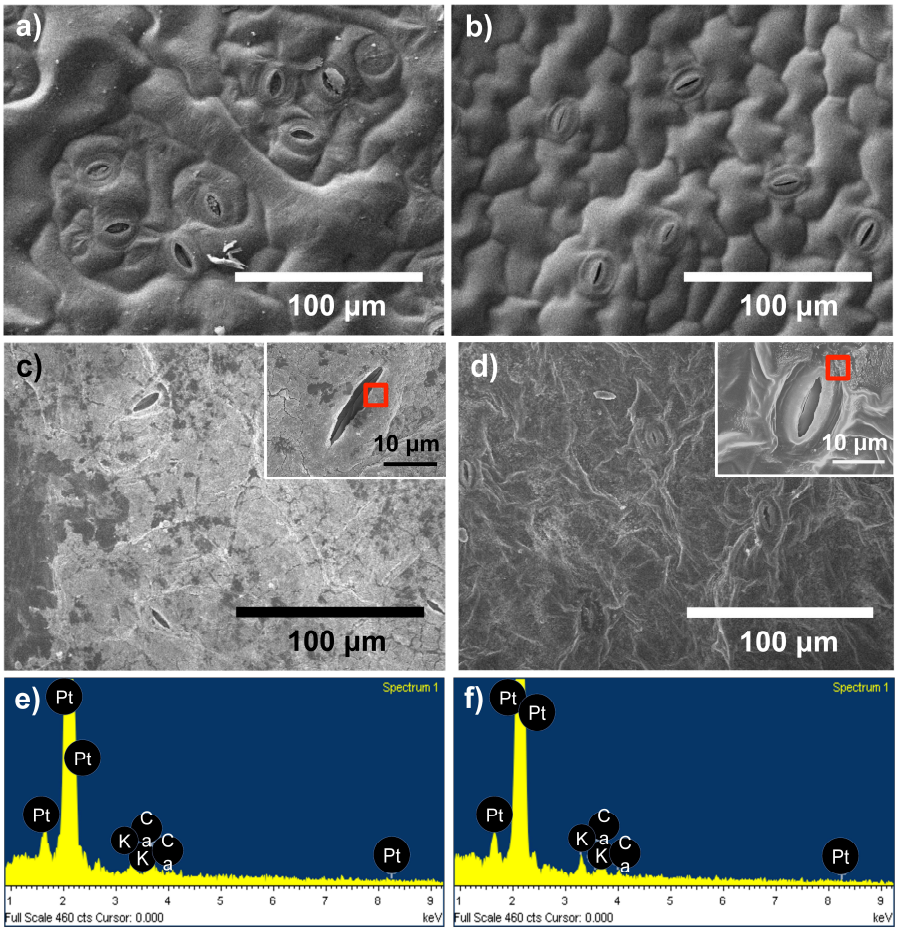

Figure 4.12: SEM micrographs of arugula and escarole abaxial foliar surfaces of control (a, b) and 500 mg Pt NPs/L foliar-exposed arugula and escarole, respectively, with the magnified stomata presented as inserts (c, d). EDX spectra (e, f; arugula and escarole, respectively) for the red-boxed area (inserts in c, d) on exposed leaves confirms the presence of Pt NPs, which appear as white particles.

Image analysis of unexposed, lyophilized arugula and escarole leaf samples (Fig. 4.12a and b, respectively) revealed a low degree of surface roughness with similar stomatal densities between the two plants and between abaxial and adaxial surfaces: arugula abaxial surface: 107.0 ± 2.3 stomata/mm^2; arugula adaxial surface: 85.6 ± 15.9 stomata/mm^2; escarole abaxial surface: 98.6 ± 7.6 stomata/mm^2; escarole adaxial surface: 69.5 ± 9.9

stomata/mm^2. Escarole was found to contain low numbers of trichomes on the abaxial (4.6 ± 3.6 trichomes/mm^2) and adaxial (1.1 ± 2.4 trichomes/mm^2) surfaces whereas no trichomes were found on arugula foliar surfaces. Statistical means comparison to determine changes in the proportion of open stomata with foliar exposure to 500 mg Pt NPs/L (Mann-Whitney test, $n = 10$, $p < 0.05$) indicated decreases in the proportion of open stomata for adaxial and abaxial arugula surfaces (no open stomata were found), a significant increase for escarole abaxial surfaces, and no difference for escarole adaxial surfaces (Table 4.7).

Table 4.7: Characterization of stomata on arugula and escarole foliar surfaces. All data are mean ± SD ($n = 10$). *Significant difference from the control according to the Mann-Whitney test ($p < 0.05$).

		Arugula		Escarole	
Foliar exposure	Parameter	Abaxial surface	Adaxial surface	Abaxial surface	Adaxial surface
Control	Stomata/mm^2	107 ± 2.32	85.6 ± 15.9	98.6 ± 7.59	69.5 ± 9.94
	Proportion of open stomata (%)	63.5 ± 11.2	60.6 ± 16.0	11.4 ± 12.0	16.7 ± 9.18
500 mg Pt NPs/L	Stomata/mm^2	104 ± 4.05	86.0 ± 11.7	96.3 ± 4.63	68.1 ± 10.4
	Proportion of open stomata (%)	0*	0*	29.2 ± 13.4*	23.4 ± 16.8

Observation with SEM did not show any differences in the Pt NP adsorption patterns between the abaxial and adaxial foliar surfaces of each plant; however, clear differences were observed between arugula and escarole leaves exposed to the 500 mg/L dispersion over a five day exposure period (Fig. 4.12c and d, with EDX spectra confirming the presence of Pt on both plants presented in Fig. 4.12e and f for arugula and escarole, respectively). While Pt NPs on escarole foliar surfaces (Fig. 4.12d) were agglomerated into discontinuous islands of Pt nano- and microparticles, on arugula they appeared as a nearly unbroken sheet of highly aggregated/agglomerated particles (Fig. 4.12c). Similarly, the magnified images of stomata showed relatively low amounts of Pt NPs around escarole stomata, primarily as loose agglomerates (insert in Fig. 4.12d), whereas relatively large amounts of Pt NPs were caked around the stomata of arugula as loosely bound agglomerates and tightly bound aggregates (insert in Fig. 4.12c). The appearance of the Pt NPs on arugula leaf surfaces was consistent with the fact that water droplets do not spread out over surfaces with low SFE, and hence the Pt NPs on arugula were concentrated over a smaller surface area relative to Pt NPs on escarole.

None of the exposed leaves exhibited necrosis in response to Pt NP exposure (Fig. 4.13). However, means comparison of the leaf masses from control and exposed plants (Mann-Whitney test, $n = 3$, $p < 0.05$) showed that the mass of 500 mg Pt NPs/L foliar-exposed arugula leaves was significantly lower than the leaf mass from the other arugula groups (5 and 50 mg Pt NPs/L foliar-exposed, root-exposed, and control groups), and that the mass of root-exposed arugula leaves was significantly higher than that of the other arugula groups (i.e., 5, 50, and 500 mg Pt NPs/L foliar-exposed and control groups; Table 4.8).

Table 4.8: Dry weight leaf masses of arugula and escarole at harvest. All data are mean ± SD ($n = 3$, 5 plants per replicate). *Significant difference from the control according to the Mann-Whitney test ($p < 0.05$).

Plant	Exposure	Pt NP treatment	DW leaf mass (g)
Arugula	Control	0 mg/L	5.47 ± 0.21
	Root	50 mg/L (20 mL)	6.61 ± 0.93*
	Foliar	5 mg/L	3.72 ± 0.57
		50 mg/L	4.30 ± 1.25
		500 mg/L	2.82 ± 0.16*
Escarole	Control	0 mg/L	5.02 ± 1.43
	Root	50 mg/L (20 mL)	4.81 ± 1.71
	Foliar	5 mg/L	5.91 ± 0.35
		50 mg/L	4.98 ± 0.35
		500 mg/L	4.49 ± 0.45

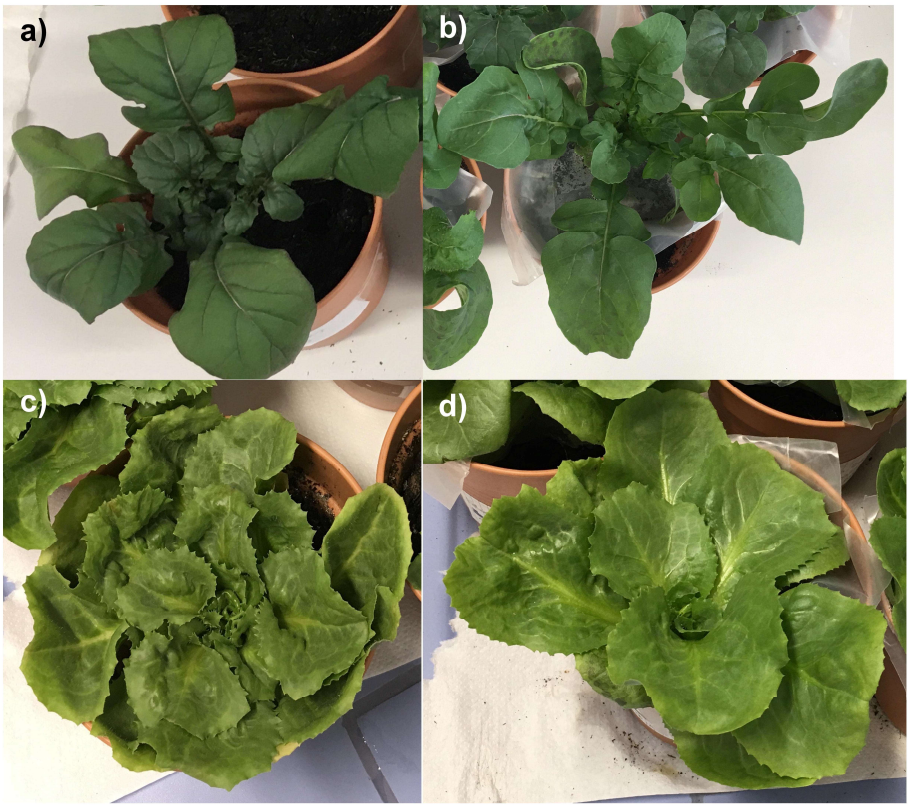

Figure 4.13: Photographs of arugula (a, b) and escarole (c, d) plants at harvest (control and 500 mg Pt NPs/L foliar exposed plants on the left and right hand side, respectively). No leaf necrosis was observed as a result of the Pt NP experimental exposures.

4.2.3 Surface Free Energy Response to Pt Nanoparticle Exposure

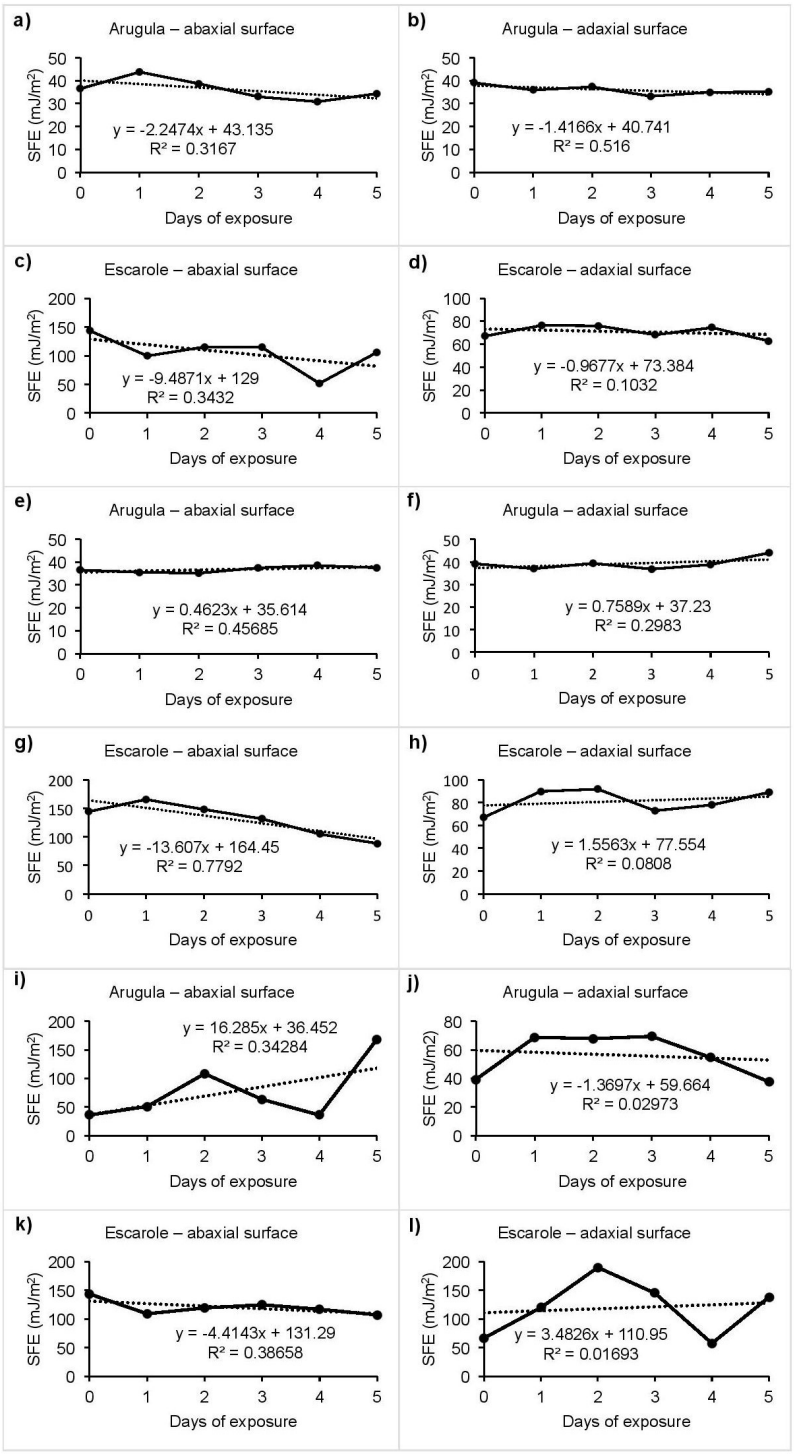

Figure 4.14: Foliar SFE values accompanied by trend lines for abaxial (a, c, e, g, i, k) and adaxial (b, d, f, h, j, l) foliar surfaces of arugula (a, b, e, f, e, j) and escarole (c, d, g, h, k, l) before the experimental period and following each day of treatment with 5 mg Pt NPs/L (a-d), 50 mg Pt NPs/L (e-h), and 500 mg Pt NPs/L (i-l). Estimations were made using acid-base theory applying contact angle values from droplets of ultrapure water, diiodomethane, and glycerol (n = 5 per liquid).

Graphical representations with trend lines depicting abaxial and adaxial foliar SFE (acid-base theory) in response to 5, 50, and 500 mg Pt NPs/L exposure for both plants are displayed in Fig. 4.14. These values are taken to represent the full impact of Pt NP exposure on SFE since a separate analysis with unexposed leaf samples showed the effect of aging on the abaxial and adaxial foliar SFE of both plants to be negligible (i.e., over a 10 day period, the difference was no greater than 4.11 mJ/m^2; Table 4.9). Contact angle values obtained throughout the foliar exposure period for arugula and escarole are available in Table 4.10 while full numerical SFE results are available in Appendix A. Comparing the two plants before the exposure period, arugula foliar surfaces had substantially lower SFE values (abaxial: 36.47 mJ/m^2; adaxial: 39.12 mJ/m^2; Fig. 4.15a) than the foliar surfaces of escarole (abaxial: 143.91 mJ/m^2; adaxial: 67.07 mJ/m^2; Fig. 4.15b). Although there was poor linearity of SFE with exposure to the Pt NP dispersion, efforts were still made to evaluate possible relationships between the two factors since, at least in the cases of the arugula abaxial and escarole adaxial surfaces (Fig. 4.14i and l, respectively) SFE changed noticeably with each day of exposure to 500 mg Pt NP/L dispersion. Overall, less change was evident in the case of 5 and 50 mg/L foliar exposures.

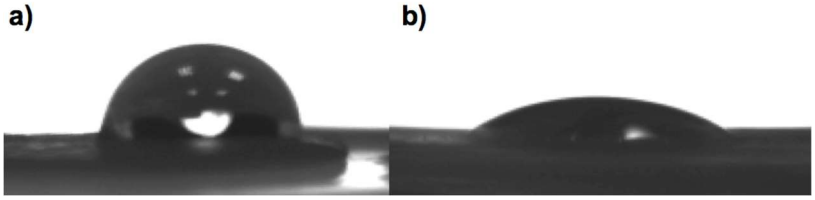

Figure 4.15: Characteristic images of water droplets on arugula (a) and escarole (b) obtained with an optical tensiometer.

Table 4.9: Contact angle values for ultrapure water (W), diiodomethane (DM), and glycerol (G) on unexposed abaxial and adaxial arugula and escarole foliar surfaces to examine the effect of aging on SFE (three-liquid acid-base theory method). Measurements were completed every other day over a 10 day period, starting from the day on which Pt NP exposure would begin. All data are `mean ± standard deviation (SD; n = 5 per liquid)`.

Plant	Surface	Day	θW(°)	θDM(°)	θG(°)	SFE
Arugula	Abaxial	0	95.87 ± 8.69	48.07 ± 4.81	85.71 ± 10.51	36.47
		2	92.15 ± 5.48	57.06 ± 8.68	88.21 ± 7.89	34.84
		4	92.67 ± 5.79	60.75 ± 12.46	85.83 ± 6.50	28.01
		6	91.13 ± 7.45	58.69 ± 5.22	87.07 ± 5.96	32.63
		8	94.36 ± 1.51	60.43 ± 5.08	90.75 ± 9.78	33.11
		10	93.52 ± 7.79	61.26 ± 8.54	91.86 ± 5.43	35.08
	Adaxial	0	107.48 ± 12.08	51.93 ± 8.39	81.94 ± 7.47	39.12
		2	98.29 ± 11.74	52.20 ± 3.18	94.22 ± 7.69	41.66
		4	95.62 ± 4.89	58.30 ± 6.22	91.86 ± 7.72	35.44
		6	94.96 ± 7.30	57.69 ± 5.76	90.04 ± 1.88	34.03
		8	98.27 ± 4.70	55.28 ± 2.63	92.97 ± 4.14	36.92
		10	95.62 ± 5.24	56.02 ± 5.07	93.62 ± 4.95	40.69
Escarole	Abaxial	0	44.68 ± 17.97	39.96 ± 4.42	77.93 ± 8.08	143.91

	2	44.78 ± 8.21	38.91 ± 3.54	78.68 ± 4.71	149.92
	4	43.40 ± 3.83	38.25 ± 4.60	76.36 ± 5.42	141.30
	6	43.92 ± 8.43	38.04 ± 4.44	76.85 ± 4.48	142.88
	8	43.80 ± 7.48	37.20 ± 3.66	76.62 ± 10.38	143.15
	10	45.34 ± 12.21	37.32 ± 5.05	77.82 ± 5.85	145.46
Adaxial	0	44.47 ± 8.31	49.30 ± 8.20	65.53 ± 11.75	67.07
	2	66.60 ± 4.15	56.97 ± 5.66	82.30 ± 7.81	68.81
	4	68.18 ± 12.44	55.74 ± 6.85	83.36 ± 4.00	70.60
	6	64.01 ± 7.06	61.61 ± 3.23	81.69 ± 3.21	65.92
	8	65.97 ± 8.18	52.10 ± 7.76	79.31 ± 5.66	66.08
	10	63.86 ± 4.62	51.37 ± 10.75	78.94 ± 4.18	71.18

Among 500 mg Pt NPs/L foliar exposed leaves, examination of the graph trend lines in Fig. 4.14i shows that the arugula abaxial foliar surface showed the greatest overall change in SFE from Pt NP exposure, displaying an overall increase of 81.4 mJ/m^2, or a more than two-fold increase over the exposure period. The adaxial surface of escarole showed a similar, but comparatively modest overall increase of 17.4 mJ/m^2 over the exposure period (Fig. 4.14l). Both the arugula adaxial and escarole abaxial foliar surfaces displayed a slight decreasing trend in SFE (overall decrease of 6.8 and 22.1 mJ/m^2 for arugula [Fig. 4.14j] and escarole [Fig. 4.14k], respectively). Statistical analysis to compare the abaxial and adaxial foliar surfaces of arugula and escarole over the course of the Pt NP exposure period showed that the abaxial surfaces of arugula and escarole (Fig. 4.14i and k, respectively) were not significantly different, whereas the adaxial surfaces of arugula and escarole (Fig. 4.14k and l, respectively) were significantly different (paired t-test, $n = 5$, $p < 0.05$).

Table 4.10: Contact angle values from ultrapure water (W), diiodomethane (DM), and glycerol (G) on abaxial and adaxial arugula and escarole foliar surfaces before and following each day of foliar exposure to 5, 50, and 500 mg Pt NPs/L dispersion. All data are mean ± SD ($n = 5$ per liquid).

Plant	Surface	Exposure, day	θW(°)	θDM(°)	θG(°)
Arugula	Abaxial	Control, 0	95.87 ± 8.69	48.07 ± 4.81	85.71 ± 10.51
		5 mg/L, 1	92.67 ± 6.91	48.91 ± 4.83	89.30 ± 12.04
		5 mg/L, 2	96.08 ± 6.60	49.46 ± 2.97	88.98 ± 12.04
		5 mg/L, 3	99.24 ± 2.49	60.77 ± 7.57	94.41 ± 10.72
		5 mg/L, 4	101.26 ± 3.74	55.92 ± 5.80	89.23 ± 1.72
		5 mg/L, 5	99.44 ± 1.54	54.28 ± 11.00	91.15 ± 14.72
		50 mg/L, 1	102.41 ± 4.88	48.62 ± 2.86	89.46 ± 1.49
		50 mg/L, 2	97.61 ± 3.88	47.48 ± 2.62	85.46 ± 5.56
		50 mg/L, 3	98.42 ± 3.09	49.88 ± 2.38	89.89 ± 1.03
		50 mg/L, 4	97.89 ± 5.33	49.57 ± 1.95	90.22 ± 0.83
		50 mg/L, 5	101.35 ± 11.88	49.81 ± 2.21	92.16 ± 2.64
		500 mg/L, 1	92.06 ± 19.62	51.67 ± 4.74	93.41 ± 11.35
		500 mg/L, 2	69.62 ± 13.79	42.83 ± 11.22	88.56 ± 6.34
		500 mg/L, 3	80.74 ± 6.91	36.92 ± 3.48	83.61 ± 8.49
		500 mg/L, 4	91.18 ± 5.45	59.42 ± 3.51	89.59 ± 3.84

		500 mg/L, 5	74.67 ± 9.98	34.96 ± 10.11	101.28 ± 31.40
Arugula	Adaxial	Control, 0	107.48 ± 12.09	51.93 ± 8.39	81.94 ± 7.47
		5 mg/L, 1	100.73 ± 3.07	49.13 ± 3.69	79.59 ± 3.09
		5 mg/L, 2	104.78 ± 9.94	53.53 ± 6.53	80.35 ± 2.38
		5 mg/L, 3	100.14 ± 2.48	52.19 ± 7.97	88.10 ± 17.61
		5 mg/L, 4	101.14 ± 3.37	50.48 ± 4.99	80.35 ± 1.46
		5 mg/L, 5	95.32 ± 7.42	47.64 ± 2.42	78.64 ± 1.51
		50 mg/L, 1	103.80 ± 8.18	47.12 ± 4.49	91.08 ± 0.62
		50 mg/L, 2	100.88 ± 2.77	40.78 ± 7.29	85.72 ± 5.41
		50 mg/L, 3	108.79 ± 9.22	45.95 ± 2.75	92.74 ± 0.78
		50 mg/L, 4	105.89 ± 8.15	43.36 ± 2.60	91.60 ± 3.59
		50 mg/L, 5	102.64 ± 6.76	43.04 ± 3.07	94.30 ± 1.47
		500 mg/L, 1	94.94 ± 7.84	38.39 ± 7.34	97.52 ± 3.69
		500 mg/L, 2	89.69 ± 11.68	54.24 ± 8.58	98.38 ± 6.43
		500 mg/L, 3	83.89 ± 10.32	36.39 ± 7.40	87.96 ± 7.79
		500 mg/L, 4	95.33 ± 13.17	63.85 ± 9.36	102.74 ± 7.50
		500 mg/L, 5	92.88 ± 18.63	61.04 ± 25.11	92.65 ± 15.31
Escarole	Abaxial	Control, 0	44.68 ± 17.97	39.96 ± 4.42	77.93 ± 8.08
		5 mg/L, 1	51.96 ± 11.28	37.82 ± 3.62	73.36 ± 3.08
		5 mg/L, 2	45.98 ± 7.90	43.76 ± 10.71	74.82 ± 1.36
		5 mg/L, 3	40.94 ± 7.28	38.51 ± 3.49	70.44 ± 7.43
		5 mg/L, 4	42.63 ± 8.75	36.96 ± 3.45	72.68 ± 2.11
		5 mg/L, 5	42.33 ± 5.36	43.16 ± 9.46	70.99 ± 2.08
		50 mg/L, 1	42.75 ± 6.01	38.26 ± 4.06	79.84 ± 2.72
		50 mg/L, 2	37.92 ± 4.97	46.08 ± 7.75	76.81± 3.63
		50 mg/L, 3	44.24 ± 8.66	49.81 ± 4.39	78.56 ± 3.23
		50 mg/L, 4	47.07 ± 8.50	43.08 ± 6.74	73.14 ± 12.84
		50 mg/L, 5	46.31 ± 11.71	50.41 ± 5.07	71.82 ± 12.29
		500 mg/L, 1	59.57 ± 11.15	48.03 ± 8.52	83.20 ± 5.57
		500 mg/L, 2	38.20 ± 8.97	52.51 ± 6.42	74.29 ± 5.62
		500 mg/L, 3	33.10 ± 5.10	39.41 ± 5.11	68.80 ± 7.40
		500 mg/L, 4	29.00 ± 7.75	48.40 ± 5.15	68.61 ± 11.91
		500 mg/L, 5	59.57 ± 11.15	48.03 ± 8.52	82.82 ± 5.11
Escarole	Adaxial	Control, 0	44.47 ± 8.31	49.30 ± 8.20	65.53 ± 11.75
		5 mg/L, 1	49.80 ± 2.65	44.99 ± 8.37	69.21 ± 6.41
		5 mg/L, 2	46.03 ± 8.54	41.15 ± 9.17	65.60 ± 5.75
		5 mg/L, 3	45.98 ± 8.05	48.99 ± 10.76	66.53 ± 8.60
		5 mg/L, 4	41.37 ± 5.79	43.25 ± 10.00	63.56 ± 5.31
		5 mg/L, 5	49.15 ± 2.87	42.57 ± 10.60	64.36 ± 7.67
		50 mg/L, 1	38.51 ± 2.58	52.82 ± 7.92	69.05 ± 7.98
		50 mg/L, 2	40.51 ± 6.21	41.82 ± 7.54	66.56 ± 6.92
		50 mg/L, 3	37.78 ± 4.41	50.87 ± 10.24	64.29 ± 5.91
		50 mg/L, 4	44.48 ± 7.35	48.58 ± 11.29	67.87 ± 7.46
		50 mg/L, 5	43.71 ± 10.85	50.29 ± 13.17	70.51 ± 5.49

500 mg/L, 1	48.06 ± 10.05	46.26 ± 3.05	77.60 ± 8.85
500 mg/L, 2	33.05 ± 6.31	49.51 ± 12.08	81.58 ± 5.34
500 mg/L, 3	44.47 ± 13.68	47.31 ± 4.62	80.07 ± 8.06
500 mg/L, 4	40.25 ± 13.71	54.04 ± 5.74	62.91 ± 12.31
500 mg/L, 5	58.83 ± 15.05	31.37 ± 5.52	83.61 ± 4.38

4.2.4 Pt Concentrations in Leaves and Roots to Assess Translocation

Numeric Pt concentration values from preliminary testing are shown in Table 4.11. Here, arugula plants were bolting and no longer edible when harvested after four weeks of Pt NP exposure (Fig. 4.16a). A comparison between the leaf and root Pt concentrations in arugula plants after one week (when the plants reached peak growth) versus four weeks after foliar exposure (50 mg Pt NPs/L) showed no statistical differences (Mann-Whitney test; $n = 3$, five plants per replicate, $p < 0.05$; Table 4.11). A similar comparison with root-exposed arugula plants, however, showed significantly higher root Pt concentrations and significantly lower leaf Pt concentrations among plants harvested four weeks after exposure (Mann-Whitney test; $n = 2$; five plants per replicate, $p < 0.05$; Table 4.11). Since the main focus of this study was on foliar exposure, where no significant differences in arugula leaf and root Pt concentrations were detected with exposure time, the plants were subsequently harvested after one week of exposure to reflect their lifecycle and appearance when normally consumed (Fig. 4.16b).

Figure 4.16: Photographs of arugula plants four weeks following exposure to Pt NPs (a) in comparison with arugula plants one week following exposure to Pt NPs (b).

Table 4.11: Preliminary results: arugula leaf and root Pt concentrations as a function of exposure period (four weeks and one week). Unless otherwise notated, data are mean ± SE ($n = 3$, 5 plants per replicate). *Data are mean ± SE ($n = 2$, 5 plants per replicate). †Significant difference between like exposure groups on the basis of exposure time according to the Mann-Whitney test ($p < 0.05$).

Exposure period (weeks)	Exposure	Pt NP treatment	Leaf Pt concentration (ng/g DW)	Root Pt concentration (ng/g DW)
4	Control	0 mg/L	1.99 ± 0.61*	1.88 ± 0.62*
	Root	50 mg/L (20 mL)	22.7 ± 1.2*†	64.3 ± 56.0*†
	Foliar	50 mg/L	147,000 ± 46,600	8.05 ± 2.83

1	Control	0 mg/L	2.59 ± 1.05	1.92 ± 0.794
	Root	50 mg/L (20 mL)	175 ± 56.2†	9.12 ± 1.01†
	Foliar	50 mg/L	123,000 ± 39,700	17.4 ± 11.5

The Pt concentrations measured in the leaves and roots, along with the average fractions (%) of total Pt detected in leaf and root segments of the treated plants are presented in Fig. 4.17a and b, respectively). Numeric Pt concentration values and total, leaf, and root Pt quantities are provided in Tables 4.12 and 4.13, respectively. The repeatability (presented in Table 4.14) expressed as the % relative SD (%RSD) ranged from 12.8-49.4% for control leaves and 22.2-86.6% for control roots. For exposed leaves (all exposures), the %RSD ranged from 1.2-63.1% for leaves and 0.4-160.8% for roots. These values indicate significant sample heterogeneity within individual replicates, particularly for root samples which were cut into pieces rather than milled. Control leaves and roots from both plants contained extremely low levels of Pt (mean values of <3.5 ng/g DW); therefore it could be assumed that Pt detected in samples from the treatment groups originated from the experimental exposures.

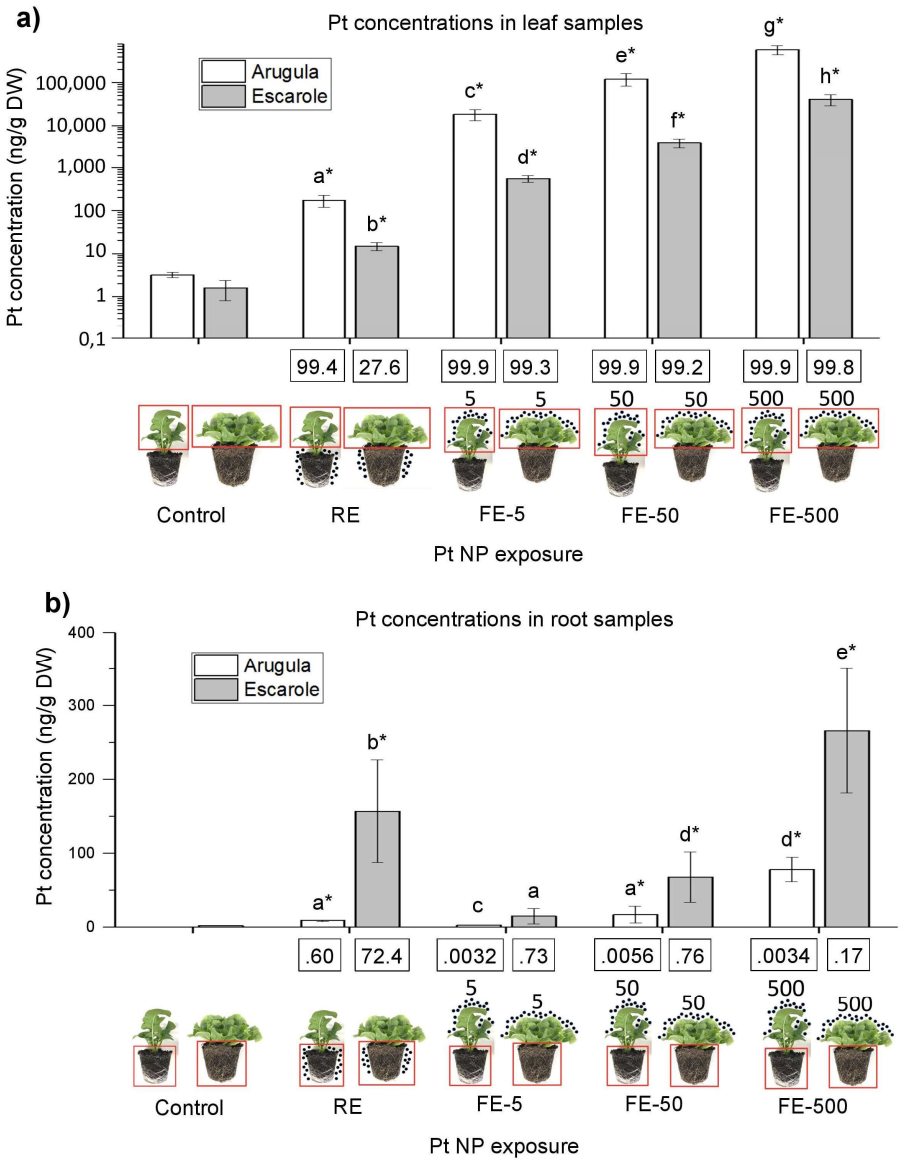

Figure 4.17: Pt concentrations of arugula and escarole leavces (a) and roots (b) after Pt NP foliar exposure (FE) or root exposure (RE). Significant mean differences between exposure groups are indicated by different letters, while letters in common indicate a lack of difference. An asterisk indicates a statistical difference between an exposure group and the corresponding control group ($p < 0.05$). Images denote plant type (arugula: left; escarole: right), analyzed plant segment (red box), and the Pt NP exposure (black dots on roots or leaves with concentration of foliar exposure in mg/L). Boxed numbers above sample images indicate the mean fraction of total Pt (%) in the sample calculated from each replicate of the exposure. DW = dry weight.

Arugula leaves consistently contained statistically higher Pt concentrations than escarole leaves at all Pt NP exposures (approximately 33, 31, and 14 times higher, on average, for the 5, 50, and 500 mg Pt NPs/L foliar exposures, respectively, and 12 times higher, on average, for the root exposure). This indicated both a higher capacity to retain foliar applications of Pt NPs and to internalize and translocate root-applied Pt NPs from roots to leaves (Fig. 4.15a). In the case of foliar applications, the low SFE of the arugula

leaves meant that applied droplets of Pt NP dispersion remained attached to the leaf surface without spreading out and dripping towards the bottom of the leaves as was the case with escarole. The amount of Pt detected in water samples from the washing procedure was negligible (<0.15 ng/mL), showing that Pt NPs were not removed from either plant by the washing procedure used in this study.

Table 4.12: Pt concentrations in arugula and escarole leaf and root samples. All data are mean ± SE (n = 3, 5 plants per replicate).

Plant	Exposure	Pt NP treatment	Leaf Pt concentration (ng/g DW)	Root Pt concentration (ng/g DW)
Arugula	Control	0 mg/L	2.59 ± 1.05	1.92 ± 0.794
	Root	50 mg/L (20 mL)	175 ± 56.2	9.12 ± 1.01
	Foliar	5 mg/L	18,400 ± 5,120	2.37 ± 0.0656
		50 mg/L	123,000 ± 39,700	17.4 ± 11.5
		500 mg/L	588,000 ± 143,000	78.2 ± 16.5
Escarole	Control	0 mg/L	2.19 ± 0.883	2.16 ± 0.858
	Root	50 mg/L (20 mL)	14.7 ± 2.97	157 ±69.6
	Foliar	5 mg/L	562 ± 100	15.0 ± 10.6
		50 mg/L	3,940 ± 903	67.8 ± 34.1
		500 mg/L	410,000 ± 11,600	266 ± 84.6

Root Pt concentrations increased in a linear manner with increasing concentration of the foliar Pt NP application, reaching statistical increases from controls at 50 and 500 mg Pt NPs/L. At 5 mg Pt NPs/L foliar exposure, only escarole roots contained statistically elevated Pt concentrations relative to the controls. Among root samples, escarole consistently accumulated higher Pt concentrations than arugula (approximately 17, 6, 4, and 3 times higher, on average, for the root and 5, 50, and 500 mg Pt NPs/L foliar exposures, respectively; Fig. 4.15b and Table 4.12).

Table 4.13: Total quantities of Pt in whole arugula and escarole plants (leaves and roots), and in leaves and roots. All data represent means from triplicate measurements for each replicate (n = 3, 5 plants per replicate). A = arugula; E = escarole; F = foliar exposure; R = root exposure. *Although it was not possible to remove all root tissue from the soil media, care was taken to remove as much as possible.

Plant, exposure pathway (Pt NP concentration [mg/L], replicate)	Total Pt in whole plant (ng)	Pt in leaves (ng)	Pt in roots* (ng)
A, F (5, 1)	60,102	60,100	2.43
A, F (5, 2)	64,102	64,100	2.30
A, F (5, 3)	75,502	75,500	1.52
A, F (50, 1)	303,035	303,000	35.4
A, F (50, 2)	712,008	712,000	8.29

A, F (50, 3)	567,022	567,000	22.0
A, F (500, 1)	1,980,036	1,980,000	36.1
A, F (500, 2)	1,730,044	1,730,000	43.9
A, F (500, 3)	1,250,072	1,250,000	72.3
A, R (50, 1)	1,317	1,310	6.99
A, R (50, 2)	1,136	1,130	5.75
A, R (50, 3)	932	924	7.75
E, F (5, 1)	3,382	3,350	31.9
E, F (5, 2)	3,910	3,870	40.1
E, F (5, 3)	2,726	2,720	6.07
E, F (50, 1)	24,408	24,300	108
E, F (50, 2)	13,620	13,500	120
E, F (50, 3)	22,008	21,800	208
E, F (500, 1)	220,303	220,000	303
E, F (500, 2)	206,361	206,000	361
E, F (500, 3)	224,460	224,000	460
E, R (50, 1)	399	37.9	361
E, R (50, 2)	444	76.2	368
E, R (50, 3)	258	103	155

Because the total fraction of translocated Pt from leaves to roots was extremely low for both plants (<1%), an attempt was made to assess whether Pt internalization and translocation from leaves to roots might have occurred only in dissolved form by comparing the average fractions of total Pt measured in the roots (Fig. 4.15b; i.e., translocated Pt) with the corresponding fractions of dissolved Pt measured in samples prepared by ultracentrifugation (Table 4.6). Size is considered to be the main determinant of NP passage into plant tissues [182]. Therefore, there are two potential uptake mechanisms. Assuming that the total fraction of dissolved Pt would be internalized and translocated by the leaf tissue due to the lack of a size exclusion barrier over the entire plant surface, any fraction of translocated Pt above the dissolved fraction might be further assumed to have been internalized and translocated in the NP form. Since the average fraction of translocated Pt in escarole was many orders of magnitude higher than the fractions of dissolved Pt, this could indicate that the escarole plants may have been able to internalize and translocate the Pt as NPs. It is also possible that the escarole foliar surface environment (e.g., temperature, humidity, and microbial communities) is more conducive to Pt NP dissolution [146], and that dissolved Pt uptake generates a higher rate of dissolution on the foliar surface [217].

By contrast, the average fractions of total Pt measured in the roots of foliar-exposed arugula plants (Fig. 4.15b) were several orders of magnitude lower than the corresponding fractions of dissolved Pt (Table 4.6). In the absence of suitable methods to accurately locate and characterize elements present at such low concentrations in plant tissues, it is therefore not possible to rule out the possibility that Pt was internalized and translocated to roots only in dissolved form. These findings therefore illustrate different surface responses to foliar Pt NP exposure between the two plants.

Table 4.14: Repeatability (expressed as SD and %RSD) of Pt measurements in arugula and escarole leaf and root samples. For all data n = 1, 5 plants per replicate.

Plant	Exposure	Pt NP treatment	Replicate	Repeatability of leaf samples (ng/mL); %RSD in parentheses	Repeatability of root samples (ng/mL); %RSD in parentheses
Arugula	Control	0 mg/L	--	0.42 (12.8%)	0.37 (86.6%)
	Root	50 mg/L (20 mL)	1	49 (20.6%)	2.3 (22.2%)
			2	100 (63.1%)	3.9 (43.1%)
			3	30 (23.4%)	0.10 (1.3%)
	Foliar	5 mg/L	1	2,500 (17.6%)	0.01 (0.4%)
			2	2,600 (15.4%)	0.01 (0.4%)
			3	1,600 (6.6%)	1.7 (72.1%)
		50 mg/L	1	13,000 (15.4%)	28 (160.8%)
			2	13,000 (10.4%)	8.6 (145.5%)
			3	17,000 (10.3%)	4.3 (14.8%)
		500 mg/L	1	57,000 (8.3%)	23 (38.8%)
			2	68,000 (10.4%)	21 (25.3%)
			3	110,000 (25.3%)	30 (32.3%)
Escarole	Control	0 mg/L	--	0.79 (49.4%)	0.44 (22.2%)
	Root	50 mg/L (20 mL)	1	4.4 (39.1%)	62 (35.2%)
			2	6.4 (37.6%)	68 (31.8%)
			3	1.0 (6.6%)	38 (48.7%)
	Foliar	5 mg/L	1	7.2 (1.2%)	3.6 (19.7%)
			2	11 (1.7%)	33 (140.1%)
			3	69 (15.3%)	0.42 (13.4%)
		50 mg/L	1	1,100 (23.1%)	24 (53.8%)
			2	91 (2.9%)	25 (49.1%)
			3	400 (9.4%)	23 (21.4%)
		500 mg/L	1	7,100 (14.2%)	86 (46.8%)
			2	800 (2.9%)	170 (48.6%)
			3	5,800 (12.9%)	280 (107.7%)

The root-exposed leaf samples from both plants showed very high percentages of Pt NP uptake and translocation from roots to leaves (Fig. 4.15a and Table 4.12). In arugula, nearly the entire amount of Pt was present in the leaves (99.4%) whereas in escarole, the percentage of Pt in leaves was markedly lower (27.6%). Had the arugula plants been harvested after four weeks of exposure, as was done in the initial trial experiment, we would have expected to measure similar leaf and root Pt concentrations to those in escarole (Table 4.11). The soil pH of Pt NP exposed plants at harvest was not statistically different from that of the controls (Table 4.15).

Table 4.15: Soil pH values at harvest. All data are mean ± SD (n = 3).

Plant	Exposure	Pt NP treatment	pH
Arugula	Control	0 mg/L	6.86 ± 0.12

	Root	50 mg/L (20 mL)	6.98 ± 0.32
	Foliar	5 mg/L	6.91 ± 0.19
		50 mg/L	6.74 ± 0.05
		500 mg/L	6.91 ± 0.10
Escarole	Control	0 mg/L	6.94 ± 0.24
	Root	50 mg/L (20 mL)	6.89 ± 0.02
	Foliar	5 mg/L	6.99 ± 0.17
		50 mg/L	6.83 ± 0.07
		500 mg/L	6.98 ± 0.22

4.2.5 Discussion

The uptake and translocation of Pt from leaves to roots and from roots to leaves was successfully confirmed in two plant species: arugula and escarole. The two species exhibited different responses in terms of Pt NP surface adsorption and Pt translocation from leaves to roots. This could partly be related to the different SFE between the two plant species [218].

Table 4.16: Proportion of open stomata (%) on abaxial and adaxial arugula surfaces with Pt NP foliar exposure (control, 50, and 500 mg/L). All data are mean ± SD ($n = 10$). *Significant differences from the control according to the Mann-Whitney test ($p < 0.05$). **The boundaries between areas where droplets of Pt NP dispersion were applied and areas where droplets were not applied is very clear since the droplets did not spread out over the arugula leaf surfaces.

		Proportion of open stomata (%)	
Foliar exposure (mg Pt NPs/L)	Areas with many visible Pt NPs?**	Abaxial surface	Adaxial surface
Control	No	6.35 ± 11.2	60.6 ± 16.0
50	Yes	0*	0*
	No	34.2 ± 16.7*	43.0 ± 13.9*
500	Yes	0*	0*
	No	0*	0*

Among arugula leaves, which have low SFE, a higher amount of material was adsorbed onto the leaf surfaces (14-33 times higher Pt concentrations were detected than in escarole leaves), the stomata were closed, and less Pt was detected in roots when compared to escarole. The closed stomata on arugula leaves were likely the result of shading effects, which occur when the amount of light reaching the surface is insufficient for photosynthesis to occur [219]. Although this was not tested by removing Pt NPs to examine whether the stomata would reopen, the finding of significantly lower arugula leaf mass after foliar exposure to 500 mg Pt NPs/L in comparison to the other arugula groups is consistent with a decreased ability to synthesize the carbohydrates needed for optimal growth. Additional examination of the arugula leaf samples foliar-exposed to 50 mg Pt NPs/L by SEM-EDX showed that while the stomata were closed in areas with concentrated Pt NPs, open stomata were still visible in areas of the leaf where Pt NPs were not present. A comparison of the proportion of open stomata in areas where Pt NPs were not present on 5o mg Pt NPs/L foliar exposed leaves with the proportion of open stomata on unexposed leaves

showed a significant decrease (Mann-Whitney test, $n = 10$, $p < 0.05$; Table 4.16). This suggests a partial shading effect at 50 mg Pt NPs/L foliar exposure and the existence of a full shading effect at 500 mg Pt NPs/L foliar exposure.

In escarole leaves, which have high SFE, less Pt was adsorbed onto the surfaces, the stomata remained open, and higher Pt concentrations were measured in roots. The high SFE could directly enhance Pt NP internalization through the formation of water film connections between the inner and outer portions of the leaves, which has been associated with an increased capacity for particle uptake by stomata [176]. This relationship between the cuticular structure (i.e., the relative proportions of the cuticular constituents and the chemical bonding between them), foliar SFE, and water film formation aligns with the cuticle's major physiological role in regulating water balance [154]. Although foliar SFE may change with repeated particle exposure, our findings were in agreement with similar studies [220], [221] which demonstrated inconsistent changes with regards to whether it increased or decreased. There were no statistical differences in leaf mass between the different escarole groups.

In our study, less than 1% of the total Pt was detected in the roots of foliar-exposed plants. In arugula, we have explained that the fraction of translocated Pt from leaves to roots could originate from dissolved Pt NPs. The average dissolution of Pt NPs in ultrapure water was several orders of magnitude greater than the average percentage of Pt translocated to roots by arugula. Consequently, the dissolved fraction of Pt is sufficient to explain the amount present in roots. In escarole, the amount of Pt detected in roots may not have been due entirely to dissolved Pt NPs, because the fraction of translocated Pt was many orders of magnitude higher than the potentially dissolved Pt from the Pt NP dispersions. However, the escarole foliar surface environment and the rate of uptake of dissolved Pt may have favored the dissolution of Pt NPs relative to arugula [146], [217]. In some cases, foliar uptake has been attributed to the interactions between the particle and leaf surface, resulting in enhanced bioavailability through the formation of organic coatings [178], [180] and secondary species [140]. Within short time periods (60 days), elemental Pt is highly unreactive even in its particulate form [215]; therefore it is unlikely that higher uptake by escarole could be explained by processes other than dissolution. An attempt to locate Pt NPs within arugula and escarole leaves using SEM (with leaf cross sections) and focused ion beam-SEM yielded no signs of Pt uptake in its particulate form. Here, analysis of xylem and/or phloem sap by electron microscopy and ICP-MS could have provided better insight into the form of Pt and its uptake mechanisms by the foliar surfaces. In either case, the finding of increased Pt translocation, whether as NPs or in its dissolved form, is in line with the high SFE of the escarole leaves. It has been previously reported that the foliar uptake of NPs occurs mainly through a hydrophilic pathway consisting of stomata [146], [176], [178], [180], [185]. Internalized NPs may reach the phloem, enabling transport to roots [222]. Wang et al. [223] showed that 1.23% of foliar-applied, non-dissolvable TiO_2 NPs were translocated to roots in watermelon. This is in agreement with our findings in the case of escarole, but not for arugula.

Platinum NP uptake and translocation from roots to leaves was also confirmed. Root to leaf NP uptake and translocation occurs when NPs are taken up with water and nutrients through the xylem via passage through the epidermis, cortex, Casparian strip (via the symplasmic pathway), and stele. Plant transpiration provides the driving force for their movement from roots to stems and leaves [157], [224]. Because the plants were cultivated in soil rather than hydroponics systems, our results provide a realistic root exposure scenario. Although the fraction of root-to-leaf translocation was much higher than that of leaf-to-root translocation (nearly 30,000 times higher for arugula and 160 times higher for escarole), the soil matrix provides a barrier to NP exposure which is absent for above-ground plant segments.

This study showed that Pt NPs were not removed from the plants when washed only with water, indicating that they are most likely to remain adhered to and within above-ground plant segments under this washing regime. Insignificant NP removal from foliar surfaces has been frequently observed, including in the case of maize leaf exposure to CeO_2 NPs [225], lettuce leaf exposure to Ag NPs [180], and grapevine leaf exposure to poly(lactic-co-glycolic) acid NPs [226]. During industrial processing or home preparation, produce may be exposed to chlorine [227] or other additives in wash water, which could potentially affect NP attachment/detachment differently than water alone. For example, Hong et al. [181] found enhanced removal of CeO_2 NPs from cucumber leaves after washing with 10 mM $CaCl_2$ solution (81.0 ± 1.0% removal) in comparison to washing only with water (73.0 ± 1.0% removal). However, to the best of our knowledge, there have been no studies focused exclusively on investigating strategies for NP removal from plant surfaces.

Chapter 3

Conclusions

In this dissertation, inadvertent food contamination with NPs originating from atmospheric deposition was examined in the context of incense-emitted NP dynamics and decay mechanisms from air and in terms of arugula and escarole foliar responses to Pt NP exposure. The first case serves as a model for understanding food exposure to NPs during indoor preparation (incense may be burned to remove cooking odors), while the second case illustrates the potential effects of outdoor air pollution on crop plants, since Pt NPs are emitted from catalytic converters along roadways.

In the first part of this work, new results were presented on incense-emitted NP concentrations and distributions, which provide a more accurate indication of potential harm from this activity than mass-based measurements alone. This is due to the fact that the size distribution of emitted particles dictates the length of time that air pollution persists; nucleation mode particles (up to 100 nm in size) only exist for ~15 minutes before coagulating with accumulation mode particles (100-1,000 nm in size), which have inefficient removal mechanisms and therefore remain airborne for significantly longer periods of time. Nanoparticles are also more likely to bind with other contaminants present in incense emissions than larger particles. Since incense is a significant emitter of NPs, we therefore hypothesized that: 1) their emissions would remain airborne for significant periods of time (i.e., hours) following the incense burning period due to a high proportion of accumulation mode particles and that 2) we would find distance-dependent effects in which the particle number concentrations would decrease with increasing distance from the measurement inlet due to coagulation between nucleation mode particles as they traveled from the incense towards the measurement inlet.

Using a scanning mobility particle sizer (SMPS) to track the NP number concentrations and distribution in air and a Dekati low pressure cascade impactor (DLPI) to measure the mass-based particle distribution in air by size, we were able to prove both hypotheses correct. The results showed that the maximum total particle concentration (TPC) at the end of the burning period was up to 30-fold higher than that of the initial background levels and that it remained up to six-fold higher 100 minutes after the conclusion of the burning period. Throughout the post-burning period, the TPC exhibited biexponential decay with two lifetimes of several tens of minutes for nucleation-mode particles and >100 minutes for accumulation mode particles. In other words, the extended periods of air pollution following incense burning aligned with the finding that accumulation mode particles (in terms of both concentration and mass) were predominant among the emitted particles. Slight distance dependent effects were also identified, with the TPC being higher with decreasing distance to the measurement inlet due to a higher proportion of nucleation mode particles.

In the second part of this work, the role of foliar surface free energy (SFE) on NP adhesion and uptake and translocation by plants was assessed for the first time. Here, arugula (low SFE) and escarole (high SFE) exposure to Pt NPs provided a good model for inadvertent plant exposure to NPs deposited from air because both plants are commonly grown and consumed, while Pt NPs are emitted from catalytic converters along roadways. Surface free energy is a quantitative measure of the polar and dispersive forces that determines surface hydrophobicity/hydrophilicity. Since a higher SFE (i.e., hydrophilicity) results in a higher contact area between droplets of the applied dispersion and leaf surfaces, we hypothesized that: 1) a higher foliar SFE would be associated with increased Pt NP adhesion to leaves and that 2) a higher foliar SFE would lead to increased internalization and translocation of Pt NPs to roots. We also hypothesized that: 3) the proportion of Pt NPs translocated from roots to leaves would exceed the proportion of Pt NPs translocated from leaves to roots because roots have a very high surface area and larger size exclusion limits in comparison to leaves, and 4) the foliar SFE would change in response to the Pt NP applications because it is partly determined by micro- and nano-surface roughness.

Three of the hypotheses related to the second part of the work were proven correct, while one was shown to be false. The results of Pt quantification in leaves and roots with inductively coupled plasma-mass spectrometry (ICP-MS) showed that the first hypothesis was incorrect: arugula leaves (low SFE) contained statistically higher Pt concentrations than escarole leaves at all Pt NP exposures (approximately 33, 31, and 14 times higher, on average, for the 5, 50, and 500 mg Pt NPs/L foliar exposures, respectively). This was due to the fact that the droplets of dispersion remained attached to the leaf surface without spreading out and dripping towards the bottom of the leaves, as was the case with escarole. On the other hand, the results of Pt quantification in the roots of foliar-exposed plants showed that statistically greater amounts of Pt were translocated from leaves to roots in escarole relative to arugula, proving the second hypothesis correct. In addition to the fact that a higher SFE may promote Pt NP uptake and translocation through the development of water film connections between the inner and outer portions of the leaf, results from scanning electron microscopy (SEM; 500 mg Pt NPs/L) showed a much higher degree of Pt NP aggregation/agglomeration on arugula relative to escarole, in addition to complete stomata closure from likely shading effects on arugula. Nonetheless, a far higher proportion of Pt NPs were translocated from roots to leaves (99% and 28% for arugula and escarole, respectively) than from leaves to roots (<1% for both plants), proving the third hypothesis correct. Surface free energy calculations using acid-base theory showed the fourth hypothesis to be correct as well: the SFE changed in response to Pt NP exposure, however it did not change in a consistent, predictable manner.

These results indicate that inadvertent food exposures to NPs in indoor and outdoor environments deserve greater attention. As shown in the first part of the work, NPs emitted into air can persist for hours of time under conditions of low ventilation, leaving food surfaces vulnerable to NP deposition. In the second part of this work, we have shown that foliar exposure to Pt NPs leads to significant adhesion and contamination of arugula and escarole leaves, and that low SFE significantly increases the extent of Pt NP retention. In light of other reports showing the disproportionate influence of urban and industrial air pollution on above-ground plant contamination, these factors further suggest the need to include air quality as a factor in discussions of food safety and urban gardening. Since NPs are not removed by washing only with water, strategies to limit human consumption of metallic NPs from atmospheric deposits should focus on the removal of outer peels and leaves and implementation of physical barriers to prevent contact.

Appendix A

Numerical and Surface Free Energy Solubility Parameter Values

Table 5.1: Complete numerical SFE and solubility parameter values for abaxial and adaxial arugula and escarole foliar surfaces before and following each day of foliar exposure to 5, 50, or 500 mg Pt NPs/L dispersion. All SFE (γ_s), solubility parameter (δ), and dispersive, non-dispersive, electron-donor, and electron-acceptor force component values (γ_s^d,) *Significant differences from the control according to the Mann-Whitney test ($p < 0.05$). **The boundaries between areas where droplets of Pt NP dispersion were applied and areas where droplets were not applied is very clear since the droplets did not spread out over the arugula leaf surfaces.

Method	Test liquids	Exposure (mg/L), day	$\gamma_s^d 1$ (mJ m^{-2})	$\gamma_s^d 2$ (mJ m^{-2})	γ_s^+ (mJ m^{-2})	γ_s^- (mJ m^{-2})	$\gamma_s^{nd} 1$ (mJ m^{-2})	$\gamma_s^{nd} 2$ (mJ m^{-2})	γ_s (mJ m^{-2})	δ (MJ$^{1/2}$ m$^{-3/2}$)
Arugula abaxial surface										
GM	W, G	Control, 0	17.07				3.51		20.58	11.99
		5, 1	6.37				10.30		16.67	10.24
		5, 2	11.26				5.58		16.85	10.32
		5, 3	7.20				6.37		13.57	8.77
		5, 4	19.56				1.47		21.01	12.18
		5, 5	12.57				3.78		16.34	10.09
		50, 1	21.29				0.97		22.26	12.72
		50, 2	20.94				2.05		22.98	13.02
		50, 3	13.25				3.89		17.13	10.45
		50, 4	11.84				4.61		16.45	10.14
		50, 5	13.74				2.79		16.53	10.17
		500, 1	1.84				16.22		18.06	10.87
		500, 2	5.23				70.00		75.23	31.70
		500, 3	1.76				25.50		27.26	14.80
		500, 4	4.50				12.99		17.50	10.61
		500, 5	19.42				86.97		106.39	41.10

W, DM	Control, 0	35.02	0.50	35.52	18.05
	5, 1	33.76	1.13	34.88	17.81
	5, 2	34.18	0.54	34.72	17.75
	5, 3	27.42	0.73	28.15	15.17
	5, 4	31.07	0.21	31.28	16.41
	5, 5	31.77	0.33	32.10	16.73
	50, 1	36.17	0.00	36.17	18.30
	50, 2	35.07	0.30	35.37	18.00
	50, 3	34.44	0.26	34.70	17.74
	50, 4	34.52	0.31	34.83	17.79
	50, 5	35.15	0.05	35.19	17.93
	500, 1	31.86	1.50	33.36	17.22
	500, 2	32.32	9.96	42.27	20.57
	500, 3	38.05	3.55	41.60	20.32
	500, 4	26.68	2.61	29.29	15.62
	500, 5	37.65	5.92	43.57	21.04
G, DM	Control, 0	37.10	0.04	37.14	18.67
	5, 1	37.55	0.36	37.91	18.96
	5, 2	37.05	0.27	37.33	18.74
	5, 3	30.07	0.19	30.26	16.01
	5, 4	32.33	0.02	32.34	16.83
	5, 5	34.10	0.23	34.33	17.60
	50, 1	37.81	0.41	38.22	19.07
	50, 2	36.63	0.02	36.64	18.48
	50, 3	37.02	0.37	37.39	18.76
	50, 4	37.34	0.45	37.80	18.91
	50, 5	37.74	0.82	38.56	19.20

		500, 1	36.72		0.89	37.61	18.84
		500, 2	41.69		0.76	42.44	20.63
		500, 3	44.05		0.31	44.36	21.33
		500, 4	29.81		0.01	29.81	15.83
		500, 5	51.22		8.36	59.58	26.61
HM	W, G	Control, 0	14.89	-23.02	-45.17	23.67	13.32
		5, 1	6.89	-22.85	-45.86	22.78	12.94
		5, 2	10.70	-22.88	-45.78	21.77	12.50
		5, 3	7.51	-22.61	-45.96	19.48	11.50
		5, 4	17.51	-22.87	-45.80	22.97	13.02
		5, 5	11.89	-22.78	-46.21	20.71	12.05
		50, 1	19.14	-22.87	-45.84	23.60	13.29
		50, 2	17.86	-23.03	-45.12	24.63	13.72
		50, 3	12.33	-22.84	-45.95	21.34	12.32
		50, 4	11.22	-23.07	-46.02	21.13	12.23
		50, 5	13.01	-22.84	-46.43	20.42	11.92
		500, 1	2.46	-22.82	-46.75	24.39	13.62
		500, 2	-4.28	-22.73	-45.83	67.80	29.32
		500, 3	3.49	-22.65	-44.91	31.59	16.53
		500, 4	5.35	-22.84	-45.93	23.77	13.36
		500, 5	-9.14	-22.19	-48.96	152.35	53.81
	W, DM	Control, 0	33.86	101.68	-1.56	37.14	18.67
		5, 1	33.10	149.24	-1.62	37.69	18.87
		5, 2	33.19	99.59	-1.56	36.51	18.43
		5, 3	27.81	74.51	-1.54	31.07	16.33
		5, 4	30.70	62.23	-1.46	32.67	16.96
		5, 5	31.22	72.58	-1.50	33.71	17.36

	50, 1	35.34	55.34	-1.32		36.16	18.30
	50, 2	33.86	85.31	-1.53		36.52	18.43
	50, 3	33.35	79.13	-1.51		35.81	18.17
	50, 4	33.41	83.14	-1.52		36.05	18.26
	50, 5	34.15	60.93	-1.40		35.50	18.05
	500, 1	31.70	162.98	-1.63		36.79	18.53
	500, 2	35.00	-126.35	-1.75		49.20	23.05
	500, 3	37.89	-457.08	-1.70		46.40	22.06
	500, 4	27.86	187.51	-1.63		34.15	17.53
	500, 5	38.50	-180.11	-1.73		49.57	23.18
G, DM	Control, 0	X	X	X	X	X	X
	5, 1	X	X	X	X	X	X
	5, 2	X	X	X	X	X	X
	5, 3	X	X	X	X	X	X
	5, 4	X	X	X	X	X	X
	5, 5	X	X	X	X	X	X
	50, 1	X	X	X	X	X	X
	50, 2	X	X	X	X	X	X
	50, 3	X	X	X	X	X	X
	50, 4	X	X	X	X	X	X
	50, 5	X	X	X	X	X	X
	500, 1	X	X	X	X	X	X
	500, 2	X	X	X	X	X	X
	500, 3	X	X	X	X	X	X
	500, 4	X	X	X	X	X	X
	500, 5	X	X	X	X	X	X

3L	W, DM, G	Control, 0	32.82		0.79	4.25			36.47	18.42
		5, 1	30.57		3.36	12.91			43.73	21.10
		5, 2	31.38		1.93	7.04			38.74	19.27
		5, 3	25.08		1.95	7.94			32.95	17.07
		5, 4	29.39		0.29	1.75			30.81	16.23
		5, 5	29.32		1.36	4.78			34.43	17.64
		50, 1	33.61		0.75	1.36			35.62	18.09
		50, 2	33.12		0.40	2.45			35.10	17.89
		50, 3	31.64		1.66	5.02			37.41	18.77
		50, 4	31.56		2.02	5.97			50.76	19.18
		50, 5	32.01		1.97	3.85			108.35	18.81
		500, 1	28.05		6.23	20.69			63.23	23.60
		500, 2	27.06		19.16	86.22			35.93	41.67
		500, 3	33.93		6.85	31.35			168.33	27.82
		500, 4	24.66		2.08	15.28				18.21
		500, 5	28.75		42.65	114.20				57.99
Method	Test liquids	Exposure (mg/L), day	$\gamma_s^d 1$ (mJ m^{-2})	$\gamma_s^d 2$ (mJ m^{-2})	γ_s^+ (mJ m^{-2})	γ_s^- (mJ m^{-2})	$\gamma_s^{nd} 1$ (mJ m^{-2})	$\gamma_s^{nd} 2$ (mJ m^{-2})	γ_s (mJ m^{-2})	δ (MJ$^{1/2}$ m$^{-3/2}$)
					Arugula adaxial surface					
GM	W, G	Control, 0	57.47				1.93		59.41	26.55
		5, 1	45.15				0.06		45.21	21.63
		5, 2	54.81				1.09		55.90	25.37
		5, 3	19.93				1.64		21.57	12.42
		5, 4	43.83				0.05		43.87	21.15
		5, 5	33.28				0.73		34.01	17.47

	50, 1	20.30	0.87	21.18	12.25
	50, 2	27.28	0.52	27.80	15.02
	50, 3	26.48	0.01	26.49	14.49
	50, 4	23.24	0.30	23.55	13.26
	50, 5	11.88	2.99	14.87	9.40
	500, 1	0.93	16.23	17.16	10.46
	500, 2	0.17	29.08	29.25	15.61
	500, 3	0.86	25.35	26.21	14.37
	500, 4	0.06	22.88	22.94	13.01
	500, 5	2.99	13.77	16.76	10.28
W, DM	Control, 0	35.11	0.09	35.20	17.93
	5, 1	35.45	0.07	35.51	18.05
	5, 2	33.43	0.00	33.44	17.25
	5, 3	33.31	0.18	33.49	17.27
	5, 4	34.66	0.07	34.73	17.75
	5, 5	35.17	0.56	35.73	18.13
	50, 1	37.46	0.01	37.48	18.79
	50, 2	40.75	0.00	40.75	20.01
	50, 3	39.38	0.42	39.80	19.66
	50, 4	40.37s	0.20	40.57	19.95
	50, 5	39.79	0.02	39.81	19.67
	500, 1	40.69	0.24	40.93	20.08
	500, 2	29.70	2.44	32.14	16.75
	500, 3	39.09	2.41	41.50	20.29
	500, 4	24.64	1.90	26.54	14.51
	500, 5	25.97	2.28	28.25	15.20
G, DM	Control, 0	33.23	0.28	33.51	17.28

		5, 1	34.57		0.41		34.98	17.85
		5, 2	31.64		0.70		32.34	16.83
		5, 3	34.78		0.05		34.84	17.79
		5, 4	33.83		0.40		34.23	17.56
		5, 5	35.35		0.44		35.80	18.16
		50, 1	39.40		0.88		40.28	19.84
		50, 2	42.20		0.39		42.59	20.69
		50, 3	40.77		1.48		42.25	20.56
		50, 4	42.27		1.50		43.78	21.12
		50, 5	43.36		2.52		45.88	21.87
		500, 1	47.66		5.06		52.71	24.27
		500, 2	36.20		1.95		38.16	19.05
		500, 3	45.80		1.30		47.10	22.31
		500, 4	29.90		1.57		31.46	16.48
		500, 5	29.40		0.04		29.44	15.68
HM	W, G	Control, 0	60.54	-23.21	-44.46	-3.10	57.45	25.89
		5, 1	38.26	-23.27	-44.16	0.94	39.20	19.44
		5, 2	52.52	-23.26	-44.24	-1.78	50.73	23.59
		5, 3	17.58	-22.92	-45.59	5.87	23.45	13.22
		5, 4	37.35	-23.25	-44.27	0.94	38.28	19.10
		5, 5	26.18	-23.29	-44.07	5.08	31.26	16.40
		50, 1	18.73	-22.79	-46.18	4.09	22.82	12.95
		50, 2	23.39	-23.03	-45.14	3.74	27.12	14.75
		50, 3	26.26	-22.71	-46.53	0.43	26.69	14.57
		50, 4	21.89	-22.77	-46.28	2.40	24.30	13.58
		50, 5	11.67	-22.62	-46.93	7.60	19.27	11.41
		500, 1	0.85	-22.43	-47.79	22.93	23.78	13.36

	500, 2	-2.75	-22.37	-48.05	37.00	34.25	17.57
	500, 3	1.86	-22.90	-45.65	28.84	30.70	16.18
	500, 4	-3.01	-22.09	-49.45	32.92	29.91	15.87
	500, 5	3.74	-22.69	-46.57	19.48	23.22	13.12
W, DM	Control, 0	X	X	X	X	X	X
	5, 1	34.33	64.21	-1.42	1.52	35.85	18.18
	5, 2	X	X	X	X	X	X
	5, 3	32.48	68.01	-1.47	2.03	34.51	17.67
	5, 4	33.70	62.15	-1.42	1.49	35.19	17.93
	5, 5	34.01	107.87	-1.57	3.45	37.45	18.79
	50, 1	37.65	48.06	-1.11	0.05	37.70	18.88
	50, 2	39.20	61.97	-1.33	0.77	39.97	19.72
	50, 3	X	X	X	X	X	X
	50, 4	X	X	X	X	X	X
	50, 5	39.28	52.74	-1.18	0.20	39.48	19.54
	500, 1	38.46	111.54	-1.55	2.87	41.33	20.23
	500, 2	30.30	243.68	-1.66	6.32	36.61	18.47
	500, 3	38.27	-5,946.37	-1.69	7.12	45.39	21.70
	500, 4	25.95	109.31	-1.61	5.13	31.08	16.33
	500, 5	27.17	146.42	-1.64	5.78	32.95	17.06
G, DM	Control, 0	32.88	45.56	-1.14	1.62	34.51	17.67
	5, 1	33.94	49.80	-1.21	2.05	35.99	18.23
	5, 2	31.57	48.87	-1.26	2.51	34.08	17.50
	5, 3	X	X	X	X	X	X
	5, 4	33.33	48.46	-1.20	1.98	35.32	17.93
	5, 5	34.59	51.53	-1.23	2.16	36.75	18.52
	50, 1	X	X	X	X	X	X

		50, 2	X	X			X	X	X	X
		50, 3	X	X			X	X	X	X
		50, 4	X	X			X	X	X	X
		50, 5	X	X			X	X	X	X
		500, 1	X	X			X	X	X	X
		500, 2	X	X			X	X	X	X
		500, 3	X	X			X	X	X	X
		500, 4	X	X			X	X	X	X
		500, 5	X	X			X	X	X	X
3L	W, DM, G	Control, 0	35.20		1.43	2.69			39.12	19.41
		5, 1	35.26		0.61	0.16			35.89	18.20
		5, 2	33.87		1.69	1.72			37.28	18.72
		5, 3	31.35		0.43	2.01			33.22	17.17
		5, 4	34.46		0.58	0.14			35.03	17.86
		5, 5	34.59		0.10	0.63			35.08	17.89
		50, 1	34.42		1.20	1.35			36.97	18.60
		50, 2	38.08		0.53	0.76			39.35	19.49
		50, 3	36.14		0.92	0.08			36.69	18.50
		50, 4	36.87		1.37	0.62			38.71	19.26
		50, 5	35.32		4.03	4.59			43.92	21.17
		500, 1	34.29		12.98	22.81			68.70	29.61
		500, 2	25.03		12.27	37.50			67.94	29.36
		500, 3	35.06		9.63	32.30			69.34	29.81
		500, 4	20.83		9.70	29.52			54.67	24.95
		500, 5	23.63		2.97	16.60			37.67	18.87

Method	Test liquids	Exposure (mg/L), day	$\gamma_s^d 1$ (mJ m^{-2})	$\gamma_s^d 2$ (mJ m^{-2})	γ_s^+ (mJ m^{-2})	γ_s^- (mJ m^{-2})	$\gamma_s^{nd} 1$ (mJ m^{-2})	$\gamma_s^{nd} 2$ (mJ m^{-2})	γ_s (mJ m^{-2})	δ (MJ$^{1/2}$ m$^{-3/2}$)
Escarole abaxial surface										
GM	W, G	Control, 0	17.86				131.89		149.74	53.11
		5, 1	3.66				90.02		93.68	37.36
		5, 2	10.64				116.02		126.66	46.85
		5, 3	8.85				118.65		127.50	47.08
		5, 4	15.72				39.12		54.84	25.01
		5, 5	8.30				115.53		123.84	46.06
		50, 1	24.92				146.50		171.42	58.78
		50, 2	24.36				152.40		176.76	60.15
		50, 3	19.80				135.90		155.69	54.69
		50, 4	7.19				106.53		113.71	43.21
		50, 5	6.18				104.92		111.10	42.46
		500, 1	8.67				92.23		100.90	39.50
		500, 2	18.35				141.69		160.04	55.83
		500, 3	13.18				137.84		151.02	53.45
		500, 4	16.44				148.99		165.42	57.23
		500, 5	8.12				91.04		99.16	38.99
	W, DM	Control, 0	29.35				26.83		56.17	25.46
		5, 1	31.59				20.82		52.41	24.17
		5, 2	27.58				27.10		54.68	24.95
		5, 3	29.53				29.10		58.63	26.29
		5, 4	11.87				43.49		55.36	25.18
		5, 5	27.37				29.64		57.02	25.75
		50, 1	29.91				27.71		57.62	25.95

		50, 2	25.28		34.00		59.28	26.51
		50, 3	24.09		30.69		54.78	24.98
		50, 4	28.10		26.04		54.14	24.76
		50, 5	24.05		29.29		53.33	24.49
		500, 1	27.46		18.08		45.54	21.75
		500, 2	21.89		36.53		58.42	26.22
		500, 3	28.10		34.82		62.92	27.72
		500, 4	23.13		41.11		64.23	28.15
		500, 5	27.46		18.08		45.54	21.75
	G, DM	Control, 0	40.33		0.10		40.42	19.89
		5, 1	40.31		0.58		37.73	20.06
		5, 2	36.91		0.82		40.35	18.89
		5, 3	39.04		1.32		58.55	19.87
		5, 4	11.52		47.03		38.02	26.26
		5, 5	36.21		1.82		42.01	19.00
		50, 1	42.01		0.00		36.55	20.47
		50, 2	35.91		0.64		34.47	18.44
		50, 3	33.80		0.66		38.04	17.65
		50, 4	36.89		1.15		34.40	19.00
		50, 5	31.57		2.82		34.40	17.62
		500, 1	36.39		0.01		36.40	18.39
		500, 2	30.76		2.30		33.06	17.11
		500, 3	38.01		1.93		39.95	19.72
		500, 4	32.11		3.75		35.86	18.18
		500, 5	36.28		0.03		36.31	18.35
HM	W, G	Control, 0	-4.61	-23.17	-44.30	134.67	130.06	47.79
		5, 1	-1.03	-23.32	-43.71	75.87	74.84	31.57

	5, 2	-3.01	-23.26	-43.91	105.08	102.08	39.85
	5, 3	-1.87	-23.36	-43.45	101.98	100.10	39.27
	5, 4	18.66	-23.92	-41.21	37.28	55.94	25.38
	5, 5	-1.84	-23.36	-43.49	99.07	97.23	38.42
	50, 1	-5.69	-23.11	-44.56	170.75	165.05	57.14
	50, 2	-5.09	-23.19	-44.18	169.42	164.33	56.95
	50, 3	-4.95	-23.15	-44.38	143.70	138.75	50.16
	50, 4	-2.01	-23.31	-43.71	91.95	89.95	36.24
	50, 5	-1.52	-23.34	-43.57	88.88	87.36	35.45
	500, 1	-4.16	-23.03	-44.97	90.06	85.90	35.01
	500, 2	-4.01	-23.26	-43.88	140.42	136.42	49.53
	500, 3	-2.32	-23.39	-43.32	122.95	120.63	45.16
	500, 4	-2.74	-23.39	-43.32	138.23	135.49	49.28
	500, 5	-3.98	-23.05	-44.91	87.95	83.98	34.42
W, DM	Control, 0	35.98	-64.28	-1.78	26.79	62.78	27.67
	5, 1	36.95	-72.07	-1.78	22.69	59.64	26.63
	5, 2	34.33	-65.43	-1.78	26.68	61.00	27.08
	5, 3	36.58	-61.41	-1.79	28.51	65.09	28.44
	5, 4	21.14	-62.63	-1.78	35.29	56.43	25.55
	5, 5	34.57	-62.40	-1.78	28.50	63.08	27.77
	50, 1	36.70	-62.72	-1.78	27.55	64.25	28.16
	50, 2	33.25	-59.49	-1.79	31.29	64.53	28.25
	50, 3	31.58	-63.91	-1.78	28.64	60.22	26.82
	50, 4	34.64	-66.46	-1.78	25.99	60.63	26.96
	50, 5	31.31	-65.73	-1.78	27.63	58.94	26.39
	500, 1	32.50	-85.61	-1.77	20.01	52.51	24.20
	500, 2	30.30	-59.65	-1.79	32.43	62.73	27.66

		500, 3	36.16	-57.00			-1.79	32.49	68.65	29.59
		500, 4	32.16	-55.32			-1.79	36.07	68.23	29.46
		500, 5	32.50	-85.61			-1.77	20.01	52.51	24.20
	G, DM	Control, 0	38.91	51.82			-1.09	1.28	40.19	19.80
		5, 1	38.79	62.46			-1.30	2.70	41.50	20.29
		5, 2	35.99	59.55			-1.32	2.99	38.98	19.36
		5, 3	38.03	70.17			-1.40	3.86	41.88	20.43
		5, 4	21.15	322.93			-1.68	32.68	53.84	24.66
		5, 5	35.81	69.28			-1.42	4.35	40.16	19.80
		50, 1	41.92	45.95			-0.66	0.08	42.00	20.47
		50, 2	35.08	55.29			-1.28	2.60	37.69	18.87
		50, 3	33.34	52.00			-1.27	2.55	35.89	18.19
		50, 4	36.10	63.52			-1.37	3.51	39.61	19.59
		50, 5	32.27	67.40			-1.45	5.20	37.47	18.79
		500, 1	36.53	41.60			-0.76	0.31	36.84	18.55
		500, 2	31.39	61.54			-1.43	4.62	36.02	18.24
		500, 3	37.43	74.87			-1.44	4.58	42.01	20.48
		500, 4	33.06	76.02			-1.49	6.09	39.16	19.42
		500, 5	36.11	42.61			-0.85	0.52	36.63	18.48
3L	W, DM, G	Control, 0	24.84		22.71	156.04			143.91	51.55
		5, 1	28.14		12.13	104.61			99.38	39.06
		5, 2	24.19		15.51	134.74			115.63	43.75
		5, 3	26.26		14.30	136.84			114.74	43.50
		5, 4	16.27		9.93	31.71			51.76	23.94
		5, 5	24.55		12.60	132.39			106.25	41.06
		50, 1	24.73		28.34	174.95			165.56	57.27

		50, 2	21.47		22.47	178.22			148.03	52.66
		50, 3	20.62		19.55	158.64			132.00	48.32
		50, 4	25.03		12.91	122.90			104.70	40.61
		50, 5	22.00		9.28	118.72			88.38	35.76
		500, 1	23.50		16.74	109.57			109.15	41.90
		500, 2	19.31		15.47	162.37			119.54	44.86
		500, 3	24.96		15.65	158.35			124.53	46.25
		500, 4	20.84		13.74	169.00			117.22	44.20
		500, 5	23.58		16.18	107.98			107.17	41.33
Method	Test liquids	Exposure (mg/L), day	$\gamma_s^d 1$ (mJ m^{-2})	$\gamma_s^d 2$ (mJ m^{-2})	γ_s^+ (mJ m^{-2})	γ_s^- (mJ m^{-2})	$\gamma_s^{nd} 1$ (mJ m^{-2})	$\gamma_s^{nd} 2$ (mJ m^{-2})	γ_s (mJ m^{-2})	δ (MJ$^{1/2}$ m$^{-3/2}$)
Escarole adaxial surface										
GM	W, G	Control, 0	1.70				91.88		93.58	37.33
		5, 1	1.67				85.24		86.92	35.32
		5, 2	1.15				87.19		88.34	35.75
		5, 3	1.68				89.98		91.66	36.76
		5, 4	1.74				95.76		97.50	38.50
		5, 5	0.08				74.22		74.30	31.40
		50, 1	8.94				121.90		130.84	48.00
		50, 2	4.53				107.42		111.96	42.71
		50, 3	3.96				108.72		112.69	42.91
		50, 4	3.39				98.75		102.14	39.87
		50, 5	6.66				109.59		116.24	43.93
		500, 1	12.99				117.94		130.94	48.03
		500, 2	45.41				189.75		235.16	74.51
		500, 3	22.92				140.76		163.67	56.78

	500, 4	1.79	97.24	99.02	38.95
	500, 5	10.16	96.41	106.57	41.16
W, DM	Control, 0	24.40	30.30	54.70	24.96
	5, 1	27.51	24.58	52.09	24.06
	5, 2	28.94	26.20	55.14	25.11
	5, 3	24.78	28.99	53.77	24.64
	5, 4	27.20	30.39	57.58	25.94
	5, 5	28.69	24.30	52.98	24.37
	50, 1	21.76	36.43	58.19	26.14
	50, 2	27.81	30.52	58.33	26.19
	50, 3	22.72	36.11	58.83	26.36
	50, 4	24.79	30.01	54.80	24.99
	50, 5	23.76	31.30	55.06	25.08
	500, 1	26.56	26.36	52.92	24.34
	500, 2	22.93	38.92	61.85	27.37
	500, 3	25.47	29.53	55.01	25.06
	500, 4	21.30	35.64	56.94	25.72
	500, 5	35.95	14.56	50.50	23.51
G, DM	Control, 0	30.73	5.54	36.27	18.34
	5, 1	34.54	2.74	37.29	18.72
	5, 2	36.05	3.46	39.51	19.55
	5, 3	31.19	4.91	36.10	18.28
	5, 4	34.19	4.89	39.09	19.40
	5, 5	34.83	4.33	39.17	19.43
	50, 1	29.22	4.71	33.93	17.44
	50, 2	35.89	3.19	39.07	19.39
	50, 3	29.39	6.74	36.13	18.28

		50, 4	31.80		4.14		35.94	18.21
		50, 5	31.32		3.35		34.66	17.73
		500, 1	36.01		0.51		36.52	18.43
		500, 2	34.87		0.17		35.04	17.87
		500, 3	35.99		0.22		36.21	18.32
		500, 4	26.95		8.79		35.74	18.14
		500, 5	47.39		0.68		48.07	22.65
HM	W, G	Control, 0	1.28	-23.49	-42.96	72.74	74.02	31.31
		5, 1	0.62	-23.42	-43.28	69.10	69.72	29.94
		5, 2	1.62	-23.49	-42.96	69.03	70.64	30.24
		5, 3	1.11	-23.47	-43.05	71.66	72.76	30.91
		5, 4	1.61	-23.52	-42.81	75.02	76.63	32.14
		5, 5	3.16	-23.52	-42.83	58.94	62.10	27.45
		50, 1	-1.64	-23.39	-43.32	103.93	102.29	39.91
		50, 2	-0.09	-23.45	-43.08	86.84	86.74	35.27
		50, 3	0.51	-23.50	-42.89	86.52	87.03	35.36
		50, 4	0.07	-23.43	-43.18	79.84	79.90	33.16
		50, 5	-1.40	-23.37	-43.45	92.32	90.92	36.53
		500, 1	-3.90	-23.19	-44.24	112.72	108.82	41.81
		500, 2	-7.43	-23.04	-44.83	364.13	356.69	101.84
		500, 3	-5.55	-23.11	-44.58	159.22	153.67	54.16
		500, 4	1.70	-23.53	-42.76	75.95	77.65	32.46
		500, 5	-4.52	-23.02	-45.04	96.20	91.67	36.76
	W, DM	Control, 0	31.81	-65.10	-1.78	28.43	60.24	26.83
		5, 1	33.80	-69.37	-1.78	24.82	58.62	26.29
		5, 2	35.48	-65.47	-1.78	26.26	61.73	27.33
		5, 3	31.96	-65.43	-1.78	27.55	59.51	26.59

	5, 4	34.53	-61.71	-1.79	29.02	63.55	27.93
	5, 5	34.88	-23.52	-1.78	24.81	59.68	26.64
	50, 1	30.16	-59.84	-1.79	32.33	62.49	27.58
	50, 2	35.15	-61.12	-1.79	29.23	64.39	28.20
	50, 3	31.06	-59.41	-1.79	32.30	63.36	27.87
	50, 4	32.14	-64.11	-1.78	28.29	60.43	26.89
	50, 5	31.35	-63.47	-1.78	29.02	60.38	26.88
	500, 1	35.14	-53.59	-1.78	25.96	59.18	26.47
	500, 2	31.67	-56.98	-1.79	34.40	66.07	28.75
	500, 3	32.72	-64.10	-1.78	28.07	60.79	27.01
	500, 4	29.60	-60.94	-1.79	31.67	61.27	27.17
	500, 5	39.61	-83.93	-1.77	18.47	58.08	26.10
G, DM	Control, 0	32.47	85.65	-1.53	7.51	39.98	19.73
	5, 1	34.77	74.07	-1.46	5.28	40.05	19.75
	5, 2	36.37	84.94	-1.49	6.05	42.42	20.63
	5, 3	32.67	82.38	-1.52	7.04	39.70	19.63
	5, 4	35.28	92.17	-1.53	7.19	42.47	20.64
	5, 5	35.64	89.27	-1.52	6.76	42.40	20.62
	50, 1	30.91	75.01	-1.51	6.76	37.67	18.87
	50, 2	36.12	81.86	-1.49	5.79	41.90	20.44
	50, 3	31.66	89.98	-1.55	8.34	40.01	19.74
	50, 4	32.93	78.22	-1.50	6.42	39.36	19.50
	50, 5	32.24	70.82	-1.47	5.69	37.93	18.97
	500, 1	35.14	53.59	-1.25	2.34	37.48	18.79
	500, 2	34.31	45.80	-1.08	1.34	35.64	18.10
	500, 3	35.17	48.50	-1.13	1.57	36.73	18.51
	500, 4	30.09	95.15	-1.57	9.64	39.73	19.64

		500, 5	X	X			X	X	X	X
3L	W, DM, G	Control, 0	23.34		4.72	101.17			67.06	29.08
		5, 1	25.56		6.80	95.90			76.62	32.13
		5, 2	27.15		6.13	97.45			76.04	31.95
		5, 3	23.57		5.04	99.46			68.34	29.49
		5, 4	25.78		5.66	106.11			74.78	31.55
		5, 5	27.45		3.85	81.76			62.94	27.73
		50, 1	20.17		8.92	136.52			89.97	36.25
		50, 2	25.64		9.01	121.19			91.74	36.78
		50, 3	21.76		5.50	119.63			73.05	31.00
		50, 4	23.22		6.78	110.23			77.89	32.53
		50, 5	21.84		9.11	123.57			88.95	35.94
		500, 1	22.99		17.20	137.82			120.37	45.09
		500, 2	18.53		32.63	224.48			189.70	63.43
		500, 3	21.41		23.11	165.93			145.27	51.92
		500, 4	20.97		3.16	105.15			57.46	25.89
		500, 5	29.87		24.80	118.05			138.08	49.98

References

[1] P. Christian, F. Von der Kammer, M. Baalousha, and T. Hofmann, "Nanoparticles: structure, properties, preparation and behaviour in environmental media," *Ecotoxicol. Lond. Engl.*, vol. 17, no. 5, pp. 326–343, Jul. 2008.

[2] European Commission, "Communication from the Commission to the European Parliament, the Council and the European Economic and Social Committee," *Official Journal of the European Union Document 52012DC0572*, 2012. [Online]. Available: http://eur-lex.europa.eu/legal-content/EN/TXT/HTML/?uri=CELEX:52012DC0572&from=EN. [Accessed: 03-Jun-2017].

[3] G. Bystrzejewska-Piotrowska, J. Golimowski, and P. L. Urban, "Nanoparticles: their potential toxicity, waste and environmental management," *Waste Manag.*, vol. 29, no. 9, pp. 2587–2595, Sep. 2009.

[4] W. Lojkowski *et al.*, "Eighth Nanoforum Report: Nanometrology." EU (FP5) Thematic Network, 2006.

[5] D. Y. Lai and P. G. Sayre, "Toxicity Testing and Evaluation of Nanoparticles: Challenges in Risk Assessment," in *Nanotoxicity*, S. C. Sahu and D. A. Casciano, Eds. John Wiley & Sons, Ltd, 2009, pp. 427–457.

[6] B. Nowack and T. D. Bucheli, "Occurrence, behavior and effects of nanoparticles in the environment," *Environ. Pollut.*, vol. 150, no. 1, pp. 5–22, Nov. 2007.

[7] P. Biswas and C.-Y. Wu, "Nanoparticles and the Environment," *J. Air Waste Manag. Assoc.*, vol. 55, no. 6, pp. 708–746, Jun. 2005.

[8] R. D. Handy, R. Owen, and E. Valsami-Jones, "The ecotoxicology of nanoparticles and nanomaterials: current status, knowledge gaps, challenges, and future needs," *Ecotoxicol. Lond. Engl.*, vol. 17, no. 5, pp. 315–325, Jul. 2008.

[9] F. Gottschalk, T. Sonderer, R. W. Scholz, and B. Nowack, "Modeled Environmental Concentrations of Engineered Nanomaterials (TiO2, ZnO, Ag, CNT, Fullerenes) for Different Regions," *Environ. Sci. Technol.*, vol. 43, no. 24, pp. 9216–9222, Dec. 2009.

[10] C. Sioutas, R. J. Delfino, and M. Singh, "Exposure Assessment for Atmospheric Ultrafine Particles (UFPs) and Implications in Epidemiologic Research," *Environ. Health Perspect.*, vol. 113, no. 8, pp. 947–955, Aug. 2005.

[11] M. Kulmala *et al.*, "Formation and growth rates of ultrafine atmospheric particles: A review of observations," *J. Aerosol Sci.*, vol. 35, no. 2, pp. 143–176, Feb. 2004.

[12] E. Navarro *et al.*, "Environmental behavior and ecotoxicity of engineered nanoparticles to algae, plants, and fungi," *Ecotoxicol. Lond. Engl.*, vol. 17, no. 5, pp. 372–386, Jul. 2008.

[13] T. Hussein, A. Puustinen, P. P. Aalto, J. M. Mäkelä, K. Hämeri, and M. Kulmala, "Urban aerosol number size distributions," *Atmos Chem Phys*, vol. 4, no. 2, pp. 391–411, Mar. 2004.

[14] J. Csavina *et al.*, "A review on the importance of metals and metalloids in atmospheric dust and aerosol from mining operations," *Sci. Total Environ.*, vol. 433, pp. 58–73, Sep. 2012.

[15] J. H. Vincent and C. F. Clement, "Ultrafine particles in workplace atmospheres," *Philos. Trans. R. Soc. Lond. Math. Phys. Eng. Sci.*, vol. 358, no. 1775, pp. 2673–2682, Oct. 2000.

[16] K. M. Zhang and A. S. Wexler, "Evolution of particle number distribution near roadways—Part I: analysis of aerosol dynamics and its implications for engine emission measurement," *Atmos. Environ.*, vol. 38, no. 38, pp. 6643–6653, Dec. 2004.

[17] G. Oberdörster, "Pulmonary effects of inhaled ultrafine particles," *Int. Arch. Occup. Environ. Health*, vol. 74, no. 1, pp. 1–8, Nov. 2000.

[18] D. B. Kittelson, "Engines and nanoparticles: a review," *J. Aerosol Sci.*, vol. 29, no. 5–6, pp. 575–588, Jun. 1998.

[19] P. F. DeCarlo, J. G. Slowik, D. R. Worsnop, P. Davidovits, and J. L. Jimenez, "Particle Morphology and Density Characterization by Combined Mobility and Aerodynamic Diameter Measurements. Part 1: Theory," *Aerosol Sci. Technol.*, vol. 38, no. 12, pp. 1185–1205, Jan. 2004.

[20] P. Kulkarni, P. A. Baron, and K. Willeke, "Introduction to Aerosol Characterization," in *Aerosol Measurement*, P. Kulkarni, P. A. Baron, and K. Willeke, Eds. John Wiley & Sons, Inc., 2011, pp. 1–13.

[21] S. V. Hering, "Impactors, Cyclones, and Other Inertial and Gravitational Collectors," in *Air Sampling Instruments*, 8th Edition., B. S. Cohen and S. V. Hering, Eds. Cincinnati, OH: American Conference of Governmental Industrial Hygienists, 1995.

[22] W. C. Hinds, *Aerosol Technology: Properties, Behavior, and Measurement of Airborne Particles.*, 2nd edition. New York, NY: John Wiley & Sons, Ltd, 2012.

[23] J. H. Vincent, *Aerosol Sampling: Science, Standards, Instrumentation and Applications*. 2007.

[24] J. H. Kim, G. W. Mulholland, S. R. Kukuck, and D. Y. H. Pui, "Slip Correction Measurements of Certified PSL Nanoparticles Using a Nanometer Differential Mobility Analyzer (Nano-DMA) for Knudsen Number From 0.5 to 83," *J. Res. Natl. Inst. Stand. Technol.*, vol. 110, no. 1, pp. 31–54, Feb. 2005.

[25] J. Happel and H. Brenner, *Low Reynolds Number Hydrodynamics: with Special Applications to Particulate Media*, 2nd Edition. The Hague, Netherlands: Martinus Nijhoff Publishers, 1983.

[26] W. P. Kelly and P. H. McMurry, "Measurement of Particle Density by Inertial Classification of Differential Mobility Analyzer–Generated Monodisperse Aerosols," *Aerosol Sci. Technol.*, vol. 17, no. 3, pp. 199–212, Jan. 1992.

[27] S. V. Hering, *Air sampling instruments for evaluation of atmospheric contaminants*. American Conference of Governmental Industrial Hygi enists, 1989.

[28] M. Marjamäki, J. Keskinen, D.-R. Chen, and D. Y. H. Pui, "Performance Evaluation of the Electrical Low-Pressure Impactor (ELPI)," *J. Aerosol Sci.*, vol. 31, no. 2, pp. 249–261, Feb. 2000.

[29] Y. Ju-Nam and J. R. Lead, "Manufactured nanoparticles: An overview of their chemistry, interactions and potential environmental implications," *Sci. Total Environ.*, vol. 400, no. 1–3, pp. 396–414, Aug. 2008.

[30] J. P. Mitchell and M. W. Nagel, "Cascade impactors for the size characterization of aerosols from medical inhalers: their uses and limitations," *J. Aerosol Med. Off. J. Int. Soc. Aerosols Med.*, vol. 16, no. 4, pp. 341–377, 2003.

[31] S. C. Wang and R. C. Flagan, "Scanning Electrical Mobility Spectrometer," *Aerosol Sci. Technol.*, vol. 13, no. 2, pp. 230–240, Jan. 1990.

[32] N. A. Fuchs, "On the stationary charge distribution on aerosol particles in a bipolar ionic atmosphere," *Geofis. Pura E Appl.*, vol. 56, no. 1, pp. 185–193, Sep. 1963.

[33] E. O. Knutson and K. T. Whitby, "Aerosol classification by electric mobility: apparatus, theory, and applications," *J. Aerosol Sci.*, vol. 6, no. 6, pp. 443–451, Nov. 1975.

[34] S. V. Hering, M. R. Stolzenburg, F. R. Quant, D. R. Oberreit, and P. B. Keady, "A Laminar-Flow, Water-Based Condensation Particle Counter (WCPC)," *Aerosol Sci. Technol.*, vol. 39, no. 7, pp. 659–672, Jul. 2005.

[35] H.-C. Chuang, T. Jones, T.-T. Chen, and K. BéruBé, "Cytotoxic effects of incense particles in relation to oxidative stress, the cell cycle and F-actin assembly," *Toxicol. Lett.*, vol. 220, no. 3, pp. 229–237, Jul. 2013.

[36] H.-C. Chuang, T. P. Jones, S.-C. C. Lung, and K. A. BéruBé, "Soot-driven reactive oxygen species formation from incense burning," *Sci. Total Environ.*, vol. 409, no. 22, pp. 4781–4787, Oct. 2011.

[37] R. Cohen, K. G. Sexton, and K. B. Yeatts, "Hazard assessment of United Arab Emirates (UAE) incense smoke," *Sci. Total Environ.*, vol. 458–460, pp. 176–186, Aug. 2013.

[38] S.-C. Lee and B. Wang, "Characteristics of emissions of air pollutants from burning of incense in a large environmental chamber," *Atmos. Environ.*, vol. 38, no. 7, pp. 941–951, Mar. 2004.

[39] S. W. See and R. Balasubramanian, "Characterization of fine particle emissions from incense burning," *Build. Environ.*, vol. 46, no. 5, pp. 1074–1080, May 2011.

[40] B. Wang, S. C. Lee, and K. F. Ho, "Chemical composition of fine particles from incense burning in a large environmental chamber," *Atmos. Environ.*, vol. 40, no. 40, pp. 7858–7868, Dec. 2006.

[41] J. J. Jetter, Z. Guo, J. A. McBrian, and M. R. Flynn, "Characterization of emissions from burning incense," *Sci. Total Environ.*, vol. 295, no. 1, pp. 51–67, Aug. 2002.

[42] Y.-C. Chang, H.-W. Lee, and H.-H. Tseng, "The formation of incense smoke," *J. Aerosol Sci.*, vol. 38, no. 1, pp. 39–51, Jan. 2007.

[43] T. V. Vu, J. Ondracek, V. Zdímal, J. Schwarz, J. M. Delgado-Saborit, and R. M. Harrison, "Physical properties and lung deposition of particles emitted from five major indoor sources," *Air Qual. Atmosphere Health*, vol. 10, no. 1, pp. 1–14, Jan. 2017.

[44] C.-R. Yang, T.-C. Lin, and F.-H. Chang, "Particle size distribution and PAH concentrations of incense smoke in a combustion chamber," *Environ. Pollut. Barking Essex 1987*, vol. 145, no. 2, pp. 606–615, Jan. 2007.

[45] S. Bootdee, S. Chantara, and T. Prapamontol, "Determination of PM2.5 and polycyclic aromatic hydrocarbons from incense burning emission at shrine for health risk assessment," *Atmospheric Pollut. Res.*, vol. 7, no. 4, pp. 680–689, Jul. 2016.

[46] S. S. H. Ho and J. Z. Yu, "Concentrations of formaldehyde and other carbonyls in environments affected by incense burning," *J. Environ. Monit. JEM*, vol. 4, no. 5, pp. 728–733, Oct. 2002.

[47] S.-C. Kuo and Y. I. Tsai, "Emission characteristics of allergenic terpenols in PM2.5 released from incense burning and the effect of light on the emissions," *Sci. Total Environ.*, vol. 584–585, pp. 495–504, Apr. 2017.

[48] S.-C. Kuo, Y. I. Tsai, and K. Sopajaree, "Emission characteristics of carboxylates in PM2.5 from incense burning with the effect of light on acetate," *Atmos. Environ.*, vol. 138, pp. 125–134, Aug. 2016.

[49] K. H. Lui *et al.*, "Characterization of chemical components and bioreactivity of fine particulate matter (PM2.5) during incense burning," *Environ. Pollut. Barking Essex 1987*, vol. 213, pp. 524–532, Jun. 2016.

[50] S.-C. C. Lung, M.-C. Kao, and S.-C. Hu, "Contribution of incense burning to indoor PM10 and particle-bound polycyclic aromatic hydrocarbons under two ventilation conditions," *Indoor Air*, vol. 13, no. 2, pp. 194–199, Jun. 2003.

[51] P. Navasumrit *et al.*, "Potential health effects of exposure to carcinogenic compounds in incense smoke in temple workers," *Chem. Biol. Interact.*, vol. 173, no. 1, pp. 19–31, May 2008.

[52] J. S. Brown, K. L. Zeman, and W. D. Bennett, "Ultrafine Particle Deposition and Clearance in the Healthy and Obstructed Lung," *Am. J. Respir. Crit. Care Med.*, vol. 166, no. 9, pp. 1240–1247, Nov. 2002.

[53] Y. S. Cheng, W. E. Bechtold, C. C. Yu, and I. F. Hung, "Incense Smoke: Characterization and Dynamics in Indoor Environments.," *Aerosol Sci. Technol.*, vol. 23, no. 3, pp. 271–281, 1995.

[54] N. Lewinski, H. Zhu, and R. Drezek, "Evaluating Strategies For Risk Assessment of Nanomaterials," in *Nanotoxicity*, S. C. Sahu and D. A. Casciano, Eds. John Wiley & Sons, Ltd, 2009, pp. 459–498.

[55] R. Hayakawa, K. Matsunaga, and Y. Arima, "Depigmented Contact Dermatitis Due to Incense.," *Contact Dermatitis*, vol. 16, pp. 272–274, 1987.

[56] M. E. Vance and L. C. Marr, "Exposure to airborne engineered nanoparticles in the indoor environment," *Atmos. Environ.*, vol. 106, no. Supplement C, pp. 503–509, Apr. 2015.

[57] G. Löfroth, C. Stensman, and M. Brandhorst-Satzkorn, "Indoor sources of mutagenic aerosol particulate matter: smoking, cooking and incense burning," *Mutat. Res.*, vol. 261, no. 1, pp. 21–28, Sep. 1991.

[58] L.-Y. Chen and C. Ho, "Incense Burning during Pregnancy and Birth Weight and Head Circumference among Term Births: The Taiwan Birth Cohort Study," *Environ. Health Perspect.*, vol. 124, no. 9, pp. 1487–1492, Sep. 2016.

[59] Y. C. Chen, W. C. Ho, and Y. H. Yu, "Adolescent lung function associated with incense burning and other environmental exposures at home," *Indoor Air*, vol. 27, no. 4, pp. 746–752, Jul. 2017.

[60] X. Song *et al.*, "The Association of Domestic Incense Burning with Hypertension and Blood Pressure in Guangdong, China," *Int. J. Environ. Res. Public. Health*, vol. 14, no. 7, Jul. 2017.

[61] European Commission, "Standards - Air Quality - Environment - European Commission," 2015. [Online]. Available: http://ec.europa.eu/environment/air/quality/standards.htm. [Accessed: 19-Dec-2017].

[62] X. Ji *et al.*, "Characterization of particles emitted by incense burning in an experimental house," *Indoor Air*, vol. 20, no. 2, pp. 147–158, Apr. 2010.

[63] T.-C. Lin, C.-R. Yang, and F.-H. Chang, "Burning characteristics and emission products related to metallic content in incense," *J. Hazard. Mater.*, vol. 140, no. 1–2, pp. 165–172, Feb. 2007.

[64] S. W. See, R. Balasubramanian, and U. Man Joshi, "Physical characteristics of nanoparticles emitted from incense smoke," *Sci. Technol. Adv. Mater.*, vol. 8, no. 1, pp. 25–32, Jan. 2007.

[65] L. Stabile, F. C. Fuoco, and G. Buonanno, "Characteristics of particles and black carbon emitted by combustion of incenses, candles and anti-mosquito products," *Build. Environ.*, vol. 56, no. Supplement C, pp. 184–191, Oct. 2012.

[66] R. C. Mannix, K. P. Nguyen, E. W. Tan, E. E. Ho, and R. F. Phalen, "Physical characterization of incense aerosols," *Sci. Total Environ.*, vol. 193, no. 2, pp. 149–158, Dec. 1996.

[67] D. Rim, M. Green, L. Wallace, A. Persily, and J.-I. Choi, "Evolution of Ultrafine Particle Size Distributions Following Indoor Episodic Releases: Relative Importance of Coagulation, Deposition and Ventilation," *Aerosol Sci. Technol.*, vol. 46, no. 5, pp. 494–503, May 2012.

[68] J.-D. Hu, Y. Zevi, X.-M. Kou, J. Xiao, X.-J. Wang, and Y. Jin, "Effect of dissolved organic matter on the stability of magnetite nanoparticles under different pH and ionic strength conditions," *Sci. Total Environ.*, vol. 408, no. 16, pp. 3477–3489, Jul. 2010.

[69] J. Jiang, G. Oberdörster, and P. Biswas, "Characterization of size, surface charge, and agglomeration state of nanoparticle dispersions for toxicological studies," *J. Nanoparticle Res.*, vol. 11, no. 1, pp. 77–89, Jan. 2009.

[70] J. Buffle, K. J. Wilkinson, S. Stoll, M. Filella, and J. Zhang, "A Generalized Description of Aquatic Colloidal Interactions: The Three-colloidal Component Approach," *Environ. Sci. Technol.*, vol. 32, no. 19, pp. 2887–2899, Oct. 1998.

[71] E. Illés and E. Tombácz, "The effect of humic acid adsorption on pH-dependent surface charging and aggregation of magnetite nanoparticles," *J. Colloid Interface Sci.*, vol. 295, no. 1, pp. 115–123, Mar. 2006.

[72] K. L. Chen and M. Elimelech, "Influence of humic acid on the aggregation kinetics of fullerene (C60) nanoparticles in monovalent and divalent electrolyte solutions," *J. Colloid Interface Sci.*, vol. 309, no. 1, pp. 126–134, May 2007.

[73] S. A. Blaser, M. Scheringer, M. Macleod, and K. Hungerbühler, "Estimation of cumulative aquatic exposure and risk due to silver: contribution of nano-functionalized plastics and textiles," *Sci. Total Environ.*, vol. 390, no. 2–3, pp. 396–409, Feb. 2008.

[74] O. Choi, T. E. Clevenger, B. Deng, R. Y. Surampalli, L. Ross Jr., and Z. Hu, "Role of sulfide and ligand strength in controlling nanosilver toxicity," *Water Res.*, vol. 43, no. 7, pp. 1879–1886, Apr. 2009.

[75] A. A. Keller *et al.*, "Stability and Aggregation of Metal Oxide Nanoparticles in Natural Aqueous Matrices," *Environ. Sci. Technol.*, vol. 44, no. 6, pp. 1962–1967, Mar. 2010.

[76] B. K. G. Theng and G. Yuan, "Nanoparticles in the Soil Environment," *Elements*, vol. 4, no. 6, pp. 395–399, Dec. 2008.

[77] M. Hassellöv, J. W. Readman, J. F. Ranville, and K. Tiede, "Nanoparticle analysis and characterization methodologies in environmental risk assessment of engineered nanoparticles," *Ecotoxicol. Lond. Engl.*, vol. 17, no. 5, pp. 344–361, Jul. 2008.

[78] J. Fang, X. Shan, B. Wen, J. Lin, and G. Owens, "Stability of titania nanoparticles in soil suspensions and transport in saturated homogeneous soil columns," *Environ. Pollut.*, vol. 157, no. 4, pp. 1101–1109, Apr. 2009.

[79] M. B. McGechan and D. R. Lewis, "SW—Soil and Water," *Biosyst. Eng.*, vol. 83, no. 3, pp. 255–273, Nov. 2002.

[80] T. K. Sen and K. C. Khilar, "Review on subsurface colloids and colloid-associated contaminant transport in saturated porous media," *Adv. Colloid Interface Sci.*, vol. 119, no. 2–3, pp. 71–96, Feb. 2006.

[81] J. N. Ryan and M. Elimelech, "Colloid mobilization and transport in groundwater," *Colloids Surf. Physicochem. Eng. Asp.*, vol. 107, pp. 1–56, Feb. 1996.

[82] T. K. Darlington, A. M. Neigh, M. T. Spencer, O. T. Nguyen, and S. J. Oldenburg, "Nanoparticle characteristics affecting environmental fate and transport through soil," *Environ. Toxicol. Chem.*, vol. 28, no. 6, pp. 1191–1199, Jun. 2009.

[83] H. F. Lecoanet, J.-Y. Bottero, and M. R. Wiesner, "Laboratory Assessment of the Mobility of Nanomaterials in Porous Media," *Environ. Sci. Technol.*, vol. 38, no. 19, pp. 5164–5169, Oct. 2004.

[84] H. F. Lecoanet and M. R. Wiesner, "Velocity Effects on Fullerene and Oxide Nanoparticle Deposition in Porous Media," *Environ. Sci. Technol.*, vol. 38, no. 16, pp. 4377–4382, Aug. 2004.

[85] Q. Chaudhry *et al.*, "Applications and implications of nanotechnologies for the food sector," *Food Addit. Contam. Part Chem. Anal. Control Expo. Risk Assess.*, vol. 25, no. 3, pp. 241–258, Mar. 2008.

[86] E. Fröhlich *et al.*, "Cytotoxicity of nanoparticles independent from oxidative stress," *J. Toxicol. Sci.*, vol. 34, no. 4, pp. 363–375, 2009.

[87] M. E. Pettitt and J. R. Lead, "Minimum physicochemical characterisation requirements for nanomaterial regulation," *Environ. Int.*, vol. 52, pp. 41–50, Feb. 2013.

[88] J. W. Card and B. A. Magnuson, "A Method to Assess the Quality of Studies That Examine the Toxicity of Engineered Nanomaterials," *Int. J. Toxicol.*, vol. 29, no. 4, pp. 402–410, Jul. 2010.

[89] C. M. Sayes and D. B. Warheit, "Characterization of nanomaterials for toxicity assessment," *Wiley Interdiscip. Rev. Nanomed. Nanobiotechnol.*, vol. 1, no. 6, pp. 660–670, Nov. 2009.

[90] EFSA Scientific Committee, "Guidance on the risk assessment of the application of nanoscience and nanotechnologies in the food and feed chain," *EFSA J.*, vol. 9, no. 5, p. n/a-n/a, May 2011.

[91] C.-F. Chau, S.-H. Wu, and G.-C. Yen, "The development of regulations for food nanotechnology," *Trends Food Sci. Technol.*, vol. 18, no. 5, pp. 269–280, May 2007.

[92] M. Cushen, J. Kerry, M. Morris, M. Cruz-Romero, and E. Cummins, "Nanotechnologies in the food industry – Recent developments, risks and regulation," *Trends Food Sci. Technol.*, vol. 24, no. 1, pp. 30–46, Mar. 2012.

[93] M. Rossi *et al.*, "Scientific basis of nanotechnology, implications for the food sector and future trends," *Trends Food Sci. Technol.*, vol. 40, no. 2, pp. 127–148, Dec. 2014.

[94] Food and Agriculture Organization of the United Nations & World Health Organization, "State of the Art on the Initiatives and Activities Relevant to Risk Assessment and Risk Management of Nanotechnologies in the Food and Agriculture Sectors: FAO/WHO Technical Paper." 2013.

[95] J. W. Card, T. S. Jonaitis, S. Tafazoli, and B. A. Magnuson, "An appraisal of the published literature on the safety and toxicity of food-related nanomaterials," *Crit. Rev. Toxicol.*, vol. 41, no. 1, pp. 20–49, Jan. 2011.

[96] K. Tiede, A. B. A. Boxall, S. P. Tear, J. Lewis, H. David, and M. Hassellov, "Detection and characterization of engineered nanoparticles in food and the environment," *Food Addit. Contam. Part Chem. Anal. Control Expo. Risk Assess.*, vol. 25, no. 7, pp. 795–821, Jul. 2008.

[97] R. Peters *et al.*, "Identification and characterization of organic nanoparticles in food," *TrAC Trends Anal. Chem.*, vol. 30, no. 1, pp. 100–112, Jan. 2011.

[98] X. Song, R. Li, H. Li, Z. Hu, A. Mustapha, and M. Lin, "Characterization and Quantification of Zinc Oxide and Titanium Dioxide Nanoparticles in Foods," *Food Bioprocess Technol.*, vol. 7, no. 2, pp. 456–462, Feb. 2014.

[99] P. Echlin, *Handbook of Sample Preparation for Scanning Electron Microscopy and X-Ray Microanalysis*. Springer Science & Business Media, 2011.

[100] R. F. Egerton, "Electron Optics," in *Physical Principles of Electron Microscopy*, Springer, Cham, 2016, pp. 27–54.

[101] I. Valdez-Vazquez, F. R. Quiroz-Figueroa, J. Carrillo-Reyes, and A. Medina-López, "Microscopy Applied In Biomass Characterization," in *Analytical Techniques and Methods for Biomass*, Springer, Cham, 2016, pp. 173–196.

[102] B. M. Simonet and M. Valcárcel, "Monitoring nanoparticles in the environment," *Anal. Bioanal. Chem.*, vol. 393, no. 1, p. 17, Jan. 2009.

[103] R. F. Egerton, "Analytical Electron Microscopy," in *Physical Principles of Electron Microscopy*, Springer, Cham, 2016, pp. 149–169.

[104] A. Lapresta-Fernández *et al.*, "A General Perspective of the Characterization and Quantification of Nanoparticles: Imaging, Spectroscopic, and Separation Techniques," *Crit. Rev. Solid State Mater. Sci.*, vol. 39, no. 6, pp. 423–458, Nov. 2014.

[105] E. Uggerud *et al.*, *Topics in Current Chemistry*. Berlin, Germany: Springer-Verlag, 2003.

[106] Agilent Technologies, "Agilent 7500 Series ICPMS: Hardware Manual." Agilent Technologies, Inc., 2008.

[107] R. Thomas, *Practical Guide to ICP-MS*. New York, NY: Marcel Dekker, Inc., 2004.

[108] R. Saadi, Z. Saadi, R. Fazaeli, and N. E. Fard, "Monolayer and multilayer adsorption isotherm models for sorption from aqueous media," *Korean J. Chem. Eng.*, vol. 32, no. 5, pp. 787–799, May 2015.

[109] K. S. W. Sing, "Adsorption methods for the characterization of porous materials," *Adv. Colloid Interface Sci.*, vol. 76, no. Supplement C, pp. 3–11, Jul. 1998.

[110] M. D. Donohue and G. L. Aranovich, "Classification of Gibbs adsorption isotherms," *Adv. Colloid Interface Sci.*, vol. 76, no. Supplement C, pp. 137–152, Jul. 1998.

[111] W. Feng, B. Wang, and Y. Zhao, "Nanotoxicity of Metal Oxide Nanoparticles in Vivo," in *Nanotoxicity: From In Vivo and In Vitro Methods to Health Risks*, 1st edition., S. C. Sahu and D. A. Casciano, Eds. John Wiley & Sons, Ltd, 2009, pp. 247–269.

[112] EFSA Scientific Committee, "The Potential Risks Arising from Nanoscience and Nanotechnologies on Food and Feed Safety," *EFSA J.*, vol. 7, no. 3, p. n/a-n/a, Mar. 2009.

[113] A. des Rieux, V. Fievez, M. Garinot, Y.-J. Schneider, and V. Préat, "Nanoparticles as potential oral delivery systems of proteins and vaccines: a mechanistic approach," *J. Control. Release Off. J. Control. Release Soc.*, vol. 116, no. 1, pp. 1–27, Nov. 2006.

[114] L. Szentkuti, "Light microscopical observations on luminally administered dyes, dextrans, nanospheres and microspheres in the pre-epithelial mucus gel layer of the rat distal colon," *J. Controlled Release*, vol. 46, no. 3, pp. 233–242, Jun. 1997.

[115] P. Jani, G. W. Halbert, J. Langridge, and A. T. Florence, "Nanoparticle uptake by the rat gastrointestinal mucosa: quantitation and particle size dependency," *J. Pharm. Pharmacol.*, vol. 42, no. 12, pp. 821–826, Dec. 1990.

[116] A. T. Florence, A. M. Hillery, N. Hussain, and P. U. Jani, "Factors Affecting the Oral Uptake and Translocation of Polystyrene Nanoparticles: Histological and Analytical Evidence," *J. Drug Target.*, vol. 3, no. 1, pp. 65–70, Jan. 1995.

[117] S. Hoshi, A. Uchino, K. Kusanagi, T. Ihara, and S. Ueda, "Uptake of orally administered polystyrene latex and poly(D,L-lactic/glycolic acid) microspheres into intestinal lymphoid tissues in chickens," *Vet. Immunol. Immunopathol.*, vol. 70, no. 1, pp. 33–42, Sep. 1999.

[118] M. Shakweh, M. Besnard, V. Nicolas, and E. Fattal, "Poly (lactide-co-glycolide) particles of different physicochemical properties and their uptake by peyer's patches in mice," *Eur. J. Pharm. Biopharm.*, vol. 61, no. 1, pp. 1–13, Sep. 2005.

[119] P. Jani, G. W. Halbert, J. Langridge, and A. T. Florence, "The uptake and translocation of latex nanospheres and microspheres after oral administration to rats," *J. Pharm. Pharmacol.*, vol. 41, no. 12, pp. 809–812, Dec. 1989.

[120] P. Aggarwal, J. B. Hall, C. B. McLeland, M. A. Dobrovolskaia, and S. E. McNeil, "Nanoparticle interaction with plasma proteins as it relates to particle biodistribution, biocompatibility and therapeutic efficacy," *Adv. Drug Deliv. Rev.*, vol. 61, no. 6, pp. 428–437, Jun. 2009.

[121] M. A. Dobrovolskaia, P. Aggarwal, J. B. Hall, and S. E. McNeil, "Preclinical studies to understand nanoparticle interaction with the immune system and its potential effects on nanoparticle biodistribution," *Mol. Pharm.*, vol. 5, no. 4, pp. 487–495, Aug. 2008.

[122] A. J. Gormley and H. Ghandehari, "Evaluation of Toxicity of Nanostructures in Biological Systems," in *Nanotoxicity*, S. C. Sahu and D. A. Casciano, Eds. John Wiley & Sons, Ltd, 2009, pp. 115–159.

[123] D. E. Owens and N. A. Peppas, "Opsonization, biodistribution, and pharmacokinetics of polymeric nanoparticles," *Int. J. Pharm.*, vol. 307, no. 1, pp. 93–102, Jan. 2006.

[124] G. Sonavane, K. Tomoda, and K. Makino, "Biodistribution of colloidal gold nanoparticles after intravenous administration: effect of particle size," *Colloids Surf. B Biointerfaces*, vol. 66, no. 2, pp. 274–280, Oct. 2008.

[125] H. Carrstensen, R. H. Müller, and B. W. Müller, "Particle size, surface hydrophobicity and interaction with serum of parenteral fat emulsions and model drug carriers as parameters related to RES uptake," *Clin. Nutr. Edinb. Scotl.*, vol. 11, no. 5, pp. 289–297, Oct. 1992.

[126] R. H. Müller, K. H. Wallis, S. D. Tröster, and J. Kreuter, "In vitro characterization of poly(methyl-methaerylate) nanoparticles and correlation to their in vivo fate," *J. Controlled Release*, vol. 20, no. 3, pp. 237–246, Aug. 1992.

[127] M. E. Norman, P. Williams, and L. Illum, "Human serum albumin as a probe for surface conditioning (opsonization) of block copolymer-coated microspheres," *Biomaterials*, vol. 13, no. 12, pp. 841–849, Jan. 1992.

[128] M. Roser, D. Fischer, and T. Kissel, "Surface-modified biodegradable albumin nano- and microspheres. II: effect of surface charges on in vitro phagocytosis and biodistribution in rats," *Eur. J. Pharm. Biopharm.*, vol. 46, no. 3, pp. 255–263, Nov. 1998.

[129] Y. Qiu *et al.*, "Surface chemistry and aspect ratio mediated cellular uptake of Au nanorods," *Biomaterials*, vol. 31, no. 30, pp. 7606–7619, Oct. 2010.

[130] Q. He, Z. Zhang, F. Gao, Y. Li, and J. Shi, "In vivo biodistribution and urinary excretion of mesoporous silica nanoparticles: effects of particle size and PEGylation," *Small Weinh. Bergstr. Ger.*, vol. 7, no. 2, pp. 271–280, Jan. 2011.

[131] J. S. Souris *et al.*, "Surface Charge-Mediated Rapid Hepatobiliary Excretion of Mesoporous Silica Nanoparticles," *Biomaterials*, vol. 31, no. 21, pp. 5564–5574, Jul. 2010.

[132] A. Nel, T. Xia, L. Mädler, and N. Li, "Toxic Potential of Materials at the Nanolevel," *Science*, vol. 311, no. 5761, pp. 622–627, Feb. 2006.

[133] J. Wang, W. Sun, and S. F. Ali, "Nanoparticles: Is Neurotoxicity a Concern?," in *Nanotoxicity*, S. C. Sahu and D. A. Casciano, Eds. John Wiley & Sons, Ltd, 2009, pp. 171–182.

[134] T. R. Pisanic, S. Jin, and V. I. Shubayev, "Iron Oxide Magnetic Nanoparticle Toxicity: Incidence and Mechanisms," in *Nanotoxicity*, S. C. Sahu and D. A. Casciano, Eds. John Wiley & Sons, Ltd, 2009, pp. 397–425.

[135] J. Simak, "Nanotoxicity in Blood: Effects of Engineered Nanomaterials on Platelets," in *Nanotoxicity*, S. C. Sahu and D. A. Casciano, Eds. John Wiley & Sons, Ltd, 2009, pp. 191–225.

[136] F. Schwab, G. Zhai, M. Kern, A. Turner, J. L. Schnoor, and M. R. Wiesner, "Barriers, pathways and processes for uptake, translocation and accumulation of nanomaterials in plants--Critical review," *Nanotoxicology*, vol. 10, no. 3, pp. 257–278, 2016.

[137] J. L. Gardea-Torresdey, C. M. Rico, and J. C. White, "Trophic Transfer, Transformation, and Impact of Engineered Nanomaterials in Terrestrial Environments," *Environ. Sci. Technol.*, vol. 48, no. 5, pp. 2526–2540, Mar. 2014.

[138] S. C. C. Arruda, A. L. D. Silva, R. M. Galazzi, R. A. Azevedo, and M. A. Z. Arruda, "Nanoparticles applied to plant science: A review," *Talanta*, vol. 131, pp. 693–705, Jan. 2015.

[139] P. Miralles, T. L. Church, and A. T. Harris, "Toxicity, Uptake, and Translocation of Engineered Nanomaterials in Vascular plants," *Environ. Sci. Technol.*, vol. 46, no. 17, pp. 9224–9239, Sep. 2012.

[140] T. Xiong *et al.*, "Copper Oxide Nanoparticle Foliar Uptake, Phytotoxicity, and Consequences for Sustainable Urban Agriculture," *Environ. Sci. Technol.*, vol. 51, no. 9, pp. 5242–5251, May 2017.

[141] R. Aryal, A. Kim, B.-K. Lee, M. Kamruzzaman, and S. Beecham, "Characteristics of Atmospheric Particulate Matter and Metals in Industrial Sites in Korea," *Environ. Pollut.*, vol. 2, no. 4, p. 10, Aug. 2013.

[142] G.-C. Fang and C.-S. Huang, "Atmospheric Particulate and Metallic Elements (Zn, Ni, Cu, Cd and Pb) Size Distribution at Three Characteristic Sampling Sites," *Environ. Forensics*, vol. 12, no. 3, pp. 191–199, Sep. 2011.

[143] N. T. Hieu and B.-K. Lee, "Characteristics of particulate matter and metals in the ambient air from a residential area in the largest industrial city in Korea," *Atmospheric Res.*, vol. 98, no. 2, pp. 526–537, Nov. 2010.

[144] M. Moustafa, A. Mohamed, A.-R. Ahmed, and H. Nazmy, "Mass size distributions of elemental aerosols in industrial area," *J. Adv. Res.*, vol. 6, no. 6, pp. 827–832, Nov. 2015.

[145] E. Schreck *et al.*, "Metal and metalloid foliar uptake by various plant species exposed to atmospheric industrial fallout: Mechanisms involved for lead," *Sci. Total Environ.*, vol. 427–428, pp. 253–262, Jun. 2012.

[146] E. Schreck *et al.*, "Foliar or root exposures to smelter particles: Consequences for lead compartmentalization and speciation in plant leaves," *Sci. Total Environ.*, vol. 476–477, pp. 667–676, Apr. 2014.

[147] M. S. Al Jassir, A. Shaker, and M. A. Khaliq, "Deposition of Heavy Metals on Green Leafy Vegerables Sold on Roadsides of Riyadh City, Saudi Arabia," *Bull. Environ. Contam. Toxicol.*, vol. 75, no. 5, pp. 1020–1027, Nov. 2005.

[148] X. Hu, Y. Zhang, J. Luo, M. Xie, T. Wang, and H. Lian, "Accumulation and quantitative estimates of airborne lead for a wild plant (Aster subulatus)," *Chemosphere*, vol. 82, no. 10, pp. 1351–1357, Mar. 2011.

[149] T. Xiong, T. Leveque, M. Shahid, Y. Foucault, S. Mombo, and C. Dumat, "Lead and cadmium phytoavailability and human bioaccessibility for vegetables exposed to soil or atmospheric pollution by process ultrafine particles," *J. Environ. Qual.*, vol. 43, no. 5, pp. 1593–1600, Sep. 2014.

[150] L. C. D. Silva, M. A. Oliva, A. A. Azevedo, and J. M. D. Araújo, "Responses of restinga plant species to pollution from an iron pelletization factory," *Water. Air. Soil Pollut.*, vol. 175, no. 1–4, pp. 241–256, Aug. 2006.

[151] Y. Song, B. A. Maher, F. Li, X. Wang, X. Sun, and H. Zhang, "Particulate matter deposited on leaf of five evergreen species in Beijing, China: Source identification and size distribution," *Atmos. Environ.*, vol. 105, pp. 53–60, Mar. 2015.

[152] L. C. D. Silva, M. A. Oliva, A. A. Azevedo, and J. M. D. Araújo, "Responses of restinga plant species to pollution from an iron pelletization factory," *Water. Air. Soil Pollut.*, vol. 175, no. 1–4, pp. 241–256, Sep. 2006.

[153] V. Fernández and P. H. Brown, "From plant surface to plant metabolism: the uncertain fate of foliar-applied nutrients," *Front. Plant Sci.*, vol. 4, Jul. 2013.

[154] E. Domínguez, J. A. Heredia-Guerrero, and A. Heredia, "The biophysical design of plant cuticles: an overview," *New Phytol.*, vol. 189, no. 4, pp. 938–949, Mar. 2011.

[155] J. Burkhardt and S. Pariyar, "Particulate pollutants are capable to 'degrade' epicuticular waxes and to decrease the drought tolerance of Scots pine (Pinus sylvestris L.)," *Environ. Pollut.*, vol. 184, pp. 659–667, Jan. 2014.

[156] K. R. Stern, J. E. Bidlack, and S. H. Jansky, *Introductory Plant Biology*, Eleventh Edition. McGraw-Hill, 2008.

[157] C. Larue *et al.*, "Accumulation, translocation and impact of TiO2 nanoparticles in wheat (Triticum aestivum spp.): Influence of diameter and crystal phase," *Sci. Total Environ.*, vol. 431, pp. 197–208, Aug. 2012.

[158] D. Lin and B. Xing, "Root Uptake and Phytotoxicity of ZnO Nanoparticles," *Environ. Sci. Technol.*, vol. 42, no. 15, pp. 5580–5585, Aug. 2008.

[159] G. Zhai, K. S. Walters, D. W. Peate, P. J. J. Alvarez, and J. L. Schnoor, "Transport of Gold Nanoparticles through Plasmodesmata and Precipitation of Gold Ions in Woody Poplar," *Environ. Sci. Technol. Lett.*, vol. 1, no. 2, pp. 146–151, Feb. 2014.

[160] T. Sabo-Attwood *et al.*, "Uptake, distribution and toxicity of gold nanoparticles in tobacco (Nicotiana xanthi) seedlings," *Nanotoxicology*, vol. 6, no. 4, pp. 353–360, Jun. 2012.

[161] L. Taiz and E. Zeiger, *Plant Physiology*, Third Edition. Sunderland, MA: Sinauer Associates, Inc., 2002.

[162] Y. Feng *et al.*, "The Role of Metal Nanoparticles in Influencing Arbuscular Mycorrhizal Fungi Effects on Plant Growth," *Environ. Sci. Technol.*, vol. 47, no. 16, pp. 9496–9504, Aug. 2013.

[163] A. Manceau *et al.*, "Formation of Metallic Copper Nanoparticles at the Soil−Root Interface," *Environ. Sci. Technol.*, vol. 42, no. 5, pp. 1766–1772, Mar. 2008.

[164] C. Vannini *et al.*, "Phytotoxic and genotoxic effects of silver nanoparticles exposure on germinating wheat seedlings," *J. Plant Physiol.*, vol. 171, no. 13, pp. 1142–1148, Aug. 2014.

[165] J. Lv, S. Zhang, L. Luo, J. Zhang, K. Yang, and P. Christie, "Accumulation, speciation and uptake pathway of ZnO nanoparticles in maize," *Environ. Sci. Nano*, vol. 2, no. 1, pp. 68–77, Feb. 2015.

[166] P. Zhang *et al.*, "Comparative toxicity of nanoparticulate/bulk Yb2O3 and YbCl3 to cucumber (Cucumis sativus)," *Environ. Sci. Technol.*, vol. 46, no. 3, pp. 1834–1841, Feb. 2012.

[167] C. O. Dimkpa, D. E. Latta, J. E. McLean, D. W. Britt, M. I. Boyanov, and A. J. Anderson, "Fate of CuO and ZnO Nano- and Microparticles in the Plant Environment," *Environ. Sci. Technol.*, vol. 47, no. 9, pp. 4734–4742, May 2013.

[168] N. Al-Salim *et al.*, "Quantum dot transport in soil, plants, and insects," *Sci. Total Environ.*, vol. 409, no. 17, pp. 3237–3248, Aug. 2011.

[169] J. Geisler-Lee *et al.*, "Phytotoxicity, accumulation and transport of silver nanoparticles by Arabidopsis thaliana," *Nanotoxicology*, vol. 7, no. 3, pp. 323–337, May 2013.

[170] Z.-J. Zhu *et al.*, "Effect of Surface Charge on the Uptake and Distribution of Gold Nanoparticles in Four Plant Species," *Environ. Sci. Technol.*, vol. 46, no. 22, pp. 12391–12398, Nov. 2012.

[171] J. Wang, Y. Yang, H. Zhu, J. Braam, J. L. Schnoor, and P. J. J. Alvarez, "Uptake, translocation, and transformation of quantum dots with cationic versus anionic coatings by Populus deltoides × nigra cuttings," *Environ. Sci. Technol.*, vol. 48, no. 12, pp. 6754–6762, Jun. 2014.

[172] X. Ma, J. Geiser-Lee, Y. Deng, and A. Kolmakov, "Interactions between engineered nanoparticles (ENPs) and plants: Phytotoxicity, uptake and accumulation," *Sci. Total Environ.*, vol. 408, no. 16, pp. 3053–3061, Jul. 2010.

[173] G. Uzu, S. Sobanska, G. Sarret, M. Muñoz, and C. Dumat, "Foliar Lead Uptake by Lettuce Exposed to Atmospheric Fallouts," *Environ. Sci. Technol.*, vol. 44, no. 3, pp. 1036–1042, Feb. 2010.

[174] C. M. Rico, S. Majumdar, M. Duarte-Gardea, J. R. Peralta-Videa, and J. L. Gardea-Torresdey, "Interaction of Nanoparticles with Edible Plants and Their Possible Implications in the Food Chain," *J. Agric. Food Chem.*, vol. 59, no. 8, pp. 3485–3498, Apr. 2011.

[175] W.-N. Wang, J. C. Tarafdar, and P. Biswas, "Nanoparticle synthesis and delivery by an aerosol route for watermelon plant foliar uptake," *J. Nanoparticle Res.*, vol. 15, no. 1, Jan. 2013.

[176] T. Eichert, A. Kurtz, U. Steiner, and H. E. Goldbach, "Size exclusion limits and lateral heterogeneity of the stomatal foliar uptake pathway for aqueous solutes and water-suspended nanoparticles," *Physiol. Plant.*, vol. 134, no. 1, pp. 151–160, Sep. 2008.

[177] J. Burkhardt and M. Hunsche, "'Breath figures' on leaf surfaces—formation and effects of microscopic leaf wetness," *Front. Plant Sci.*, vol. 4, 2013.

[178] C. Larue *et al.*, "Fate of pristine TiO2 nanoparticles and aged paint-containing TiO2 nanoparticles in lettuce crop after foliar exposure," *J. Hazard. Mater.*, vol. 273, pp. 17–26, May 2014.

[179] K. Birbaum *et al.*, "No Evidence for Cerium Dioxide Nanoparticle Translocation in Maize Plants," *Environ. Sci. Technol.*, vol. 44, no. 22, pp. 8718–8723, Nov. 2010.

[180] C. Larue *et al.*, "Foliar exposure of the crop Lactuca sativa to silver nanoparticles: Evidence for internalization and changes in Ag speciation," *J. Hazard. Mater.*, vol. 264, pp. 98–106, Jan. 2014.

[181] J. Hong *et al.*, "Evidence of Translocation and Physiological Impacts of Foliar Applied CeO2 Nanoparticles on Cucumber (Cucumis sativus) Plants," *Environ. Sci. Technol.*, vol. 48, no. 8, pp. 4376–4385, Apr. 2014.

[182] K.-J. Dietz and S. Herth, "Plant nanotoxicology," *Trends Plant Sci.*, vol. 16, no. 11, pp. 582–589, Nov. 2011.

[183] P. Lü *et al.*, "Nano-silver pulse treatments improve water relations of cut rose cv. Movie Star flowers," *Postharvest Biol. Technol.*, vol. 57, no. 3, pp. 196–202, Sep. 2010.

[184] J.-Y. Lee and H. Lu, "Plasmodesmata: the battleground against intruders," *Trends Plant Sci.*, vol. 16, no. 4, pp. 201–210, Apr. 2011.

[185] J. Kurepa *et al.*, "Uptake and Distribution of Ultrasmall Anatase TiO $_2$ Alizarin Red S Nanoconjugates in *Arabidopsis thaliana*," *Nano Lett.*, vol. 10, no. 7, pp. 2296–2302, Jul. 2010.

[186] M. N. Moore, "Do nanoparticles present ecotoxicological risks for the health of the aquatic environment?," *Environ. Int.*, vol. 32, no. 8, pp. 967–976, Dec. 2006.

[187] M. Remškar, G. Tavčar, and S. D. Škapin, "Sparklers as a nanohazard: size distribution measurements of the nanoparticles released from sparklers," *Air Qual. Atmosphere Health*, vol. 8, no. 2, pp. 205–211, Apr. 2015.

[188] S. Terashima, N. Mita, S. Nakao, and S. Ishihara, "Platinum and Palladium Abundances in Marine Sediments and Their Geochemical Behavior in Marine Environments.," *Bull. Geol. Surv. Jpn.*, vol. 53, no. 11–12, pp. 725–247, 2002.

[189] K. H. Ek, G. M. Morrison, and S. Rauch, "Environmental routes for platinum group elements to biological materials--a review," *Sci. Total Environ.*, vol. 334–335, pp. 21–38, Dec. 2004.

[190] J. S. Taurozzi, V. A. Hackley, and M. R. Wiesner, "Ultrasonic dispersion of nanoparticles for environmental, health and safety assessment – issues and recommendations," *Nanotoxicology*, vol. 5, no. 4, pp. 711–729, Dec. 2011.

[191] K. A. Khalik, "Morphological studies on trichomes of Brassicaceae in Egypt and taxonomic significance," *Acta Bot. Croat.*, vol. 64, no. 1, pp. 57–73, May 2005.

[192] V. Fernández and M. Khayet, "Evaluation of the surface free energy of plant surfaces: toward standardizing the procedure," *Front. Plant Sci.*, vol. 6, Jul. 2015.

[193] K. Koch, B. Bhushan, and W. Barthlott, "Multifunctional surface structures of plants: An inspiration for biomimetics," *Prog. Mater. Sci.*, vol. 54, no. 2, pp. 137–178, Feb. 2009.

[194] J. K. Spelt, D. Li, and A. W. Neumann, "The Equation of State Approach to Interfacial Tensions," in *Modern Approaches to Wettability*, Springer, Boston, MA, 1992, pp. 101–142.

[195] Y. Yuan and T. R. Lee, "Contact Angle and Wetting Properties," in *Surface Science Techniques*, Springer, Berlin, Heidelberg, 2013, pp. 3–34.

[196] F. Hejda, P. Solar, and J. Kousal, "Surface Free Energy Determination by Contact Angle Measurements - A Comparison of Various Approaches," in *WDS'10 Proceedings of Contributed Papers, Part III*, 2010, pp. 25–30.

[197] D. K. Owens and R. C. Wendt, "Estimation of the surface free energy of polymers," *J. Appl. Polym. Sci.*, vol. 13, no. 8, pp. 1741–1747, Aug. 1969.

[198] S. Wu, "Calculation of interfacial tension in polymer systems," *J. Polym. Sci. Part C Polym. Symp.*, vol. 34, no. 1, pp. 19–30, Jan. 1971.

[199] C. J. Van Oss, M. K. Chaudhury, and R. J. Good, "Interfacial Lifshitz-van der Waals and polar interactions in macroscopic systems," *Chem. Rev.*, vol. 88, no. 6, pp. 927–941, Sep. 1988.

[200] A. Kroflič, M. Germ, Š. Mechora, and V. Stibilj, "Selenium and its compounds in aquatic plant Veronica anagallis-aquatica," *Chemosphere*, vol. 151, pp. 296–302, May 2016.

[201] Food and Drug Administration: Center for Food Safety and Applied Nutrition, "Produce: Selecting and Serving it Safely."

[202] European Food Safety Authority, "EFSA Updates Consumer Advice on Sprout Consumption Following the 2011 E. coli Outbreak in Germany & France."

[203] T. Eftimov, P. Korošec, and B. Koroušić Seljak, "A Novel Approach to statistical comparison of meta-heuristic stochastic optimization algorithms using deep statistics," *Inf. Sci.*, vol. 417, no. Supplement C, pp. 186–215, Nov. 2017.

[204] C.-R. Yang, T.-C. Lin, and F.-H. Chang, "Correlation between calcium carbonate content and emission characteristics of incense," *J. Air Waste Manag. Assoc. 1995*, vol. 56, no. 12, pp. 1726–1732, Dec. 2006.

[205] G.-C. Fang *et al.*, "Fine (PM2.5), coarse (PM2.5-10), and metallic elements of suspended particulates for incense burning at Tzu Yun Yen temple in central Taiwan," *Chemosphere*, vol. 51, no. 9, pp. 983–991, Jun. 2003.

[206] R. Zhou, Q. An, X. W. Pan, B. Yang, J. Hu, and Y. H. Wang, "Higher cytotoxicity and genotoxicity of burning incense than cigarette," *Environ. Chem. Lett.*, vol. 13, no. 4, pp. 465–471, Dec. 2015.

[207] I. Lagzi, R. Mészáros, G. Gelybó, and Á. Leelőssy, *Atmospheric Chemistry*. Eötvös Loránd University, 2013.

[208] W. W. Nazaroff, "Indoor particle dynamics," *Indoor Air*, vol. 14 Suppl 7, pp. 175–183, 2004.

[209] C.-R. Yang, T.-C. Lin, and F.-H. Chang, "Particle size distribution and PAH concentrations of incense smoke in a combustion chamber," *Environ. Pollut. Barking Essex 1987*, vol. 145, no. 2, pp. 606–615, Jan. 2007.

[210] B. Višić *et al.*, "Incense powder and particle emission characteristics during and after burning incense in an unventilated room setting," *Air Qual. Atmosphere Health*, vol. 11, no. 6, pp. 649–663, Jul. 2018.

[211] Z. Zhang and Q. Chen, "Experimental measurements and numerical simulations of particle transport and distribution in ventilated rooms," *Atmos. Environ.*, vol. 40, no. 18, pp. 3396–3408, Jun. 2006.

[212] Y. Zhou, Y. Deng, P. Wu, and S.-J. Cao, "The effects of ventilation and floor heating systems on the dispersion and deposition of fine particles in an enclosed environment," *Build. Environ.*, vol. 125, pp. 192–205, Nov. 2017.

[213] C. Zhuang, G. Yang, T. Long, and D. Hu, "Numerical comparison of removal and deposition for fully-distributed particles in central- and split-type air-conditioning rooms," *Build. Environ.*, vol. 112, pp. 17–28, Feb. 2017.

[214] M. E. Vance and L. C. Marr, "Exposure to airborne engineered nanoparticles in the indoor environment," *Atmos. Environ.*, vol. 106, pp. 503–509, Apr. 2015.

[215] S. Lustig, S. Zang, W. Beck, and P. Schramel, "Dissolution of metallic platinum as water soluble species by naturally occurring complexing agents," *Microchim. Acta*, vol. 129, no. 3–4, pp. 189–194, Sep. 1998.

[216] N. Odzak, D. Kistler, R. Behra, and L. Sigg, "Dissolution of metal and metal oxide nanoparticles in aqueous media," *Environ. Pollut.*, vol. 191, pp. 132–138, Aug. 2014.

[217] M. S. Silberberg and P. G. Amateis, "Kinetics: Rates and Mechanisms of Chemical Reactions," in *Chemistry: The Molecular Nature of Matter and Change*, 7th Ed., New York, NY: McGraw-Hill Education, 2015, pp. 674–729.

[218] E. Kranjc, D. Mazej, M. Regvar, D. Drobne, and M. Remškar, "Foliar surface free energy affects platinum nanoparticle adhesion, uptake, and translocation from leaves to roots in arugula and escarole," *Environ. Sci. Nano*, Dec. 2017.

[219] T. Hirano, M. Kiyota, and I. Aiga, "Physical effects of dust on leaf physiology of cucumber and kidney bean plants," *Environ. Pollut.*, vol. 89, no. 3, pp. 255–261, Jan. 1995.

[220] S. L. Honour, J. N. B. Bell, T. W. Ashenden, J. N. Cape, and S. A. Power, "Responses of herbaceous plants to urban air pollution: effects on growth, phenology and leaf surface characteristics," *Environ. Pollut. Barking Essex 1987*, vol. 157, no. 4, pp. 1279–1286, Apr. 2009.

[221] F. Kardel, K. Wuyts, M. Babanezhad, T. Wuytack, S. Adriaenssens, and R. Samson, "Tree leaf wettability as passive bio-indicator of urban habitat quality," *Environ. Exp. Bot.*, 2012.

[222] J. Hong *et al.*, "Toxic effects of copper-based nanoparticles or compounds to lettuce (Lactuca sativa) and alfalfa (Medicago sativa)," *Environ. Sci. Process. Impacts*, vol. 17, no. 1, pp. 177–185, Jan. 2015.

[223] W.-N. Wang, J. C. Tarafdar, and P. Biswas, "Nanoparticle synthesis and delivery by an aerosol route for watermelon plant foliar uptake," *J. Nanoparticle Res.*, vol. 15, no. 1, p. 1417, Jan. 2013.

[224] D. Lin and B. Xing, "Root Uptake and Phytotoxicity of ZnO Nanoparticles," *Environ. Sci. Technol.*, vol. 42, no. 15, pp. 5580–5585, Aug. 2008.

[225] K. Birbaum *et al.*, "No Evidence for Cerium Dioxide Nanoparticle Translocation in Maize Plants," *Environ. Sci. Technol.*, vol. 44, no. 22, pp. 8718–8723, Nov. 2010.

[226] A. Valletta, L. Chronopoulou, C. Palocci, B. Baldan, L. Donati, and G. Pasqua, "Poly(lactic-<Emphasis Type="Italic">co</Emphasis>-glycolic) acid

nanoparticles uptake by <Emphasis Type="Italic">Vitis vinifera</Emphasis> and grapevine-pathogenic fungi," *J. Nanoparticle Res.*, vol. 16, no. 12, p. 2744, Dec. 2014.

[227] M. Uyttendaele, L. Jacxsens, and S. Van Boxstael, "4 - Issues surrounding the European fresh produce trade: a global perspective," in *Global Safety of Fresh Produce*, J. Hoorfar, Ed. Woodhead Publishing, 2014, pp. 33–51.

Bibliography

Publications Related to the Thesis

Journal Articles

B. Višić, E. Kranjc, L. Pirker, U. Bačnik, G. Tavčar, S.D. Škapin, and M. Remškar, "Incense powder and particle emission characteristics during and after burning incense in an unventilated room setting," *Air quality, Atmosphere & Health,* vol. 11, issue 6, pp. 649-663, 2018.

E. Kranjc, D. Mazej, M. Regvar, D. Drobne, and M. Remškar, "Foliar surface free energy affects platinum nanoparticle adhesion, uptake, and translocation from leaves to roots in arugula and escarole," *Environmental Science: Nano,* vol. 5, no. 2, pp. 520-532, 2018.

Conference Abstracts

E. Kranjc, D. Mazej, M. Regvar, D. Drobne, and M. Remškar, "Comparison of arugula (Eruca sativa Mill.) and escarole (Cichorium endivia L.) interactions with foliar- and root-applied platinum nanoparticles," in *NANOAPP 2017, Nanomaterials & Application*, Bled, Slovenia 2017.

E. Kranjc, D. Mazej, M. Regvar, R. Milačič, M. Horvat, D. Drobne, and M. Remškar, "Comparison of arugula (Eruca sativa Mill.) and escarole (Cichorium endivia L.) interactions with foliar- and root-applied platinum nanoparticles," in *9th Jožef Stefan International Postgraduate School Students' Conference and 11th Young Researchers' Day*, Ljubljana, Slovenia: Jožef Stefan International Postgraduate School: Jožef Stefan Institute, 2017.

E. Kranjc, M. Remškar, D. Drobne, and S. Novak, "Pogledi na nanovarnost na primeru nanosa nanodelcev platine na solati (rukola in endivija)," in *Nanovarnost – ali smo dovolj previdni z nano?: zbornik povzetkov*, Izola, Slovenia: Nacionalni inštitut za javno zdravje, 2016.

E. Kranjc, M. Remškar, D. Drobne, and S. Novak, "Comparison of internalization and translocation of platinum nanoparticles in arugula (Eruca sativa Mill.) and escarole (Cichorium endivia L.) salad greens," in *4th International ISEKI_Food Conference*, Vienna, Austria: ISEKI-Food Association, 2016.

Other Publications (optional)

Work Reports

E. Kranjc, M. Remškar, "Measurements of nanoparticles in air in the laboratory of SavaTech d.o.o.," IJS working report 11777, 2014.

E. Kranjc, M. Koblar, M. Remškar, "Meritve nanodelcev v zraku," IJS working report 11738, 2014.

Invited Conference Lectures

E. Kranjc, "Nanoparticles and food (safety): the adhesion, uptake, and translocation of Pt nanoparticles by arugula and escarole plants," in *ISO-FOOD Spring School * Workshop on Nanoparticles and Food*, Ljubljana, Slovenia: Jožef Stefan Institute 2018.

. . .